Atom Interferometry in ^{85}Rb

Department of Physics

University of Liverpool

Thesis submitted in accordance with the requirements of the University of Liverpool for the degree of Doctor in Philosophy by Andrew Edward Carroll

March 2019

Acknowledgements

I would like to thank my supervisor, Jonathon Coleman, for his wisdom and words of encouragement during difficult times. I would also like to thank Carl Metelko, who was always around to offer solutions to various perplexing issues. During my time in the laboratory, I worked with David Morris, Jonathan Tinsley, Gedminas Elertas and Alex Webber-Date, each of whom was an unalloyed pleasure to spend time with. I would like to thank the Liverpool Particle Physics Group for being the most welcoming and supportive group I could possibly have hoped for. I would also like to thank the workshop for their expertise and cheerful advice, even under difficult circumstances. This work simply could not have been accomplished without them. Finally, I would like to thank my family, for their unwavering support throughout.

Abstract

Atom interferometry is a rapidly progressing field of contemporary research, offering unprecedented measurement sensitivity to space-time and its distortion. This sensitivity increase is promising both for probing fundamental physics, such as the dark-sector and gravitational waves, and for technological applications such as gyroscopes and gravity gradiometers. Current evidence for dark matter and dark energy is solely based on astronomical observations. This thesis is therefore motivated by the eventual aim to apply this new sensitivity to the measurement of a dark-sector field on the laboratory scale.

The drop-topology atom interferometer at the University of Liverpool is based on a two-laser system to create all of the required interferometry frequencies. This system confines rubidium-85 atoms in a magneto-optical trap before sub-Doppler cooling mechanisms reduce the atoms to μK temperatures. The states of these atoms are then manipulated via Raman transitions. As part of this thesis, the state detection system was upgraded and sources of decoherence removed, resulting in the observation of coherent manipulation of atomic states via Rabi oscillations and the calibration of beam-splitter and mirror pulses. A clock sequence was then realised, demonstrating interference via Ramsey fringes with a coherence time of around a millisecond.

Author's Contribution

When I came into the laboratory, a magneto-optical trap had been developed and some hints of the Raman system affecting the atoms had been found. I helped upgrade the MOT, converting it to a fibre-launch setup which increased the beam size from 3.4 mm to 12.0 mm. I improved the state detection system to make it more accurate and stable over time. I suspected the presence of contaminant light in the chamber was causing destruction of reliable state manipulation, as evidenced by the consistently large excited population independent of the Raman beam interaction. A microwave horn was profiled and installed to act as an independent check on the Raman system. I then took several actions to reduce the presence of this contaminant light and observed reliable state manipulations with the microwave horn, culminating in heavily damped single-photon Rabi oscillations being observed. These resonances were then used to measure and minimise the magnetic field in the chamber.

After the decoherence effects from the MOT beams were reduced, the system was switched back to Raman transitions. I improved and upgraded the Raman system, as well as detecting and eliminating a source of contaminant light specific to this system. This led to two-photon Raman transitions being observed, followed by Rabi oscillations. These oscillations allowed the calibration of $\pi/2$ pulses which then resulted in interference fringes being observed via a Ramsey sequence.

Table of contents

List of figures **xiii**

1 Introduction **1**

1.1 Overview of Atom Interferometry 1

1.1.1 Applications and Fundamental Physics 1

1.1.2 Principles of Atom Interferometry 3

1.2 Discussion of Experiment 3

1.3 Dark Energy Searches 5

2 Atom Interferometry Theory **9**

2.1 Laser Cooling and Atom Trapping 9

2.1.1 Doppler cooling and the Doppler Limit 9

2.1.2 Magneto-Optical Trapping 11

2.1.3 Sub-Doppler Cooling 15

2.2 Atomic Interaction with Radiation 17

2.2.1 Two-Level Systems 17

2.2.2 Interaction Hamiltonian 19

2.3 Raman Transitions 25

2.4 Atomic Structure and Selection Rules 31

2.5 Interference 33

2.5.1 Ramsey Fringes 33

2.5.2 Atom Interferometry Sequence 36

2.5.3 Gravimetry 40

3 Experimental Overview **43**

3.1 Vacuum Chamber 43

3.2 Laser Control 45

3.2.1 Frequency Locking 45

3.2.2 Power Amplification 51

3.3 Sequence Timing 53

3.3.1 Cooling Laser Control 53

3.3.2 Repumper Laser Control 55

3.3.3 Shutters 55

3.4 Magnetic Coils 57

3.4.1 Bias Magnetic Coils 57

3.4.2 MOT Coils 57

3.5 FPGA Control 57

3.6 MOT Beam Delivery 58

3.6.1 MOT Beams 58

3.6.2 Power Balancing 60

3.7 MOT and Molasses Diagnostics 62

3.7.1 Cameras 63

3.7.2 Beam Alignment Procedure 63

3.7.3 Atom Number Measurement 65

3.7.4 Temperature Measurement 65

3.8 Microwave Horn 68

3.9 Raman System 71

3.9.1 Raman Power Upgrade 75

3.9.2 Raman Beam Alignment 76

3.9.3 Raman Beam Coherence 76

3.10 State Detection 77

3.10.1 Fluorescence Measurement Apparatus 77

3.11 Interferometry Sequence 79

4 Search for Coherent State Manipulation 83

4.1 First Observation of Raman Resonance 83

4.2 Signal to Noise Improvement 85

4.3 Reduction of Contaminant Light 87

4.3.1 AOM0 88

4.3.2 AOM1 89

4.3.3 AOM2 90

4.3.4 Raman System 91

4.3.5 Shutters 92

4.3.6 Summary 92

4.4 Microwave Horn Scans 92

4.4.1 Frequency Scans 93

4.4.2 Data Readout and Errors 94

4.4.3 Rabi Oscillation Scan 96

4.5 Magnetic Spectroscopy 96

4.6 Summary 100

5 State Manipulation: Raman Beams 103

5.1 Raman System Upgrade 103

5.1.1 Circular Polariser 103

5.2 Raman Resonances 104

5.3 Rabi Oscillations 107

5.4 Ramsey Fringes 109

5.5 Loss of Coherence 112

5.6 Sources of Decoherence 113

5.6.1 Atomic Collisions 114

5.6.2 On-Resonant Light 115

6 Summary **117**

Appendix A Rubidium 85 D2 Transition Data [51] **119**

References **121**

List of figures

1.1 Schematic representation of the interferometry sequence [35]. The atoms are cooled and state selected at stage (a), then released to fall down the interferometry pipe at (b). Raman beams put the atoms into a superposition of states at (c), represented by red and blue circles. (d) is a propagation time T, after which a second pulse reverses the states of the wavepackets (e). (f) is another propagation time T. At (g), the two wavepackets now overlap again, and a final Raman pulse is applied. Finally, the state detection pulses are applied at (h), measuring the population discrepancy from the original population in (b). 6

1.2 Two interferometers are positioned in the same noise envelope and using the same lasers, but separated by some baseline distance. The difference in phase between the interferometers, $\Delta(\Delta\phi) \equiv \Delta\Phi$, is expected to be zero, with all sources of phase noise common to both interferometers. Any deviation from $\Delta(\Delta\phi) = 0$ could be evidence of a dark energy field gradient between the two arms. 8

2.1 Plot of the scattering rate as a function of optical frequency. The dashed lines show how atoms with equal but opposite Doppler shifts relative to the beam experience a drastic change in scattering rate [48]. 11

2.2 Quiver plot representation of a two-dimensional slice of equation 2.6. This plot shows that the magnetic field grows twice as quickly along the z-axis as along the x-axis, with an associated sign change between axes. This sign change must be accounted for by beam polarisation for an atom trapping effect to be created. 12

2.3 Diagram showing the Zeeman splitting of a simple, two state system with an l = 0 ground state and an l = 1 excited state. The Zeeman shift causes the red-detuned laser to be pushed towards resonance with the m = 1 substate [49]. 13

2.4 Energy level diagram for rubidium-85. The hyperfine ground and excited states have total angular momentum values F = 2 and F = 3 respectively [50][51]. 14

2.5 The superposition of $\sigma^+ - \sigma^-$ beams creates a linearly polarised field which rotates around the z-axis. [52]. 15

2.6 Magnetic substates for a J = 1 ground state. The filled circles represent the steady state populations of each state when the atom is stationary. The AC Stark effect causes the energy level difference shown between g_0 and $g_{\pm 1}$ [52]. 16

2.7 Frequency scan over resonance displays a sinc-squared function profile. The pulse time t in equation 2.26 is kept constant and is selected so that the amplitude is equal to unity when $\omega - \omega_0$ is zero, in other words it has the duration of a π pulse. 23

2.8 Rabi oscillations for various detunings from resonance. By increasing detuning, more Rabi cycles are observable before any decoherence effects cause critical damping of the oscillations. 24

2.9 The coupling of two states via a higher, intermediate state is called a lambda system. Increasing Δ while simultaneously satisfying the resonance condition makes transition to the excited state $|i\rangle$, and therefore single-photon decoherence, less likely. 26

2.10 a) Co-propagating, velocity-insensitive Raman beam configuration. b) Counter-propagating, velocity-sensitive Raman beams, with linear, orthogonal polarisation. 33
2.11 Ramsey fringes calculation plot using equation 2.65, showing the superposition of fringes over the ordinary resonance function. The $\pi/2$ pulse duration is taken to be around 0.2 s. The state population maximum is scaled to unity. 37
2.12 Diagram of the Mach-Zehnder type interferometry sequence with pulse interval T, showing the trajectories of the two paths. The sensitivity of the measurement is proportional to the integrated spacetime area between the paths [66]. 38

3.1 Diagram of the current atom interferometry vacuum chamber, showing both the upper chamber for magneto-optical trapping and state preparation and the lower chamber for state detection. 44
3.2 Overview of both independent optical circuit system, the locking circuits and magneto-optical trapping and Raman circuits. This separation is required so that work can be performed on the second optical table without causing the lasers to become unlocked due to vibrations. Optical schematics throughout created via [70]. 46
3.3 ECDL Littrow configuration: By alignment of diffraction grating, an external cavity can be created and the lasing frequency controlled. 47
3.4 ECDL lasing plot. The ECDL was aligned to be retro-reflective and the output power measured. At the lasing current, the back-reflected light begins to seed the internal laser cavity, causing the 'hockey stick' shape and the drastic increase in power, here at around 25 mA. This effect is useful diagnostically to check external cavity alignment. 48
3.5 Simple absorption spectroscopy plot for both species of rubidium, as the laser frequency is swept across the resonances. Each of the peaks is Doppler broadened, resulting in a width of the order GHz. 49

3.6 All frequency generation is done via the repumper and cooling ECDLs shown above. The repumper light is coupled to the main table via an optical fibre, with an efficiency of around 50 %. The cooling light is used as seed light for a tapered amplifier. Only around 20 mW is required for this, so the rest of the light is used as spare light for other experiments. 50

3.7 Saturated spectroscopy signal for laser locking. The narrow spikes are the 'Lamb dips' caused by saturation spectroscopy. The green line shows the error signal which is generated from the photodiode signal and is used to provide a locking slope at the peak positions. The cooling laser is locked to one of the F = 3 transitions, the repumper to one of the F = 2 transitions. . 51

3.8 Around 10 mW of locked light from the cooling laser is used to seed the tapered amplifier. The output light is then beam shaped via a concave mirror and a 1D beam expander to correct for ellipticity, followed by a 2D beam expander for collimation and coupling efficiency. Both a half waveplate and a quarter waveplate are used to create linearly polarised light which is aligned to the fast axis of the fibre. 52

3.9 As (a) shows, the output of the tapered amplifier is highly elliptical with several different modes, causing a critical reduction in fibre coupling. (b) was taken after various beam shaping measures were implemented, creating a much more Gaussian beam with a single mode. This allowed a coupling efficiency of around 40%. 53

3.10 Around 300 mW of cooling light is transported to the main table via fibre. The cooling laser is then double-passed through two AOMs to control both intensity and frequency. 54

3.11 The repumper laser is controlled via AOM2. The above design is chosen to keep the repumper on resonance, acting only as an intensity switch. 56

3.12 The field lines created by anti-Helmholtz MOT coils are shown on the left, creating an in-going magnetic field along the axial direction between the coils and an out-going field in the plane orthogonal to the axial direction. The plot on the right shows that magnetic field was measured to be linear when moving along the axial direction, with deviations from linearity at distances of around 25 mm from the centre. The red and blue lines indicate measurements for equal but opposite coil currents [75]. 58
3.13 Photographs of atom cloud and MOT beam fluorescence. Filling the upper chamber with rubidium vapour allows the beams to be observed and is useful for beam alignment. 59
3.14 Photograph a) shows the beams and atom cloud before the fibre launch upgrade and b) after the upgrade. The beams are clearly larger and a bigger atom cloud is now visible, especially relative to the larger and therefore more dispersed MOT beams. 60
3.15 Upgraded MOT beam delivery design. Translation stages to move the beams with respect to the chamber windows are not shown. 61
3.16 The cooling and repumper beams are overlapped and the half waveplates adjusted to balance the cooling powers. The cooling light is required to travel a long way ($\sim$ 6 m) before entering the final fibre collimator, so is recollimated after it passes through AOM1. 62
3.17 Example photograph a) and Gaussian fit b) to determine the beam alignment. 63
3.18 The three lines show how the beam alignment procedure outlined matches with a photograph of the MOT beams. The beam parameters are then adjusted to ensure a common crossing point for all six beams. 64
3.19 Camera image of an atom cloud. The widths of the Gaussian atom distributions are found by summing over the pixel counts in each row/column and fitting the resultant histogram. From this fit, information about size as a function of time can be inferred. 66

3.20 Example of a temperature measurement, with the red and blue lines fitting the x- and y- atom cloud positions respectively. 67
3.21 Data showing the reduction of cloud temperature as the molasses duration is increased, where molasses duration here refers to the duration of the PGC cooling effect, where the anti-Helmholtz coils are switched off and the cooling beams are highly detuned. 68
3.22 Calibration plot for the microwave horn. The frequency doubler has a cut-off input power of around 10 dBm, below which the power into the amplifier is lower than expected, exhibiting non-linear behaviour. These measurements include a loss contribution from a 5 dB attenuator. 70
3.23 The power going into the microwave horn increases linearly with the power into the amplifier, with an offset of around 7 dBm from what is expected. . 70
3.24 Position of the microwave horn, situated beneath one of the horizontal MOT beams. 71
3.25 Energy level diagram for rubidium-85. The cooling and repumper frequencies are shown, as well as the on-resonance detection beams, the further detuned molasses frequency and the two Raman frequencies detuned by $\approx$ 1.5 GHz. 72
3.26 Calibration of the cooling laser beam waist as it passes through the Brimrose. A camera was placed on a translation stage to take photos of the beam waist as it is moved along the direction of propagation. Doing this ensured that the beam waist is less than the active area of the AOM crystal. 73
3.27 Schematic of the cooling laser being split into the two Raman beam components (R1 and R2). The beams are overlapped via a beam splitter and coupled into a 10 m fibre. To match the Raman polarisations to the key of the fibre, the overlapping beam splitter is necessarily non-polarising. The PBS acts as a polarisation purifying element. The four composite lens elements are labelled from L1 to L4 moving downstream along the beam path. 74

3.28 Profiles of Raman beams R1 (left) and R2 (right) entering the Raman fibre collimation package. Profile was measured via the Thorlabs BP208-IR/M scanning slit optical beam profiler. 76
3.29 The sinusoidal fit shows how the photodiode signal varies with time as the two Raman beams exhibit a 'beat note' effect. This behaviour is only possible if the two beams have a constant phase difference, showing that they are in phase with one another. The absolute vertical offset is a function of the difference in powers between R1 and R2. 78
3.30 State detection setup. The photodiode and filter act to stop unwanted light reaching the photodiode and causing an offset on the signal. The lens positions were then calibrated to image the atom cloud onto the photodiode. The distance between the photodiode and the atom cloud is $\approx$ 10 cm. 79
3.31 Photograph a) shows the atom cloud before the state detection system was updated, showing evidence of glare and also a blurry image of the cloud. The iris and filter were uses to remove the glare and the imaging was improved by changing the lens setup, as demonstrated in b). 80
3.32 Schematic of interferometry sequence, with the interferometry sequence timing on the x-axis. The photodiode signal shows the exponential decay of the F = 3 state during the cooling pulses. 81
3.33 Example of photodiode signal, showing the cooling pulse fluorescences. The ratio of the signal amplitudes is used to infer the excited hyperfine state population after the state manipulation stage. 81

4.1 First evidence of state manipulation via Raman beams. This data was taken with a 5 ms Raman pulse. 84
4.2 Attempted Rabi oscillation scan shows the behaviour expected of critically damped oscillations. 84
4.3 The peak contrast measured after the beam delivery system was upgraded. With reference to figure 4.1, the contrast has reduced from around 0.15 to 0.06. 85
4.4 Example state population measurement with the Raman beam path blocked. 86

4.5 Example of state preparation stage calibration, showing the F = 2 state becoming fully depopulated after 1.2 ms. 87
4.6 Figure a) shows the previous PBS configuration, and figure b) the improved configuration. An extra PBS, labelled PBS3, is inserted to reduce the contaminant light. 156 mW of power is observed at the power meter when AOM0 is on. 88
4.7 Variation of waveplate angle shows that contaminant light passing through AOM0 could not be reduced below 92 μW. 89
4.8 Photodiode signal example plot. The shutter gap which was eventually inserted between the first cooling pulse and the repumper pulse has been removed for easy comparison with figure 4.4. 93
4.9 Frequency scan with microwave horn showing central peak and broadened, magnetically sensitive side resonances. 94
4.10 Frequency scan of the horn central peak, with a microwave pulse time of 5 ms. 95
4.11 Rabi oscillation with microwave horn. Coherent oscillations are clear if heavily damped. 97
4.12 Wide frequency scan showing several resonance peaks, the separation of which gives an indication of the magnetic field strength. 98
4.13 Diagram showing the single-photon transitions between the hyperfine ground state of rubidium-85 which are permitted by the selection rules. The distance between the levels is indicative of the hyperfine energy splitting. The arrows shown are the 11 non-degenerate single-photon transitions. 99
4.14 Position of resonance peaks as the magnetic coil current is linearly varied. The $m_F = 0 \rightarrow m_F = 0$ transition (orange data points) is fit with a line which is constrained to be vertical. 101

5.1 Schematic of circular polariser. The Raman system delivers linearly polarised light to this optical element, ensuring the polarisation is correct to drive velocity insensitive transitions [96]. 104

5.2 Scan of the frequency difference between the Raman beams, offset from the empirical transition (see appendix A). This data was taken with a pulse duration of around 5 ms. 105
5.3 Raman resonances fit with Lorentzian functions, for different bias field configurations. The above plots show that the amplitude with the z-coils on is larger, providing a larger signal-to-noise ratio, demonstrated by the data more closely resembling a Lorentzian distribution. 106
5.4 Initial Rabi oscillation data after removal of contaminant effects and Raman system upgrade. 107
5.5 Rabi oscillations for various detunings from resonance. The plots on the left show the linear increase in F = 3 populating mentioned earlier, due to these scans being taken without heated cells. The plots on the right have had this linear background subtracted. 108
5.6 Excited hyperfine state population as the R2 beam pulse length is increased. Both data sets are fit with linear functions. 109
5.7 Ramsey fringes with an interval length of $T = 0.8$ ms. A slight offset from the theoretical central frequency is clear, caused by the AC Stark shift. . . . 110
5.8 Ramsey fringes as a function of interval length. For $T = 0.8$ ms, the central frequency offset was found to be 0.19 ± 0.01 kHz. 111
5.9 Consistency check between the fitting parameters and the Ramsey sequence pulse settings. The proximity to the red line shows how close the expected and measured pulse intervals are, for some given offset c. By fitting with a straight line with a gradient equal to unity, this offset was found to be 0.107 $\pm$ 0.008 ms. This discrepancy may be caused by assumptions involved in deriving the Ramsey fringe equation, the pulses not being perfectly square etc. 112
5.10 Decrease in the fitted central fringe amplitude as the pulse interval time is increased. 113

5.11 Decrease of the Ramsey fringe contrast as the time between Ramsey pulses is increased. The Raman beam detuning is set to be 3 kHz away from resonance. Data was fit with a decaying sine curve. 114

Chapter 1

Introduction

1.1 Overview of Atom Interferometry

1.1.1 Applications and Fundamental Physics

Atom interferometry is one of the most promising fields in physics, combining both insights into fundamental physics in the precision measurement domain with a panoply of real-world applications [1]. Six Nobel prizes have been awarded for contributions to atomic, molecular and optical (AMO) physics, including the discovery of laser cooling techniques and the creation of a Bose-Einstein condensate [2][3]. Atom interferometers, taking advantage of these advances, may be used to test many aspects of fundamental physics, including the phase-shift caused by tidal forces on an extended wavefunction [4], setting limits on the weak equivalence principle [5][6], measurement of the fine-structure constant [7][8] and potential measurement of the gravitational Aharonov-Bohm effect [9]. These measurements and many others are exciting because they probe the experimental overlap between quantum mechanics and general relativity, offering the possibility of gaining new information about the interaction of matter and gravity. Additionally, atom interferometers are also being proposed

to measure the laboratory-scale structure of the 'dark universe' [10][11][12][13][14], with dark energy searches discussed further in section 1.3.

Atom interferometers also offer more practical uses, such as absolute gravimetry [15][16][17], gravity gradiometry [18][4], and inertial sensing [19][17]. Atom interferometers are also currently being proposed to measure gravitational waves, acting in a complementary way with existing, light-based gravitational wave sensors [20][21].

In addition to the above applications, many of the techniques used in atom interferometry have also been used to revolutionise the field of time keeping. In 1949, N. F. Ramsey developed the 'separated oscillating fields' technique, producing interference between internal states in a strongly analogous way to the classic two-slit experiments of quantum mechanics, allowing the precision frequency measurement of an on-resonant electromagnetic field [22]. This eventually resulted in the atomic time standard surpassing previous timekeeping methods, with the decision to officially define the SI second by the properties of caesium-133 being made in 1967. Current strontium atomic clocks are capable of a total uncertainty of 2.1×10^{-18} in fractional frequency units [23][24][25][26].

In 1991, Kasevich and Chu demonstrated matter-wave interference with laser-cooled sodium atoms [27]. In contrast to Ramsey's technique, Kasevich and Chu used Raman transitions to interfere the external rather than internal states of atoms [24], an achievement previously thought impossible due to de Broglie phase instability. This dependence on atomic external states quickly led to atoms being used to probe external fields, in much the same way neutron interference had previously been used to measure gravitational acceleration [28] [29]. The ability to laser-cool atoms to micro-Kelvin temperatures coupled with their larger mass opened up a whole new sensitivity domain for probing external inertial forces with interferometry.

1.1.2 Principles of Atom Interferometry

Atom interferometers rely upon the principle of *coherent* control of atomic de Broglie waves [1]. If coherent control of the atoms is achieved, offering the atoms multiple indistinguishable paths will cause the wavefunction to split, with a well-known initial relative phase between the paths. The phase accumulated along each path depends upon the action, and hence upon the potentials that the atom is exposed to along each path. This action may be broken up into two parts; the free evolution action S_{path} and the external field interaction S_{field}. These potentials can be electromagnetic in origin, for example atomic interaction with laser fields causing an action S_{light}, or gravitational potentials [30].

The two or more wavepackets after travelling different paths are then brought back together, potentially resulting in interference effects. This recombination requires that the relative phase information is then converted into state population information, which can be readily measured. If the coherence is maintained during the whole procedure, for both the atoms and the laser fields, the phase difference between the paths can then be inferred from the interference fringes and hence the potentials measured to extremely high precision. In this way, atom interferometers offer some of the most precise measurements of local gravity g with a sensitivity of 6.7×10^{-12} g per shot [31].

1.2 Discussion of Experiment

Development of an atom interferometer at the University of Liverpool began in earnest in late 2013, with the aim of using atom interferometers for fundamental physics searches, complementary to the successful particle physics research already performed at Liverpool. The experiment uses rubidium-85 as an atomic source and two laser beams to perform state manipulation via stimulated Raman transitions between the two hyperfine ground states. Rubidium-85 is not as commonly used in atom interferometry as rubidium-87, with the decision to use rubidium-85 as the atomic species influenced by its smaller hyperfine splitting,

allowing the use of a relatively inexpensive RF signal generator. The atom interferometry experimental procedure is as follows, see figure 1.1 (more details can be found in chapter 3, as well as in [32] [33]):

Step 1 The atoms are initially confined in a magneto-optical trap (MOT), made up of an anti-Helmholtz configuration magnetic field and three pairs of circularly polarised, counter-propagating beams which are red-detuned from resonance. Whilst trapped in the MOT the atoms are Doppler cooled to approximately 150 μK [34].

Step 2 In order to reach temperatures below the Doppler limit, an optical molasses is produced. This involves switching the magnetic field off and further detuning the lasers, allowing polarisation gradient cooling to reduce the atom cloud temperature to a few μK.

Step 3 A state preparation phase then occurs, ensuring that all of the atoms begin the interferometry sequence in the $|s\rangle = |g\rangle$ state, where $s = \{g, e\}$ is the label for the hyperfine internal states.

Step 4 The atom cloud is then exposed to the Raman beams for a duration $t_{\pi/2}$ designed to create a '$\pi/2$' or 'beam-splitter' pulse, analogous to the beam splitter in a Mach-Zehnder light interferometer. This acts to create an equal superposition between the ground and excited states, $|g\rangle$ and $|e\rangle$, with a momentum splitting between the two states which causes them to begin to spatially separate.

Step 5 The atoms are then allowed to propagate freely for a time T, without interacting with the Raman beams. During this time, the atom wavefunction splits and travels along two paths.

Step 6 A second pulse is then applied of duration equal to twice the beam-splitter pulse, called a 'π' or 'mirror' pulse. This interchanges the state population of the superposition, so that $|g\rangle \rightarrow |e\rangle$ and $|e\rangle \rightarrow |g\rangle$.

Step 7 A second free propagation time of time T is then inserted. During this time, the separated wave packets are brought back together and overlap due to the interaction with the π pulse.

Step 8 A final beam-splitter pulse is then performed, which acts to recombine the two wavepackets. In the absence of any external forces, all of the atoms will be placed back into the ground state.

Step 9 Finally, the atomic state populations are measured by a series of state detection pulses, fluorescing the atoms. This fluorescence is measured and the intensity is proportional to the state population. If the state detection system measures a non-zero $|e\rangle$ state population, the atoms must have picked up an extra phase from another source such as an external potential. In this way, measurement of the excited state population allows the inference of the phase difference between the paths. Thus, the advantage of the $\pi/2 - \pi - \pi/2$ sequence is that it forces the atoms to travel along two different spacetime paths, with accumulated phase difference acting as a sensitive probe of external potentials.

1.3 Dark Energy Searches

In 1998, it was discovered via astronomical observations that the universe is not simply expanding but the rate of expansion is increasing with time [36]. To accommodate this phenomenon in terms of general relativity, an extra term was added to the Einstein Field Equations (EFEs) to create a uniform negative pressure and hence an inflationary effect. The source of this negative pressure was dubbed *Dark Energy* (DE) and calculations showed that it would have to make up around 70% of the total energy in the observable universe to account for the observed rate of expansion [37][38][39].

Despite modification of the EFEs providing a convincing explanation for the observed acceleration, no theoretical explanation in terms of quantum fields has been widely accepted

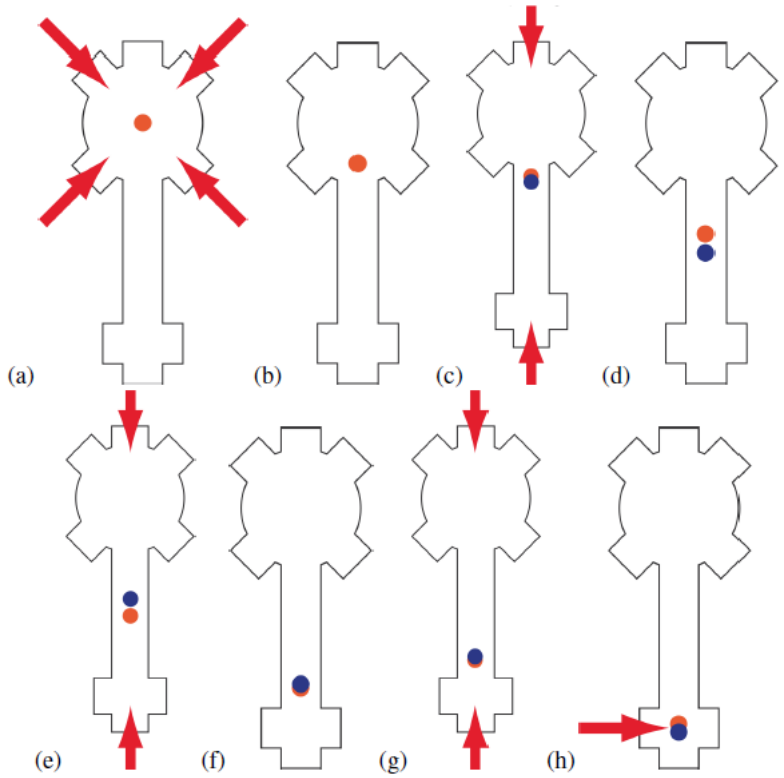

Fig. 1.1 Schematic representation of the interferometry sequence [35]. The atoms are cooled and state selected at stage (a), then released to fall down the interferometry pipe at (b). Raman beams put the atoms into a superposition of states at (c), represented by red and blue circles. (d) is a propagation time T, after which a second pulse reverses the states of the wavepackets (e). (f) is another propagation time T. At (g), the two wavepackets now overlap again, and a final Raman pulse is applied. Finally, the state detection pulses are applied at (h), measuring the population discrepancy from the original population in (b).

[40][41][42], with every current source of experimental evidence for dark energy coming from cosmological observations. In order to provide a quantum explanation for dark energy, a measurement of the small-scale structure of the dark energy field may provide insight, providing an incentive for experiments which are very sensitive to quantum fields, such as atom interferometers, to be designed with this specific purpose in mind.

The low energy density of the dark energy field might make it seem that measurement is near-impossible, but this is not so. The calculated energy density of a uniform dark energy field is $\rho_{DE} = 6.3 \times 10^{-10}$ J/m^3. An electric field with an energy density $\rho_{DE} = 100\rho_E$ would equate to an electric field strength of about 1 V/m, easily detectable in the laboratory.

The problem therefore is not the energy density itself, but the homogeneity of the field and the unknown coupling to ordinary matter.

To address this, a pair of assumptions are made which must be met for an atom interferometric experiment to detect the effects of dark energy on the laboratory scale [43]:

- The DCV has an non-uniform spatial distribution, causing the phase ϕ_{DCV} accumulated along each arm to be path-dependent.
- There exists a non-gravitational interaction between the atoms and the DCV.

The first assumption is in contrast to the cosmological constant model of dark energy. This model adds a scalar field to the EFEs of the form $\Lambda g_{\mu\nu}$, where Λ is the cosmological constant. The independence of the scalar field Λ on position is in turn based on the theory that Λ is caused by vacuum fluctuations in quantum field theory. Quantum field theory calculations of the vacuum energy are, however, known to have serious difficulty accounting for the observed magnitude of the cosmological constant, casting some doubt on this uniformity assumption [44][45]. The second assumption is required because any phase shift caused by gravitational interaction with a dark energy field would be far too small to be observed by current atom interferometers.

An overview of the proposed interferometry setup is shown in figure 1.2. A pair of atom interferometers A and B are separated by a baseline distance d. The interferometers are of near-identical construction and close enough together to be in the same noise envelope, using the same lasers for the interferometry pulses. Constructing them this way causes all sources of common noise to cancel, meaning that when they make simultaneous measurements, both should measure the same phase change. The difference in phase between the interferometer pair, $\Delta\Phi = \phi_A - \phi_B$, is therefore expected to be zero, even for a uniform DCV interaction. A non-uniform field will cause a difference in accumulated phase between the arms which, provided the signal is above the noise background, will cause $\Delta\Phi \neq 0$ and potentially indicate the presence of a non-uniform DCV field.

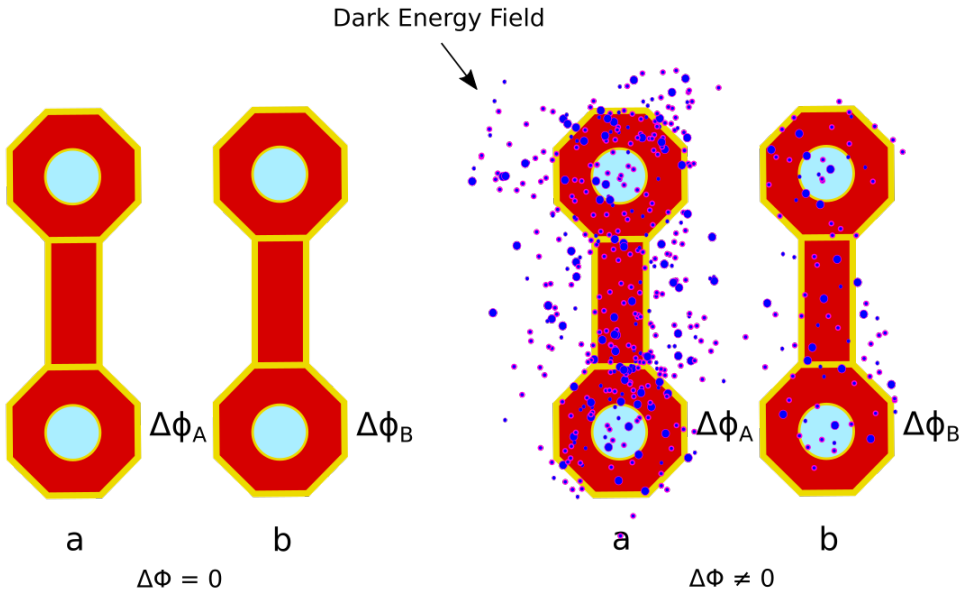

Fig. 1.2 Two interferometers are positioned in the same noise envelope and using the same lasers, but separated by some baseline distance. The difference in phase between the interferometers, $\Delta(\Delta\phi) \equiv \Delta\Phi$, is expected to be zero, with all sources of phase noise common to both interferometers. Any deviation from $\Delta(\Delta\phi) = 0$ could be evidence of a dark energy field gradient between the two arms.

Measurement of a potential dark content of the vacuum on the laboratory is the eventual aim of this experiment. This thesis, however, is primarily concerned with laying the foundational work for this project by achieving coherent control and interference of atomic states.

Chapter 2

Atom Interferometry Theory

2.1 Laser Cooling and Atom Trapping

2.1.1 Doppler cooling and the Doppler Limit

Laser fields may be used to drastically reduce the temperature of neutral atoms via the Doppler cooling technique. This can reduce the velocity of thermal atoms from 100s of m/s to a few cm/s [46], allowing atoms to be trapped in a potential well via magnetic fields and experimented on for a time frame of order seconds.

The advantages of ultra-cold over thermal atoms are several. Firstly, the atoms have a longer mean-free path and so are less likely to undergo collisions which may change the state of the atoms. Secondly, lowering the temperature keeps the atoms from escaping the parameters of the laser beams which are of order a few centimetres. Finally, the Doppler broadening of the state transitions is reduced by having low temperatures, allowing effects such as Zeeman splitting of the hyperfine states to be observed.

Doppler cooling involves an atom preferentially absorbing photons from the opposing direction to its velocity and subsequently emitting them in a random direction, causing

an effective direction-dependant frictional force and hence a reduction in velocity. This scattering force takes the form [47]

$$F_{scatt} = \frac{\Delta p}{\Delta t} = \frac{\Delta N}{\Delta t} P_{photon}, \tag{2.1}$$

where $\Delta N/\Delta t$ is the number of photons scattered per second, usually referred to as the *scattering rate*, R_{scatt}. The scattering rate for a transition depends upon the intensity of the laser fields I, the saturation intensity for this transition I_{sat}, the linewidth of the resonance Γ and the detuning from the resonance peak δ as described by the equation

$$R_{scatt} = \frac{\Gamma}{2} \frac{\frac{I}{I_{sat}}}{1 + \frac{I}{I_{sat}} + \frac{4\delta^2}{\Gamma^2}}, \tag{2.2}$$

where the saturation intensity is defined as the intensity required to excite half of the atoms into the upper state at equilibrium. For a single photon momentum of $\hbar k$, this gives a scattering force of

$$F_{scatt} = \hbar k \frac{\Gamma}{2} \frac{\frac{I}{I_{sat}}}{1 + \frac{I}{I_{sat}} + \frac{4\delta^2}{\Gamma^2}}. \tag{2.3}$$

For small detuning, $\delta \ll \Gamma$ and at saturation intensity, the scattering rate becomes $\Gamma/4$. When $I \gg I_{sat}$, the scattering force approaches the maximum value of

$$F_{max} = \hbar k \frac{\Gamma}{2}. \tag{2.4}$$

If a beam of atoms is arranged to be travelling towards a laser beam which is resonant with an atomic transition, the frequency of the light will appear blue shifted from resonance due to the Doppler shift of the atoms travelling towards the beam. If the beam is therefore deliberately red-shifted below resonance, this will cancel the Doppler effect and cause the scattering rate to increase via equation 2.2.

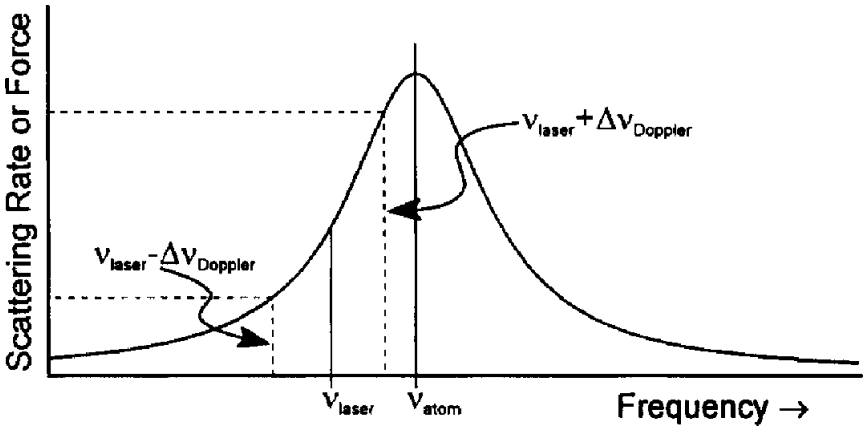

Fig. 2.1 Plot of the scattering rate as a function of optical frequency. The dashed lines show how atoms with equal but opposite Doppler shifts relative to the beam experience a drastic change in scattering rate [48].

To cool an atomic vapour in three dimensions, three pairs of these detuned orthogonal beams are generally required. This technique is referred to as an *optical molasses*. Atoms moving towards any of these six laser beams will preferentially scatter atoms from this beam, resulting in a 3-dimensional cooling effect. This technique does have its limits, with a minimum expected temperature set by the *Doppler cooling limit*

$$T_D = \frac{\hbar\Gamma}{2k_B}, \tag{2.5}$$

where k_B is Boltzmann's constant. The Doppler limit for ^{85}Rb is 145 μK.

2.1.2 Magneto-Optical Trapping

The action of the counter-propagating beams on the atoms in an optical molasses is not enough to cause atom trapping; laser cooling slows down atoms but it does not confine them to a particular position. By adding an inhomogeneous magnetic field superimposed over the system of three pairs of orthogonal, red-detuned beams, a magneto-optical trap is created. This field may be provided by a pair of coils in an anti-Helmholtz configuration. Two coils,

with opposing currents and radii equal to d, are separated by an axial distance d. These coils create a quadrupole magnetic field of the form

$$\mathbf{B}(x,y,z) = B_{grad}(-\frac{x}{2}\mathbf{i} - \frac{y}{2}\mathbf{j} + z\mathbf{k}). \tag{2.6}$$

This field configuration creates a magnetic minimum at the centre, around which the atoms cloud will coalesce. The field lines for the anti-Helmholtz configuration are shown in figure 2.2.

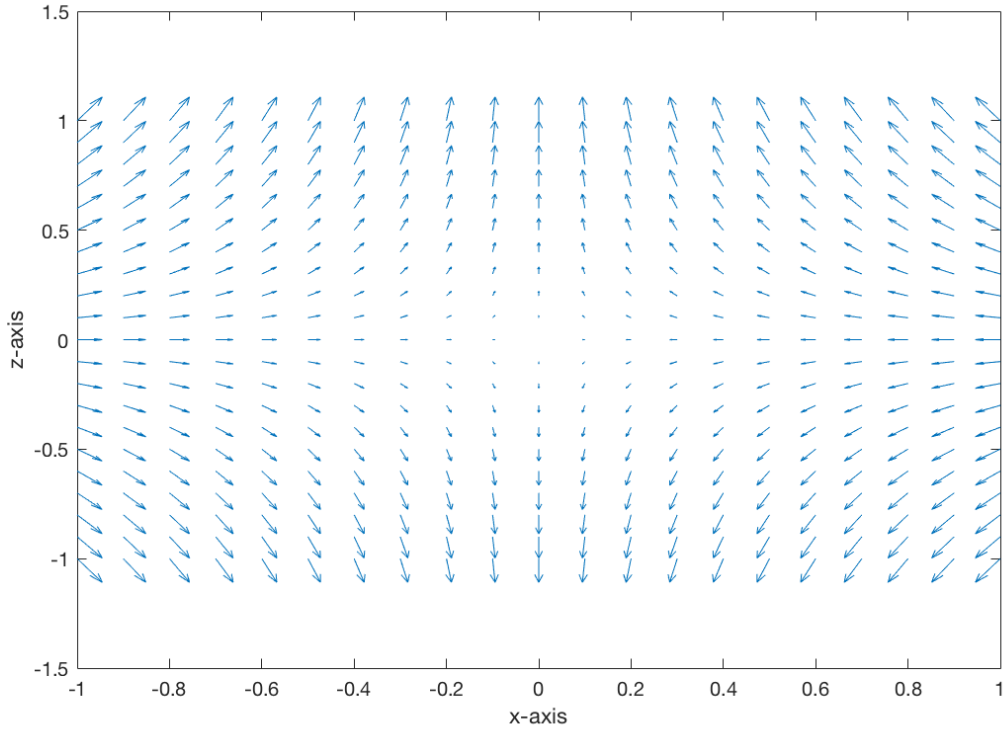

Fig. 2.2 Quiver plot representation of a two-dimensional slice of equation 2.6. This plot shows that the magnetic field grows twice as quickly along the z-axis as along the x-axis, with an associated sign change between axes. This sign change must be accounted for by beam polarisation for an atom trapping effect to be created.

This magnetic field creates a magnetic minimum at the centre that increases linearly as the atoms move in any direction.

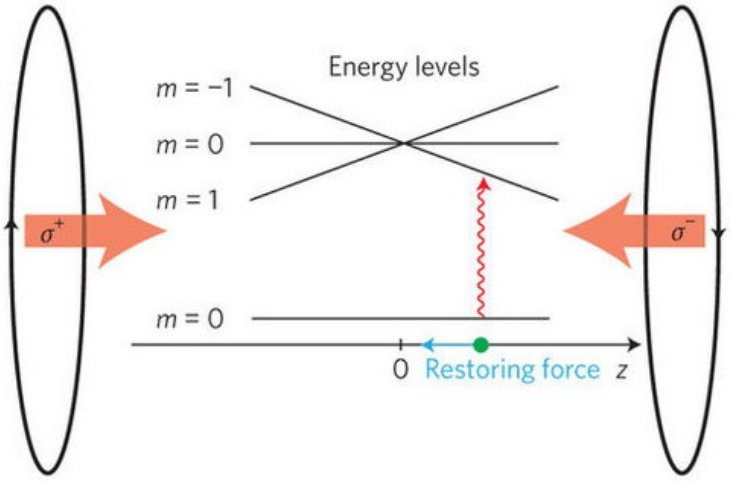

Fig. 2.3 Diagram showing the Zeeman splitting of a simple, two state system with an l = 0 ground state and an l = 1 excited state. The Zeeman shift causes the red-detuned laser to be pushed towards resonance with the m = 1 substate [49].

The magnetic field acts to split the magnetic substates m_F in terms of energy (see figure 2.3), via the Zeeman effect which, to lowest order, takes the form

$$\Delta E = \mu_B g_F m_F |B|, \tag{2.7}$$

where μ_B is the Bohr magneton and g_F is the Landé g-factor for the hyperfine state.

By splitting the atomic states and red detuning the cooling laser, states which have a lower energy due to the Zeeman effect are pushed closer to resonance. Light with a polarisation which satisfies the angular momentum constraints of these transitions is therefore more likely to be absorbed. Therefore, by choosing the beam polarisations to match this criterion, it is possible to create a position-dependent force on the atoms to constrain them around the magnetic minimum.

By fixing all six MOT beams to be circularly polarised and the anti-Helmholtz coils creating a field which is always parallel to the beam propagation direction, the selection rules are fixed

to be $\Delta m_F = \pm 1$. The $F' = 4$ state is split into nine magnetic substates, and $F = 3$ into seven. The polarisation of the beams which causes a constraining force must be matched to the magnetic field direction; reversal of the magnetic field requires the polarisation handedness to be flipped for the MOT to still function.

Any atomic species which is to be cooled via this method must have an energy level structure containing a *closed optical loop*, so that once an atom absorbs a cooling photon and is excited to a higher state, it reliably returns to its original ground state and may repeat the cooling process. In the case of ^{85}Rb, the cooling laser is red-detuned from the $5^2S_{1/2},\ F = 3 \rightarrow 5^2P_{3/2},\ F' = 4$ transition (see figure 2.4). This frequency predominantly excites atoms to the $F' = 4$ state which then decays to the $F = 3$ state.

A MOT setup with only the $5^2S_{1/2},\ F = 3 \rightarrow 5^2P_{3/2},\ F' = 4$ transition frequency light will quickly disappear, however, due to transitions of the form $5^2S_{1/2},\ F = 3 \rightarrow 5^2P_{3/2},\ F' = 3 \rightarrow 5^2S_{1/2},\ F = 2$, causing all of the atoms to fall into the $F = 2$ 'dark state' and out of the cooling cycle. To remedy this, a second frequency called the *repumper* frequency is introduced, causing the transition $5^2S_{1/2},\ F = 2 \rightarrow 5^2P_{3/2},\ F' = 3 \rightarrow 5^2S_{1/2},\ F = 3$ and moving the atoms back into the cooling cycle.

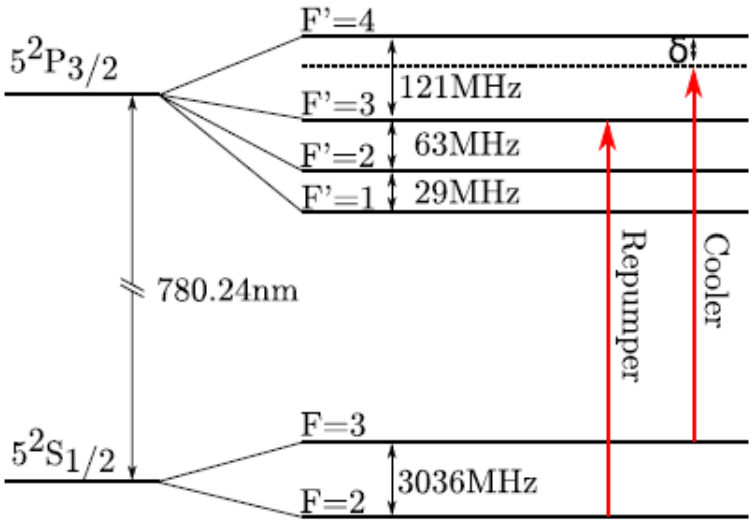

Fig. 2.4 Energy level diagram for rubidium-85. The hyperfine ground and excited states have total angular momentum values F = 2 and F = 3 respectively [50][51].

2.1.3 Sub-Doppler Cooling

In order to reach temperatures below the Doppler limit, a technique called *polarisation-gradient cooling* (PGC) is used. This involves switching the magnetic field off and increasing the detuning of the cooling beams, effectively returning to an optical molasses configuration. The atom cloud then expands in the beams, causing a cooling effect which can go below the Doppler limit and reach micro-Kelvin temperatures. This technique relies upon both beams being derived from the same laser, making them coherent.

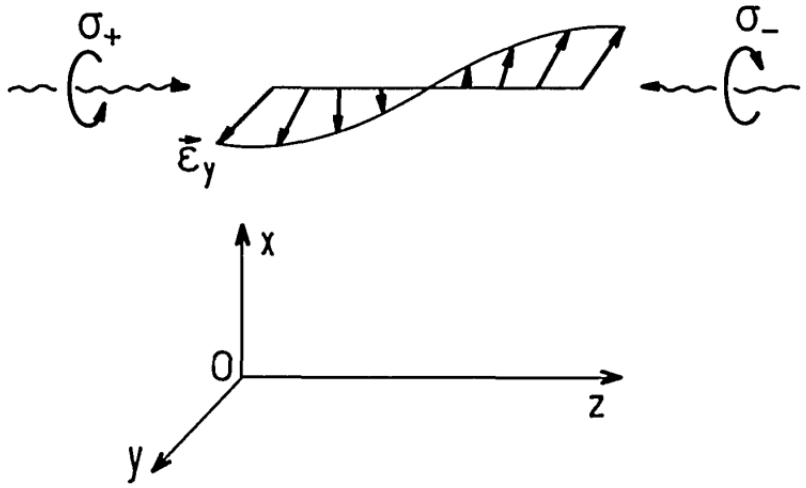

Fig. 2.5 The superposition of $\sigma^+ - \sigma^-$ beams creates a linearly polarised field which rotates around the z-axis. [52].

The PGC technique typically used in a MOT configuration involves $\sigma^+ - \sigma^-$ polarised beams. In one dimension, the superposition of these beams results in a linear polarisation axis which rotates around the axis of propagation z by the angle $\phi = -kz$, where k is the wavevector of the beams (see figure 2.5). In the case of a stationary atom, the linearly polarised light will drive π transitions (see section 2.4) which, due to the Clebsch-Gordan coefficients, will cause the state g_0 to be preferentially populated (figure 2.6).

In the case of a moving atom, however, a stationary coordinate system is transformed to a co-moving system, to keep the direction of polarisation constant. This results in an inertial potential energy term of the form $V = kvJ_z$, where v is the atomic velocity and J_z is the angular momentum operator in the z direction. This inertial term introduces couplings between the

magnetic substates, shown by the double arrows in figure 2.6, known as adiabatic couplings which disappear as $v \to 0$. These couplings are strongly directionally dependent, creating a force which opposes the direction of motion. This velocity-dependant force leads to an effect called *motion-induced orientation*. This in turn leads to the photon absorption amplitude being directionally dependent, resulting in a frictional force [52][53].

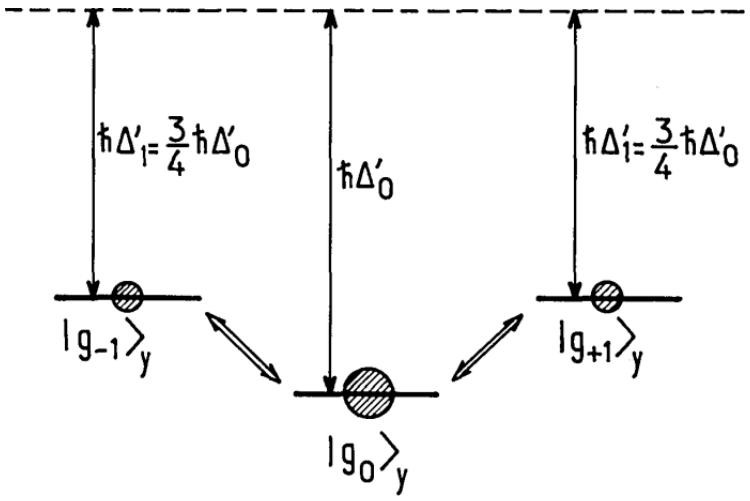

Fig. 2.6 Magnetic substates for a J = 1 ground state. The filled circles represent the steady state populations of each state when the atom is stationary. The AC Stark effect causes the energy level difference shown between g_0 and $g_{\pm 1}$ [52].

The lower temperature limit to this method is called the *recoil limit* where the recoil temperature is defined as

$$T_r = \frac{(\hbar k)^2}{k_B m_A}, \tag{2.8}$$

where m_A is the atomic mass. This is the temperature corresponding to atoms with an average momentum equal to the momentum of one photon with the wavevector k and has a value for rubidium-85 of $T_r \approx 370$ nK [34][54].

2.2 Atomic Interaction with Radiation

2.2.1 Two-Level Systems

Alkali metals have an electron structure of a single valence electron outside of a group of closed electron shells. This makes these metals 'hydrogen-like' and therefore the next simplest atoms to analyse after hydrogen itself. Due to their simplicity, and their susceptibility to laser-cooling methods, alkali metals such as ^{85}Rb are ideal candidates for atomic species in interferometry experiments. The hyperfine states of rubidium-85 are labelled $F = 2$ and $F = 3$, where F is defined as the total angular momentum quantum number $F = I + L + S = I + J$. The quantities I, L and S here are the nuclear, orbital and spin angular momentum numbers respectively.

The two hyperfine ground states of ^{85}Rb are a good approximation to a two-state system due to their splitting, $\omega \approx 2\pi\times$ 3.04 GHz, being a factor 10^5 smaller than the separation between the $5^2S_{1/2}$ and $5^2P_{3/2}$ states (see figure 2.4). The quantum mechanical behaviour of a two-state system is well understood, allowing the hyperfine state manipulations of ^{85}Rb to be readily compared to theory. Additionally, the excited hyperfine state of ^{85}Rb has a lifetime of order seconds, meaning that spontaneous decay to the ground state is highly unlikely over the time frames of the experiment.

For the purposes of this work a semi-classical treatment is used. This involves treating the radiation as a classical, oscillating electric field but the atom as a quantized, two-state system[1]. This will allow the derivation of equations required for chapters 4 and 5.

The Hamiltonian for the interacting system is composed of two terms,

$$H = H_0 + H_I(t). \tag{2.9}$$

[1] A three-state system is briefly introduced to describe Raman transitions, which eventually reduces to a two-state system

The first term is the time-independent Hamiltonian for the unperturbed system; the eigenfunctions of H_0 are simply the wavefunctions for a non-interacting system. Taking the $F = 2$ state eigenvector to be $|g\rangle$ and the $F = 3$ eigenvector to be $|e\rangle$, this leads to the equations

$$H_0 |g\rangle = E_g |g\rangle = \hbar\omega_g |g\rangle \tag{2.10a}$$

and

$$H_0 |e\rangle = E_e |e\rangle = \hbar\omega_e |e\rangle , \tag{2.10b}$$

where E_g and E_e are the energies of the $|g\rangle$ and $|e\rangle$ levels, which are assumed to be orthonormal. Any general state vector $|\Psi\rangle$ consists of a superposition of the states $|g\rangle$ and $|e\rangle$,

$$|\Psi(t)\rangle = |g\rangle \langle g|\Psi\rangle + |e\rangle \langle e|\Psi\rangle = a_g(t) |g\rangle + a_e(t) |e\rangle , \tag{2.11}$$

where $\langle g|\Psi\rangle$ and $\langle e|\Psi\rangle$ are the time-dependent amplitudes for the system to be measured in the ground and excited states respectively.

The radiation-dependent components of the amplitudes may be factored out to give

$$a_g(t) = c_g(t) e^{-i\omega_g t} \tag{2.12a}$$

$$a_e(t) = c_e(t) e^{-i\omega_e t} . \tag{2.12b}$$

This results in a general state vector of the form

$$|\Psi(t)\rangle = c_g(t)\,|g\rangle\, e^{-i\omega_g t} + c_e(t)\,|e\rangle\, e^{-i\omega_e t}. \tag{2.13}$$

2.2.2 Interaction Hamiltonian

The term $H_I(t)$ is the perturbation caused by the oscillating electric field. For a monochromatic electromagnetic field, the electric field component takes the classical form $\vec{E} = \vec{E}_0\cos(\omega t)$ with angular frequency ω interacting with an electric dipole $\vec{d} = e\vec{r}$, giving the interaction Hamiltonian

$$H_I(t) = -\vec{d}\cdot\vec{E} = e\vec{r}\cdot\vec{E}_0\cos(\omega t), \tag{2.14}$$

representing the potential energy of a dipole in a sinusoidally oscillating electric field.

By using equation 2.13 as the general state vector for this two-state system, and inserting equation 2.9 for the complete Hamiltonian into the time-dependant Schrödinger equation gives

$$(H_0 + H_I)(c_g(t)\,|g\rangle\, e^{-i\omega_g t} + c_e(t)\,|e\rangle\, e^{-i\omega_e t}) = i\hbar\frac{d}{dt}(c_g(t)\,|g\rangle\, e^{-i\omega_g t} + c_e(t)\,|e\rangle\, e^{-i\omega_e t}). \tag{2.15}$$

Differentiating and using equations 2.10 to cancel like terms results in

$$H_I[c_g(t)\,|g\rangle\, e^{-i\omega_g t} + c_e(t)\,|e\rangle\, e^{-i\omega_e t}] = i\hbar[\frac{d(c_g(t))}{dt}\,|g\rangle\, e^{-i\omega_g t} + \frac{d(c_e(t))}{dt}\,|e\rangle\, e^{-i\omega_e t}]. \tag{2.16}$$

Taking the inner products of the above equation with $\langle g|$ and $\langle e|$ and noting that for a dipole field, $\langle g|\,H_I\,|g\rangle = \langle e|\,H_I\,|e\rangle = 0$, gives the equations

$$i\frac{d}{dt}c_g(t) = \Omega\cos(\omega t)e^{-i\omega_0 t}c_e(t) \tag{2.17a}$$

and

$$i\frac{d}{dt}c_e(t) = \Omega^*\cos(\omega t)e^{i\omega_0 t}c_g(t) \tag{2.17b}$$

respectively [55]. The parameter ω_0 is the difference between the two state frequencies, $\omega_0 = \omega_e - \omega_g$, and Ω is called the *Rabi frequency* and is defined as

$$\Omega \equiv \frac{\langle g|\, e\vec{r}\cdot\vec{E}_0\,|e\rangle}{\hbar}, \tag{2.18}$$

with Ω^* the Hermitian adjoint of Ω. These matrix elements describe the transition strength and are dependent upon overlap between the electric field polarisation and the electric dipole alignment vectors.

The sinusoidal term in equations 2.17 can be expanded as

$$\cos(\omega t) = \frac{1}{2}(e^{i\omega t} + e^{-i\omega t}). \tag{2.19}$$

Inserting 2.19 into equation 2.17a gives

$$i\frac{dc_g}{dt} = \frac{\Omega}{2}\left\{e^{i(\omega-\omega_0)t} + e^{-i(\omega+\omega_0)t}\right\}c_e. \tag{2.20}$$

where the amplitude time dependencies have been made implicit. Assuming that the electric field frequency is near resonance, $\omega \approx \omega_0$, the $\omega + \omega_0$ term oscillates much faster than the $\omega - \omega_0$ term. Over any appreciable integration time, therefore, the different frequencies in the integral of the $\omega + \omega_0$ term will cancel out and this term will average to zero. This is known as the rotating-wave approximation.

Neglecting these $\omega + \omega_0$ terms in the expansion of equations 2.17a and 2.17b via 2.19 result in the equations

$$i\frac{dc_g}{dt} = e^{i(\omega-\omega_0)t}\frac{\Omega}{2}c_e, \tag{2.21a}$$

and

$$i\frac{dc_e}{dt} = e^{-i(\omega-\omega_0)t}\frac{\Omega^*}{2}c_g. \tag{2.21b}$$

Combining 2.21a and 2.21b gives the second-order differential equation

$$\frac{d^2c_e}{dt^2} + i(\omega-\omega_0)\frac{dc_e}{dt} + \left|\frac{\Omega}{2}\right|^2 c_e = 0. \tag{2.22}$$

Taking the initial conditions $c_g(0) = 1$ and $c_e(0) = 0$ and solving equation 2.22 results in the amplitudes for the ground and excited states

$$c_g(t) = e^{i\delta t/2}\left[\cos\left(\frac{\Omega_D t}{2}\right) - i\frac{\delta}{\Omega_D}\sin\left(\frac{\Omega_D t}{2}\right)\right], \tag{2.23a}$$

$$c_e(t) = -ie^{-i\delta t/2}\frac{\Omega}{\Omega_D}\sin\left(\frac{\Omega_D t}{2}\right), \tag{2.23b}$$

where Ω_D is defined as

$$\Omega_D^2 \equiv \Omega^2 + (\omega-\omega_0)^2 \tag{2.24}$$

and the detuning δ is

$$\delta \equiv \omega - \omega_0. \tag{2.25}$$

Multiplying equation 2.23b by its complex conjugate results in the equation for the excited state probability P_e,

$$P_e = |c_e(t)|^2 = \frac{\Omega^2}{\Omega_D^2}\sin^2\left(\frac{\Omega_D t}{2}\right), \tag{2.26}$$

For on-resonant light interactions, equation 2.26 reduces to

$$|c_e(t)|^2 = \sin^2\left(\frac{\Omega t}{2}\right). \tag{2.27}$$

This sinusoidal change in the state population as pulse time is varied is called a *Rabi oscillation*.

For off-resonant interaction, $\omega \neq \omega_0$, equation 2.26 is required. Figure 2.7 shows the expected change in state population as the electric field frequency is scanned across resonance. The detuning $\delta \equiv \omega - \omega_0$ is varied and plotted in units of Ω. Making the substitution $\delta = k\Omega$ and setting the time t to be a π pulse $t = \pi/\Omega$ reduces equation 2.26 to

$$|c_e|^2 = \frac{1}{1+k^2}\sin^2\left(\frac{\pi}{2}\sqrt{1+k^2}\right). \tag{2.28}$$

This function is plotted in figure 2.7 and displays a sinc-like distribution, with lobes either side of the main resonance. The shape of this distribution is caused by the square nature of the assumed Raman pulse; the Fourier transform of a 'box' function is a sinc function. The shape of the resonance can therefore be manipulated by changing the temporal intensity profile of the Raman pulse. This becomes of particular importance for counter-propagating beams, where the Doppler shift of the atoms will also vary over the duration of the pulse and affect the fidelity of the state population transfer pulses. This problem can be solved either

by having very short, intense pulses or via the method of pulse shaping, creating a desired pulse shape which will correct for these Doppler-induced effects [56][57][58].

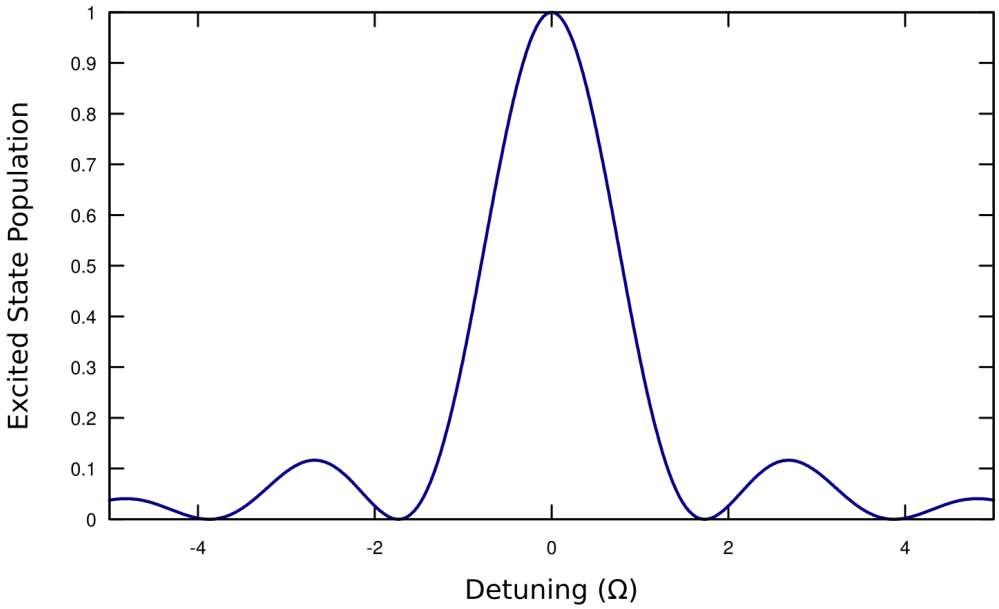

Fig. 2.7 Frequency scan over resonance displays a sinc-squared function profile. The pulse time t in equation 2.26 is kept constant and is selected so that the amplitude is equal to unity when $\omega - \omega_0$ is zero, in other words it has the duration of a π pulse.

Plotting the state population as the pulse time t is varied produces the expected Rabi oscillations. Figure 2.8 displays Rabi oscillations for various values of δ, where $\delta = 0$ is the maximum amplitude Rabi oscillations of equation 2.27. The pulse duration is given in units of π/Ω. By setting the pulse frequency to be off-resonance, the Rabi oscillations both decrease in amplitude and increase in frequency.

For a constant Rabi frequency, on-resonant light can be used to coherently and repeatably manipulate the internal states of the atoms. For an interferometer, this takes the form of π and $\pi/2$ pulses.

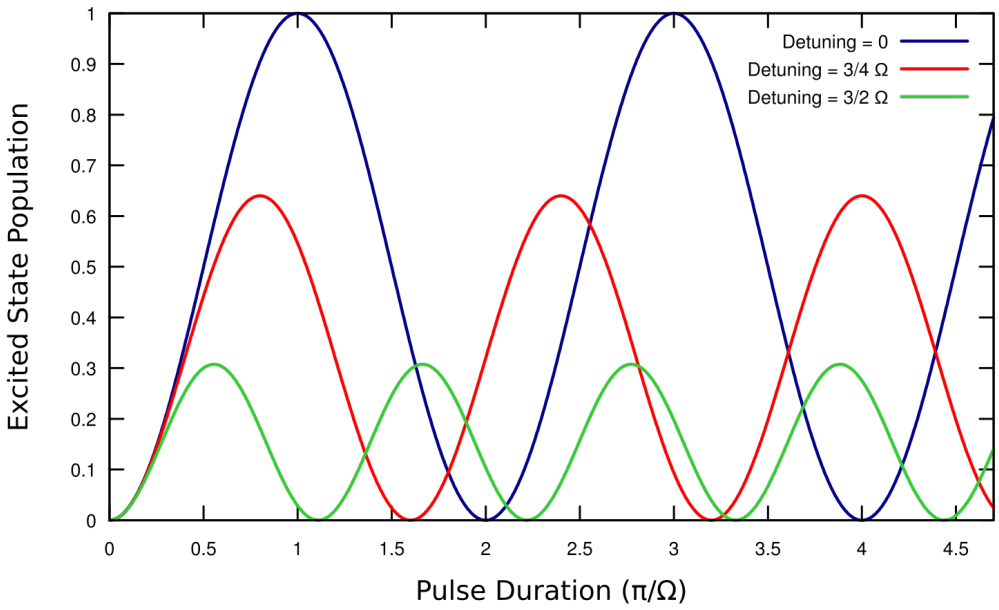

Fig. 2.8 Rabi oscillations for various detunings from resonance. By increasing detuning, more Rabi cycles are observable before any decoherence effects cause critical damping of the oscillations.

π pulse

If a group of atoms is initially prepared in the lower state $|g\rangle$, a radiation pulse of the appropriate duration will cause the population to be completely transferred to the state $|e\rangle$. This is called a π pulse, with the restriction on the pulse duration being $\Omega t = \pi$.

More generally, a π pulse will cause the transition

$$c_1 |g\rangle + c_2 |e\rangle \rightarrow -i\{c_1 |e\rangle + c_2 |g\rangle\}, \tag{2.29}$$

inverting the state populations, $|g\rangle \leftrightarrow |e\rangle$.

$\pi/2$ pulse

Instead of inverting the populations, an atomic wavefunction can be split into two equal components via a $\pi/2$ pulse, with the requirement that $\Omega t = \pi/2$. This means that an atom

initially in the $|g\rangle$ state will be in an equal superposition of both $|g\rangle$ and $|e\rangle$ states after the $\pi/2$ pulse,

$$|g\rangle \rightarrow \frac{1}{\sqrt{2}}(|g\rangle - i|e\rangle). \tag{2.30}$$

Via π and $\pi/2$ pulses, the atomic states can be coherently controlled, allowing the atoms to travel along different paths to reach a final state and hence cause interference effects.

2.3 Raman Transitions

The manipulation of atomic internal states may be performed via *Raman transitions*. These occur when an atom interacts simultaneously with two electric fields. An atom initially in the ground state $|g\rangle$ will absorb a photon from one field, causing it to become excited to an intermediate, virtual state. Interaction with the second field causes stimulated emission of a photon, resulting in the atomic transition to the higher state $|e\rangle$, see figure 2.9. Two-photon transitions have an associated wavevector $\vec{k}_{\text{eff}}$ which depends on the relative orientation of the beams. For counter-propagating beams, $\vec{k}_{\text{eff}} = \vec{k}_1 - \vec{k}_2$. To avoid actually populating any real intermediate states, the virtual state is detuned away from resonant frequency with respect to any single-photon transition levels, making the amplitude for these transitions negligible. The atom interacts with electric fields of the form

$$\vec{E}(t) = \vec{E}_1 \cos(\omega_1 t + \phi_1) + \vec{E}_2 \cos(\omega_2 t + \phi_2). \tag{2.31}$$

The two-photon detuning from resonance δ is defined as

$$\delta \equiv \omega_{\text{eff}} - \omega_0 = (\omega_1 - \omega_2) - (\omega_e - \omega_g) \tag{2.32}$$

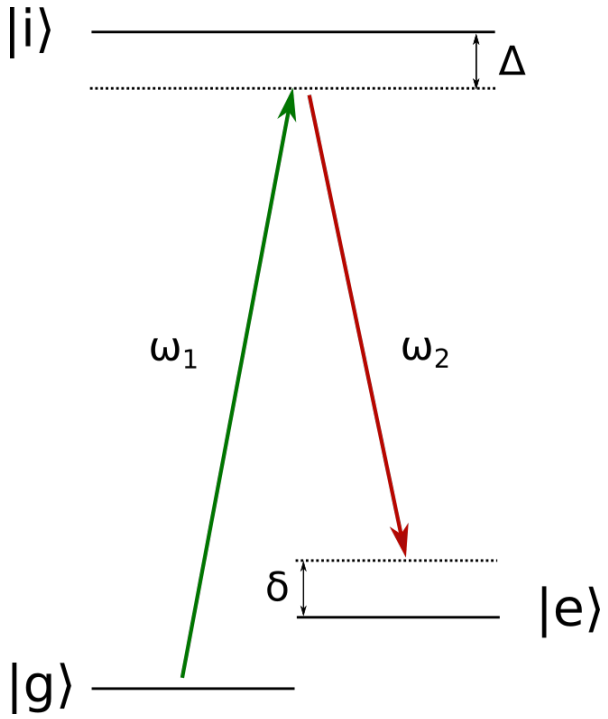

Fig. 2.9 The coupling of two states via a higher, intermediate state is called a lambda system. Increasing Δ while simultaneously satisfying the resonance condition makes transition to the excited state $|i\rangle$, and therefore single-photon decoherence, less likely.

where $\omega_{\text{eff}} = \omega_0$ is the resonance definition. Each electric field also has a detuning from the state $|i\rangle$ defined as

$$\Delta_1 = \omega_1 - (\omega_i - \omega_g), \tag{2.33a}$$

$$\Delta_2 = \omega_2 - (\omega_i - \omega_e), \tag{2.33b}$$

meaning that the two photon detuning can also be defined as

$$\delta \equiv \Delta_1 - \Delta_2. \tag{2.34}$$

The total two-photon detuning from $|i\rangle$ is then given by

$$\Delta = (\Delta_1 + \Delta_2)/2. \tag{2.35}$$

To ensure that atoms are excited to the virtual state and not the higher state $|i\rangle$, the detuning Δ must satisfy the condition

$$|\Delta| \gg \Gamma, \tag{2.36}$$

where Γ is the linewidth of the D_2 transition. This condition reduces the likelihood of spontaneous decay from $|i\rangle$, which would remove atoms from the interferometry sequence.

The three-level Hamiltonian for Raman transitions is

$$H(t) = \hbar\omega_g |g\rangle\langle g| + \hbar\omega_e |e\rangle\langle e| + \hbar\omega_i |i\rangle\langle i| - \vec{r}\cdot\vec{E}(t). \tag{2.37}$$

Solving the Schrödinger equation for a three-state system with the above Hamiltonian results in the equations

$$i\frac{dc_g}{dt} = \frac{\Omega_{gi}}{2} e^{i\Delta_1 t} c_i, \tag{2.38a}$$

$$i\frac{dc_e}{dt} = \frac{\Omega_{ie}}{2} e^{i\Delta_2 t} c_i, \tag{2.38b}$$

$$i\frac{dc_i}{dt} = \frac{\Omega_{gi}^*}{2} e^{-i\Delta_1 t} c_g + \frac{\Omega_{ie}^*}{2} e^{-i\Delta_2 t} c_e. \tag{2.38c}$$

where the rotating-wave approximation has been made, $\omega_n + \omega_i - \omega_g \gg \Delta \approx \Delta_1 \approx \Delta_2$ [59] [60].

Given that the detuning $|\Delta| \gg \Gamma$ and therefore that the intermediate state $|i\rangle$ is negligibly populated, the three-state system reduces to a two-state system. This is done via adiabatic elimination of the intermediate state [61][62]. Integrating equation 2.38c with respect to time gives

$$\int_0^t \dot{c}_i(t')dt' = \frac{-i}{2}\left(\Omega_{gi}\int_0^t e^{-i\Delta_1 t'}c_g(t')dt' + \Omega_{ie}^*\int_0^t e^{-i\Delta_2 t'}c_e(t')dt'\right). \tag{2.39}$$

By assuming that the amplitudes $c_g(t)$ and $c_e(t)$ evolve much more slowly than the $e^{-i\Delta t}$ expressions, the amplitudes can be assumed to be approximately time independent and taken outside the integrand

$$c_i(t) \approx \frac{-i}{2}\left(\Omega_{gi}c_g\int_0^t e^{-i\Delta_1 t'}dt' + \Omega_{ie}^*c_e\int_0^t e^{-i\Delta_2 t'}dt'\right). \tag{2.40}$$

Solving the integrals in the above equation gives the result

$$c_i(t) \approx \frac{\Omega_{gi}}{2\Delta_1}\left(e^{-i\Delta_1 t}-1\right)c_g(t) + \frac{\Omega_{ie}^*}{2\Delta_2}\left(e^{-i\Delta_2 t}-1\right)c_e(t). \tag{2.41}$$

The state $|i\rangle$ may now be eliminated by substituting the above equation into equations 2.38a and 2.38b. The new coupled state equations take the form

$$i\hbar\begin{bmatrix}\dot{c_g}(t)\\ \dot{c_e}(t)\end{bmatrix} = \hbar\begin{bmatrix}\frac{|\Omega_{gi}|^2}{4\Delta_1}(1-e^{i\Delta_1 t}) & \frac{\Omega_{gi}\Omega_{ie}^*}{4\Delta_2}(e^{i(\delta t+\phi)}-e^{i\Delta_1 t})\\ \frac{\Omega_{gi}^*\Omega_{ie}}{4\Delta_1}(e^{-i(\delta t+\phi)}-e^{i\Delta_2 t}) & \frac{|\Omega_{ie}|^2}{4\Delta_2}(1-e^{i\Delta_2 t})\end{bmatrix}\begin{bmatrix}c_g(t)\\ c_e(t)\end{bmatrix}. \tag{2.42}$$

Once again the rotating-wave approximation can be made, due to the fact that the single-photon terms $e^{i\Delta t}$ oscillate much more quickly than the two-photon terms $e^{-i\delta t}$. Taking this approximation the above equations become

$$i\hbar \begin{bmatrix} \dot{c_g}(t) \\ \dot{c_e}(t) \end{bmatrix} \approx \hbar \begin{bmatrix} \Omega_g^{AC} & \frac{1}{2}\Omega_{\text{eff}} e^{i(\delta t+\phi)} \\ \frac{1}{2}\Omega_{\text{eff}}^* e^{-i(\delta t+\phi)} & \Omega_e^{AC} \end{bmatrix} \begin{bmatrix} c_g(t) \\ c_e(t) \end{bmatrix}. \tag{2.43}$$

The above coupled equations link the two states, $|g\rangle$ and $|e\rangle$, where the effective Rabi frequency Ω_{eff} is defined as

$$\Omega_{\text{eff}} \equiv \frac{\Omega_{gi}\Omega_{ie}^*}{2\Delta} \tag{2.44}$$

and Ω_i^{AC} is the frequency shift of the state i caused by the AC Stark effect. The effective Rabi frequency describes how the system oscillates between the two states via two-photon interactions.

In order to have a two-photon solution for the excited state population analogous to equation 2.26, a uniform energy shift of $-\hbar(\Omega_g^{AC} + \Omega_e^{AC})/2$ is applied to the Hamiltonian in 2.43 which becomes

$$\hat{H}_{\text{eff}} = \frac{\hbar}{2} \begin{bmatrix} \Omega_g^{AC} - \Omega_e^{AC} & \Omega_{\text{eff}} e^{i(\delta t+\phi)} \\ \Omega_{\text{eff}}^* e^{-i(\delta t+\phi)} & \Omega_e^{AC} - \Omega_g^{AC} \end{bmatrix}. \tag{2.45}$$

Transforming this Hamiltonian into a frame rotating at the angular frequency δ results in

$$\hat{H}_{\text{eff}} = \frac{\hbar}{2} \begin{bmatrix} -(\delta - \delta^{AC}) & \Omega_{\text{eff}} e^{i(\delta t+\phi)} \\ \Omega_{\text{eff}}^* e^{-i(\delta t+\phi)} & \delta - \delta^{AC} \end{bmatrix}. \tag{2.46}$$

The shift in frequency, caused by the AC Stark effect, takes the form [47] [63]

$$\delta^{AC} \equiv \Omega_e^{AC} - \Omega_g^{AC}. \tag{2.47}$$

Differentiating the Schrödinger equation with the Hamiltonian 2.46 leads to a second-order equation of the form

$$\frac{d^2c_e}{dt^2} + i(\delta - \delta^{AC})\frac{dc_e}{dt} + \left(\frac{\Omega_{\text{eff}}}{2}\right)^2 c_e = 0. \tag{2.48}$$

The solution of 2.48 for the excited state amplitude is [35][64]

$$c_g(t) = e^{i(\delta-\delta^{AC})t/2}\left[\cos\left(\frac{\Omega_R t}{2}\right) - i\frac{\delta}{\Omega_R}\sin\left(\frac{\Omega_R t}{2}\right)\right], \tag{2.49a}$$

$$c_e(t) = -ie^{-i(\delta-\delta^{AC})t/2}e^{-i\phi}\frac{\Omega_{\text{eff}}}{\Omega_R}\sin\left(\frac{\Omega_R t}{2}\right). \tag{2.49b}$$

where $e^{-i\phi}$ is related to the phase difference between the two Raman beams. Squaring this equation results in the excited state probability as a function of time

$$P_e = |c_e|^2 = \frac{\Omega_{\text{eff}}^2}{\Omega_R^2}\sin^2\left(\frac{\Omega_R t}{2}\right), \tag{2.50}$$

where Ω_R is defined as

$$\Omega_R \equiv \sqrt{\Omega_{\text{eff}}^2 + (\delta - \delta^{AC})^2}. \tag{2.51}$$

These equations are essentially identical in form to those found in 2.2.2, with the addition of terms arising from the AC Stark effect and the substitution of Ω for Ω_{eff}.

2.4 Atomic Structure and Selection Rules

The two-level systems so far considered have to be modified in the presence of a magnetic field. The addition of a magnetic field, to provide a quantization axis, causes the hyperfine levels to split into $2F+1$ substates via the Zeeman effect. The permitted atomic transitions between these states are dictated by the following atomic selection rules, as shown for example in [65]

$$\Delta J = 0, \pm 1, \tag{2.52a}$$

$$\Delta L = \pm 1, \tag{2.52b}$$

$$\Delta m_F = 0, \pm 1. \tag{2.52c}$$

with the exception to 2.52a that $J = 0 \rightarrow J' = 0$ is forbidden.

The amplitude for a particular dipole transition depends not just on the detuning δ but also on the polarisation of the probing electric field, as described by 2.18, repeated below for convenience.

$$\Omega = \frac{\langle g | \, e\vec{r} \cdot \vec{E}_0 \, | e \rangle}{\hbar}. \tag{2.18}$$

The inner product of the dipole vector and the electric field vector ensures that angular momentum is conserved. This means that the amplitude for a transition caused by an electric field with a particular polarisation will depend critically on direction with respect to the quantisation axis. This gives rise to various different types of transitions:

σ^+ & σ^- transitions A circularly polarised beam of light with a wavevector component $\vec{k}$ parallel to the quantisation axis $\vec{d}$ can cause σ^+ and σ^- transitions, changing the angular momentum component Δm_F by $+1$ and -1 respectively.

π^0 transitions Linearly polarised light with a polarisation vector component *parallel* to the quantisation axis and wavevector *perpendicular* can drive a π^0 transition, with $\Delta m_F = 0$.

π^+ & π^- transitions Linearly polarised light with polarisation *perpendicular* to the quantisation axis can be decomposed into an equal superposition of σ^+ & σ^- polarisation. These are defined as $\pi^+ \equiv (\sigma^+ + \sigma^-)/\sqrt{2}$ and $\pi^- \equiv (\sigma^+ - \sigma^-)/\sqrt{2}$. These both drive transitions with $\Delta m_F = \pm 1$.

Figure 2.10 shows the two different Raman beams configurations used for atom interferometry, as permitted by the above selection rules. Having both beams co-propagating and with the same circular polarisation leads to moving atoms experiencing equal Doppler shifts with respect to the beams and so stay on resonance. Changing to a counter-propagating, linearly orthogonal setup makes the resonance velocity sensitive as the Doppler shifts do not cancel.

The co-propagating configuration is useful for early calibration of the experiment. This is due to the velocity-insensitive nature of these transitions, allowing them to address all atom velocity classes and therefore offering increased fringe visibility relative to the counter-propagating configuration. After calibration, the setup is then often switched to the counter-propagating configuration in order to become Doppler and hence gravity sensitive. The work in this thesis is primarily concerned with the co-propagating Raman beam setup.

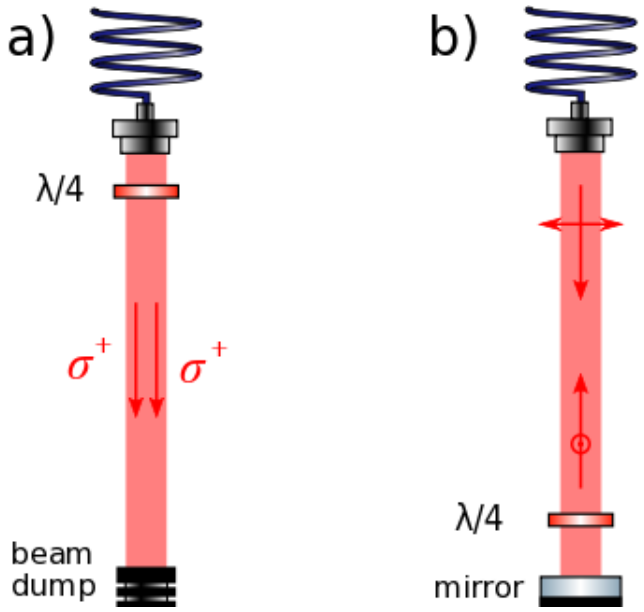

Fig. 2.10 a) Co-propagating, velocity-insensitive Raman beam configuration. b) Counter-propagating, velocity-sensitive Raman beams, with linear, orthogonal polarisation.

2.5 Interference

2.5.1 Ramsey Fringes

When the wavefunction of an atom is split into two paths and then brought back together, any difference in phase between the paths can be observed as an interference effect. This requires a multi-pulse sequence to achieve. A Ramsey pulse sequence, as discussed in chapter one, is the predominantly used interference pulse sequence for atomic clocks. It consists of a pair of $\pi/2$ pulses separated by an interval time T. The difference between this configuration and a π pulse is that there may be a phase offset between the pulses due to the interval. To see this, a two-pulse system with $T = 0$ and a non-zero phase offset is investigated. The excited state amplitude after the first pulse is simply equation 2.23b. Assuming the pulse is on resonance so $\Omega = \Omega_D$ and has a duration of $\tau = \pi/2\Omega$, equations 2.23 reduce to

$$c_g(\tau) = \frac{1}{\sqrt{2}}. \tag{2.53a}$$

$$c_e(\tau) = \frac{-i}{\sqrt{2}}. \tag{2.53b}$$

This pulse is immediately followed by a second pulse with phase offset ϕ. This transforms the Hamiltonian to

$$H_I(t) = e\vec{r}\cdot\vec{E}_0 cos(\omega_0 t + \phi). \tag{2.54}$$

Rederiving the excited state amplitude with the new Hamiltonian 2.54 leads to

$$i\frac{dc_e}{dt} = \Omega^* \cos(\omega t + \phi) e^{i\omega_0 t} c_g \tag{2.55}$$

which may be rewritten as

$$i\frac{dc_e}{dt} = \frac{\Omega^*}{2} e^{-i\phi}\left(1 + e^{2i(\omega_0+\phi)}\right) c_g \approx \frac{\Omega^*}{2} e^{-i\phi} c_g, \tag{2.56}$$

using the Euler equation and neglecting rapidly oscillating terms. Repeating this process for the ground state population via equation 2.17a and combining the two results in the second-order differential equation

$$\frac{d^2 c_e}{dt^2} + \left(\frac{|\Omega|}{2}\right)^2 c_e = 0. \tag{2.57}$$

The solution of this equation takes the form

$$c_e(t_0 + \tau) = \gamma_1 \sin\left(\frac{\Omega\tau}{2}\right) + \gamma_2 \cos\left(\frac{\Omega\tau}{2}\right), \tag{2.58}$$

where γ_1 and γ_2 are constants of integration. Differentiating equation 2.58 and equating to equation 2.55 results in

$$\gamma_1 = \frac{-ie^{-i\phi}}{\sqrt{2}}, \tag{2.59}$$

for $\tau = 0$. Equivalently, γ_2 can be found by inserting the condition $\tau = 0$ directly into 2.58 and equating with 2.53b to give

$$\gamma_2 = \frac{-i}{\sqrt{2}}. \tag{2.60}$$

Finally, inserting these constants into equation 2.58 with the condition $\Omega\tau = \pi/2$ gives the equation

$$c_e(2\tau) = -\frac{i}{2}\left(e^{-i\phi} + 1\right). \tag{2.61}$$

For $\phi = 0$, this has the same effect as twice the amplitude for one $\pi/2$ pulse, in other words a π pulse. The probability to be in the excited state is therefore

$$P_e = |c_e(2\tau)|^2 = \frac{1+\cos\phi}{2}. \tag{2.62}$$

Thus equation 2.62 shows that varying the phase between the pulses results in a sinusoidal state oscillation, demonstrating interference fringes. By the same reasoning, making the interval time T non-zero can also cause a phase offset between the pulses, once again giving interference.

To derive an equation for a non zero pulse interval, equation 2.17 is solved for the initial conditions $c_g(0) = 1$ and $c_e(0) = 0$. Integration of 2.17 gives the amplitude [47]

$$c_e(t) = \frac{\Omega^*}{2}\left\{\frac{1-\exp[i(\omega_0+\omega)t]}{\omega_0+\omega} + \frac{1-\exp[i(\omega_0-\omega)t]}{\omega_0-\omega}\right\}. \tag{2.63}$$

Once again the rotating-wave approximation is made, assuming that the radiation is close to resonance ω and that the term with $\omega_0 + \omega$ in the denominator can be neglected.

Equation 2.63 is for a single pulse of time t. For a Ramsey sequence, each atom can be excited from $|g\rangle$ to $|e\rangle$ by either the first or second pulse, so the amplitudes must be added for a pulse at time τ_p and $\tau_p + T$,

$$c_e(t) = \frac{\Omega^*}{2}\left\{\frac{1-\exp[i(\omega_0-\omega)\tau_p]}{\omega_0-\omega} + \exp[i(\omega_0-\omega)T]\frac{1-\exp[i(\omega_0-\omega)\tau_p]}{\omega_0-\omega}\right\}, \quad (2.64)$$

where τ_p is the pulse duration. Squaring the above function results in the equation

$$P_e = |c_e(t)|^2 = \left|\Omega\tau_p\right|^2\left[\frac{\sin(\delta\tau_p/2)}{\delta\tau_p/2}\right]^2\cos^2\left(\frac{\delta T}{2}\right), \quad (2.65)$$

where $\delta \equiv \omega_0 - \omega$. Equation 2.65 describes the functional form of the *Ramsey interference fringes* observed when the frequency difference δ is scanned across resonance, as shown in figure 2.11. The cosine term acts to add fringes to the sinc squared function, with a frequency proportional to the interval time T. This means that extending the interval time creates narrower and narrower fringes, allowing a much more precise measurement of the central frequency ω_0 than a simple measurement of the centre of the resonance peak would permit. This extended precision is the main reason the separated oscillating fields technique is used for atomic clocks.

2.5.2 Atom Interferometry Sequence

The Ramsey sequence creates interference between the the internal states of the atoms but, due to the imparted momentum being typically small, does not create interference between external states. For this, a pulse sequence is required which will separate the wavefunction

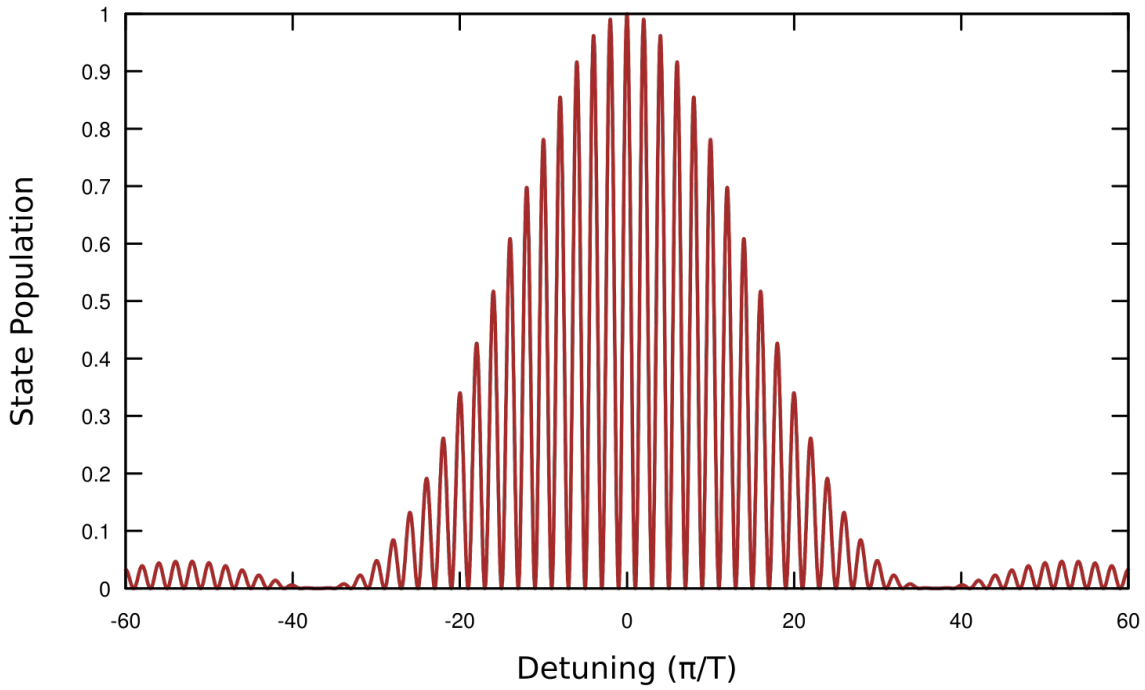

Fig. 2.11 Ramsey fringes calculation plot using equation 2.65, showing the superposition of fringes over the ordinary resonance function. The $\pi/2$ pulse duration is taken to be around 0.2 s. The state population maximum is scaled to unity.

into two spatial paths and then recombine them. This modification to the Ramsey sequence creates a Mach-Zehnder type interferometer.

The simplest way this can be achieved is by inserting a π pulse symmetrically between the $\pi/2$ pulses of the Ramsey sequence. Given that the individual photon momenta are large enough to separate the wavepackets over the time T, this sequence will create a coherent superposition along two paths which will be spatially overlap again at time $2T$. This pulse sequence of $\pi/2 - \pi - \pi/2$ creates an interferometer which is closely analogous to a Mach-Zehnder light interferometer, as shown in figure 2.12.

The total phase difference accumulated between the two paths, assuming they are overlapped at time $t = 0$, takes the form [32]

$$\Delta\phi_{total} = \Delta\phi_{light} + \Delta\phi_{path}, \tag{2.66}$$

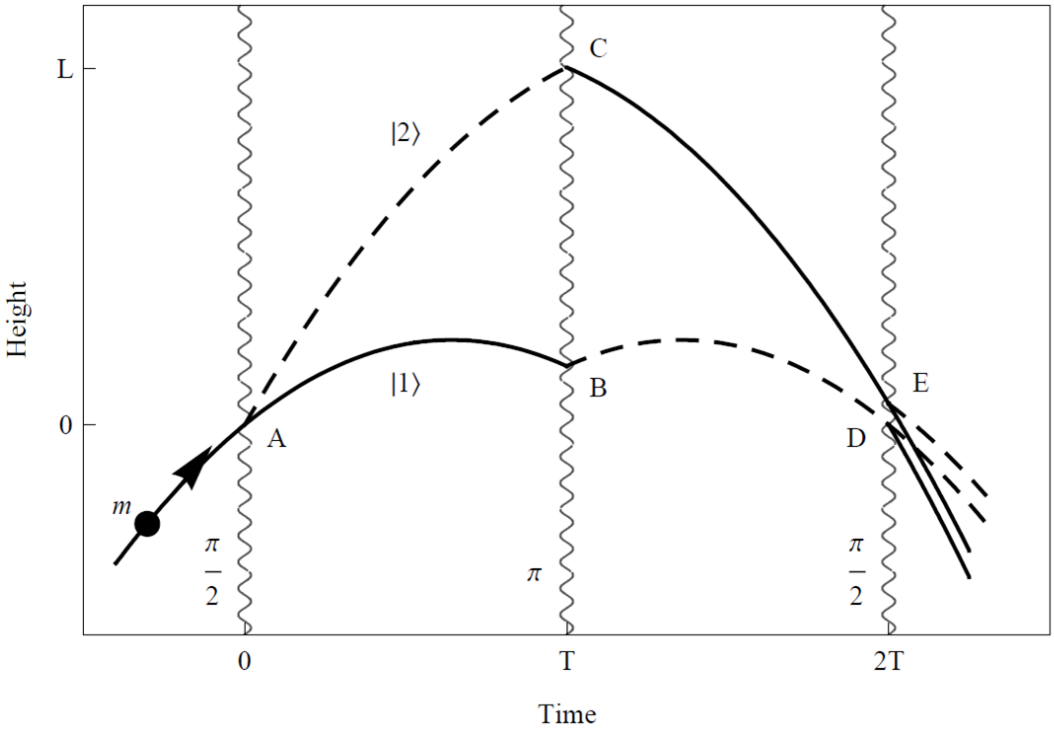

Fig. 2.12 Diagram of the Mach-Zehnder type interferometry sequence with pulse interval T, showing the trajectories of the two paths. The sensitivity of the measurement is proportional to the integrated spacetime area between the paths [66].

where $\Delta\phi_{light}$ is the phase accumulated via interaction with the interferometry pulses, and $\Delta\phi_{path}$ is the phase accumulated along each path. For atoms falling in a gravitational field which is either absent or spatially uniform, the term $\Delta\phi_{path}$ vanishes due to the fact that each of the states spend equal time travelling each path.

The phase offset from the light pulses is given by the equation

$$\Delta\phi_{light} = \sum_{PathII} \phi_j^{II} - \sum_{PathI} \phi_i^{I}, \tag{2.67}$$

where i and j run over the pulse numbers $\{1,2,3\}$. The phase factor which is collected at each laser interaction point is summarised in table 3.1.

Internal state	Momentum state	Phase factor ϕ_i
$g \rightarrow e$	$\mathbf{p} \rightarrow \mathbf{p} + \hbar\mathbf{k}_{\text{eff}}$	$\phi_{avg}^{AC} + (k_{\text{eff}} z_i - \omega_{\text{eff}} t_i - \phi_{\text{eff}}) + \pi/2$
$e \rightarrow g$	$\mathbf{p} + \hbar\mathbf{k}_{\text{eff}} \rightarrow \mathbf{p}$	$\phi_{avg}^{AC} - (k_{\text{eff}} z_i - \omega_{\text{eff}} t_i - \phi_{\text{eff}}) + \pi/2$
$g \rightarrow g$	$\mathbf{p} \rightarrow \mathbf{p}$	$(\phi_{avg}^{AC} - \frac{1}{2}\phi_{\text{diff}}^{AC})$
$e \rightarrow e$	$\mathbf{p} + \hbar\mathbf{k}_{\text{eff}} \rightarrow \mathbf{p} + \hbar\mathbf{k}_{eff}$	$(\phi_{avg}^{AC} + \frac{1}{2}\phi_{\text{diff}}^{AC})$

Table 2.1 Summary of phase shifts caused by Raman transitions. k_{eff}, ω_{eff} and ϕ_{eff} are the effective wavevector, angular frequency and phase offset respectively.

To calculate the state population after the Mach-Zehnder sequence is complete, equation 2.49b can be utilised to calculate the amplitude of the excited state $|e\rangle$ after the first $\pi/2$ pulse

$$c_{e,\mathbf{p}+\hbar\mathbf{k}_{\text{eff}}}(t_1 + \tau/2) = -ie^{-i\delta\tau/4} e^{-i\phi_A(t_1)} \frac{\Omega_{\text{eff}}}{\Omega_R} \sin\left(\frac{\Omega_R t}{2}\right), \tag{2.68}$$

where it has been assumed that the AC Stark effect has been cancelled via careful selection of the relative Raman beam intensities and that initial conditions were $c_{g,\mathbf{p}}(t_1) = 1$ and $c_{e,\mathbf{p}+\hbar\mathbf{k}_{\text{eff}}}(t_1) = 0$. The term $e^{-i\phi_A(t_1)}$ is the optical phase at position A and time t_1.

Inserting the identity $\tau/2 = \pi/2\Omega_R$ to ensure the pulse duration is correct for a $\pi/2$ pulse, and assuming the pulse is short, intense and on-resonance, equation 2.68 reduces to

$$c_{g,\mathbf{p}+\hbar\mathbf{k}_{\text{eff}}}(t_1 + \tau/2) \approx \frac{1}{\sqrt{2}}, \tag{2.69a}$$

$$c_{e,\mathbf{p}+\hbar\mathbf{k}_{\text{eff}}}(t_1 + \tau/2) \approx -\frac{i}{\sqrt{2}} e^{-i\phi_A(t_1)}. \tag{2.69b}$$

for atoms which were initially in the ground state. This equation shows that, given the above assumptions, the amplitude to be in the excited state depends upon the optical phase, with

each interaction accumulating a phase dependent on spacetime position. Again utilising 2.68, the π pulse amplitudes are

$$c_{g,\mathbf{p}+\hbar\mathbf{k}_{\text{eff}}}(t_1+\tau) \approx 1, \tag{2.70a}$$

$$c_{e,\mathbf{p}+\hbar\mathbf{k}_{\text{eff}}}(t_1+\tau) \approx -ie^{-i\phi_A(t_1)}. \tag{2.70b}$$

Multiplying amplitudes in the conventional way and summing over paths results in

$$\begin{aligned} c_{e,\mathbf{p}+\hbar\mathbf{k}_{\text{eff}}}(2T+2\tau) &= c^{I}_{e,\mathbf{p}+\hbar\mathbf{k}_{\text{eff}}}(t_3+\tau/2) + c^{II}_{e,\mathbf{p}+\hbar\mathbf{k}_{\text{eff}}}(t_3+\tau/2) \\ &= -\frac{i}{2}e^{-i\phi_{B'}(t_2)}\left(1-e^{-i[\phi_A(t_1)-\phi_B(t_2)-\phi_{B'}(t_2)+\phi_C(t_3)]}\right) \\ &= -\frac{i}{2}e^{-i\phi_{B'}(t_2)}\left(1-e^{-i\Delta\phi_{total}}\right). \end{aligned} \tag{2.71}$$

2.5.3 Gravimetry

Assuming a uniform gravitational field, the Lagrangian is given by

$$\mathscr{L} = \frac{1}{2}m\dot{z}^2 - mgz \tag{2.72}$$

and $\Delta\phi_{path} = 0$. In the absence of a gravitational field, $\Delta\phi_{light}$ would also be zero, but gravity breaks the symmetry of the states and a phase is accumulated which is proportional to g. To see this, the phase accumulated along each path is calculated and the difference taken as in 2.67. The offset accumulated for path I is

$$\Delta\phi_{PathI} = [|g\rangle \to |g\rangle]_{t=0} + [|g\rangle \to |e\rangle]_{t=T} + [|e\rangle \to |g\rangle]_{t=2T}. \tag{2.73}$$

Utilising table 3.1, this term becomes

$$\begin{aligned}\Delta\phi_{PathI} = [\phi_{avg}^{AC} + (k_{\text{eff}} z_i(T) - \omega_{\text{eff}} T_i - \phi_{\text{eff}}) + \pi/2] + \\ [\phi_{avg}^{AC} - (k_{\text{eff}} z_i(2T) - \omega_{\text{eff}} 2T_i - \phi_{\text{eff}}) + \pi/2] + \\ [\phi_{avg}^{AC} - \frac{1}{2}\phi_{\text{diff}}^{AC}]\end{aligned} \tag{2.74}$$

Similarly for path II, the phase offset is

$$\Delta\phi_{PathII} = [|g\rangle \rightarrow |e\rangle]_{t=0} + [|e\rangle \rightarrow |g\rangle]_{t=T} + [|g\rangle \rightarrow |g\rangle]_{t=2T} \tag{2.75}$$

$$\begin{aligned}\Delta\phi_{PathII} = [\phi_{avg}^{AC} + (k_{\text{eff}} z_i(0) - \phi_{\text{eff}}) + \pi/2] + \\ [\phi_{avg}^{AC} - (k_{\text{eff}} z_i(T) - \omega_{\text{eff}} T_i - \phi_{\text{eff}}) + \pi/2] + \\ [\phi_{avg}^{AC} - \frac{1}{2}\phi_{\text{diff}}^{AC}]\end{aligned} \tag{2.76}$$

Inserting equations 2.74 and 2.76 into 2.67 and utilising the fact that $z(t) = \frac{1}{2}gt^2$ for an atom initially at rest results in the total phase shift

$$\Delta\phi_{total} = k_{\text{eff}} g T^2. \tag{2.77}$$

Inserting this equation into 2.71 and squaring gives the excited state population

$$\begin{aligned}P_{g\rightarrow e} &= \frac{1}{2}\big(1 - \cos(\Delta\phi_{total})\big) \\ &= \frac{1}{2}\big(1 - \cos(k_{\text{eff}} g T^2)\big).\end{aligned} \tag{2.78}$$

The above equation shows that as the wavepackets travel along different spacetime paths, they pick up different phases dependent on local gravity g. Varying an additional phase offset between the beams will cause the state population to oscillate, resulting in interference fringes. In the counter-propagating configuration, Doppler sensitivity will mean that the fringe amplitude will decrease if the beams frequency is not linearly increased, or *chirped*, to match the Doppler shift. By finding the chirp rate which maximises the fringe amplitude, the gravitational field strength can be measured.

Chapter 3

Experimental Overview

A typical atom interferometer consists of three parts. The first is an initial stage where the atoms are cooled and their internal states are prepared. This is followed by a period of coherent state manipulation as the atoms propagate through space, leading to state interference. Finally, a state detection stage is implemented to determine the phase difference accumulated between the paths. This chapter presents how each of these three stages is achieved.

3.1 Vacuum Chamber

A vacuum chamber is required for an atom interferometer to preserve the fidelity of the atomic internal states. Collisions with air molecules or other atoms of thermal rubidium can cause decoherence and prevent observation of quantum effects. Most atom interferometry experiments achieve a pressure of 10^{-10} mbar with a minimum pressure of 10^{-7} mbar required to form a magneto-optical trap [67].

Figure 3.1 shows the vacuum configuration for this experiment. It consists of a spherical octagon chamber and a six-way cross, connected via a 40 cm long interferometry tube. The spherical octagon, in which the atoms are initially trapped and cooled, consists of two 11.43 cm and eight 3.38 cm diameter ConFlat flanges, with a chamber inner diameter of

8.13 cm [68]. Four of the eight smaller ports are used for MOT beams, one for the rubidium source, one for the Raman beam entrance port and one for atom cloud monitoring. The eighth is used to connect the spherical octagon to the interferometry tube. The intention is that the atoms will eventually be dropped down to the lower chamber and state detection performed there, allowing interrogation times of around a quarter of a second. The coils to create the magnetic field are wound around the octagon, to create a magnetic field parallel to the axis of symmetry which runs through the large windows.

Fig. 3.1 Diagram of the current atom interferometry vacuum chamber, showing both the upper chamber for magneto-optical trapping and state preparation and the lower chamber for state detection.

A pressure of 10^{-9} mbar was achieved by first using a roughing pump to go from atmospheric pressure down to 10^{-2} mbar, followed by a turbo pump to reach 10^{-7} mbar. The vacuum

chamber was then baked out and finally an ion pump used to lower the pressure to 10^{-9} mbar. The ion pump and the vacuum chamber are deliberately spatially separated to minimise the effect of the strong magnetic field created by the ion pump on the interferometer.

The rubidium source in this case is an alkali metal dispenser [69]. This consists of a 'boat' of rubidium chromate and a getter material. By passing a current of $3-5$ amps through the boat, thermal rubidium, as well as other contaminant materials, is released. The getter material acts to absorb the contaminants and results in a purer output. This method provides a warm source of natural rubidium, with a 72:28 ratio of ^{85}Rb : ^{87}Rb.

3.2 Laser Control

To achieve magneto-optical trapping and cooling, precise control of laser frequency, power and polarisation is required. The lasers and optics for this experiment are split over two tables connected by fibres: the first on which the lasers are frequency locked and power amplified; the second on which switching, power balancing and magneto-optical trapping occur. This overall design is shown in figure 3.2.

3.2.1 Frequency Locking

To create the laser beams with the required two frequencies for a ^{85}Rb magneto-optical trap, two Littrow-configuration Moglabs external cavity diode lasers (ECDLs) are used (see figure 3.3) [71]. ECDLs are semiconductor diode-based lasers with an external cavity used for frequency selection. In Littrow-configuration, the cavity is formed between the rear facet of the diode and a diffraction grating, with typical length of a few centimetres. The first-order diffraction mode of the grating is aligned to retro-reflect back into the diode and 'seed' light at a frequency which depends on the grating angle (figure 3.4). This causes the naturally broad linewidth of the diode to narrow [72]. The zeroth-order mode is then used as the laser output.

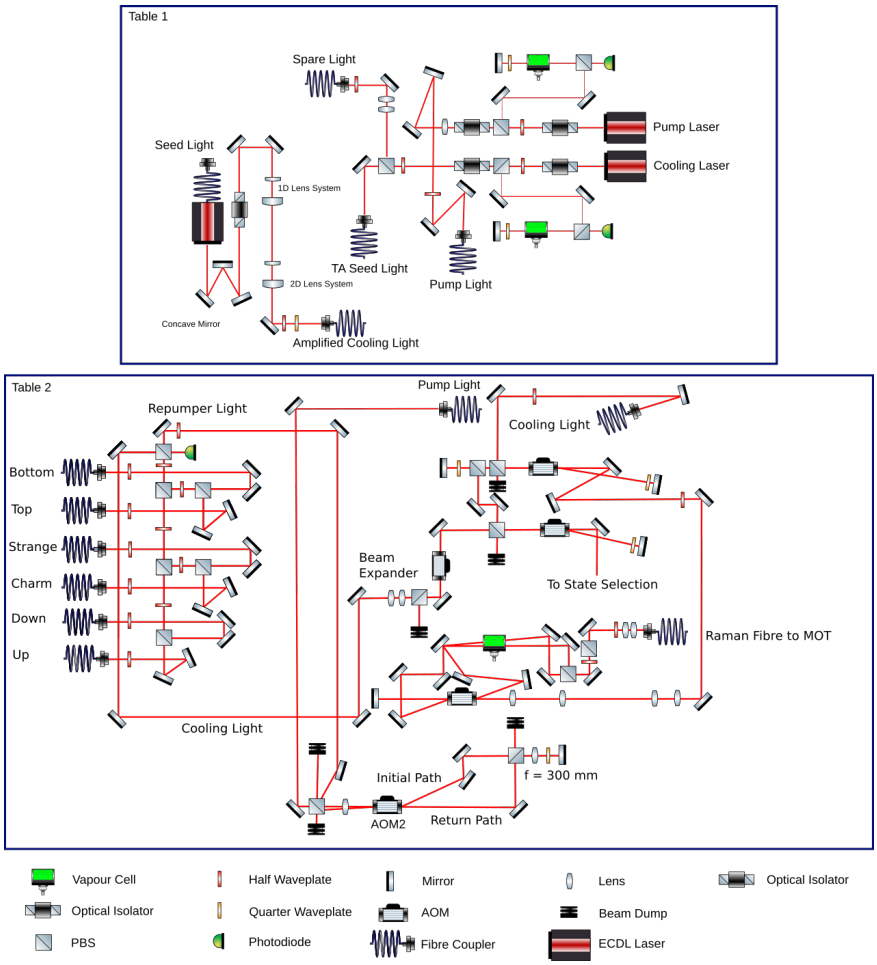

Fig. 3.2 Overview of both independent optical circuit system, the locking circuits and magneto-optical trapping and Raman circuits. This separation is required so that work can be performed on the second optical table without causing the lasers to become unlocked due to vibrations. Optical schematics throughout created via [70].

By varying the angle of the grating ('Littrow angle'), as well as the diode current, the laser output frequency can be tuned [73]. For the ECD004, the Littrow angle is varied via a Piezoelectric actuator. These ECDLs have a full width at half maximum linewidth of around 200 kHz, ideal for locking to a rubidium transition of width $\sim$ 6 MHz.

Diode lasers naturally drift in frequency over time and with variations in temperature, are susceptible to jumping between cavity resonance modes (mode-hopping) etc. Frequency locking requires both the laser frequency to be measured, typically by absorption spectroscopy, and a feed-back loop to adjust the current and grating angle to correct changes in the laser frequency.

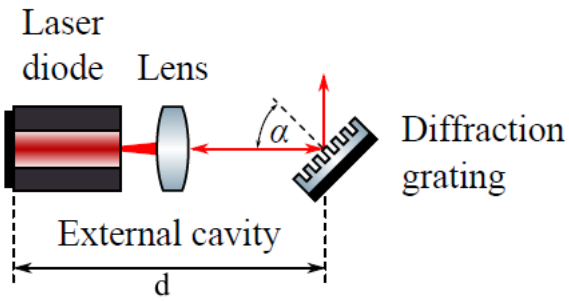

Fig. 3.3 ECDL Littrow configuration: By alignment of diffraction grating, an external cavity can be created and the lasing frequency controlled.

For the ECD004, locking feedback is controlled via a Moglabs diode laser controller [74]. Straightforward absorption spectroscopy involves a laser beam passing through a vapour cell and then being incident on a photodiode. When the laser frequency is on resonance with an atomic transition, the laser light will be scattered and the power that reaches the photodiode will decrease. Measuring the total power that passes through the cell as the laser frequency is varied therefore allows the atomic transition to be characterised.

This method is however limited by the Doppler broadening of the spectral lines. Doppler broadening is caused by the atoms in the room temperature vapour cell having a spread of velocities along the direction of propagation of the laser. This causes non-resonant laser light to be Doppler shifted towards resonance, resulting in a frequency broadening of the measured transition. This broadening completely dominates the natural linewidth of the hyperfine transitions for rubidium, causing the spectral profile to be widened by a factor of 10^3 to ~ 1 GHz, see figure 3.5 [47][75].

Saturated spectroscopy is an improvement on simple absorption spectroscopy, allowing the laser frequency to be locked to the rubidium hyperfine structure and hence providing the MHz frequency precision required for magneto-optical trapping. To perform frequency locking via saturated spectroscopy, a few mW of light is diverted from the ECDL laser via a polarising beam splitter (PBS), as shown in figure 3.6. This light is retro-reflected through a rubidium vapour cell, around which a solenoid is wound. The initial and retro-reflected beams are referred to as the pump and probe beams respectively. The beam profile is enlarged via

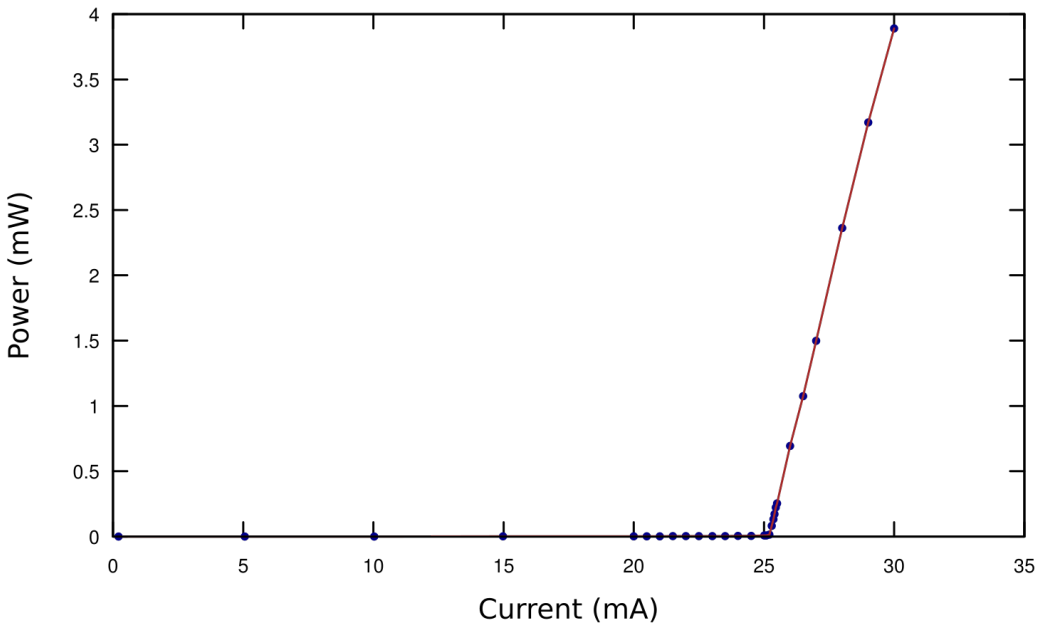

Fig. 3.4 ECDL lasing plot. The ECDL was aligned to be retro-reflective and the output power measured. At the lasing current, the back-reflected light begins to seed the internal laser cavity, causing the 'hockey stick' shape and the drastic increase in power, here at around 25 mA. This effect is useful diagnostically to check external cavity alignment.

a beam expander (not shown) to address as large a number of atoms in the vapour cell as possible.

As the laser frequency is scanned across resonance the beam frequency may be above or below the central resonance frequency. If the frequency is higher than the central frequency, it is effectively blue-detuned from resonance. This means that those atoms which travel away from the pump beam will have a compensating red-detuning, and so will be on resonance and relatively likely to absorb a photon. These atoms are not, however, likely to be scattered via the probe beam, due to being blue-detuned with respect to this beam and hence pushed even further away from resonance. The probe beam will still be scattered by the vapour, but by a different velocity class of atoms than scatters the pump beam. Similarly, when the frequency of the laser light is lower than the resonance frequency, it is effectively red-detuned and the pump beam will more strongly interact with those atoms moving towards this beam. By the same logic, the probe beam will again be pushed away from resonance with respect to the atoms in this velocity class and so little scattering will occur via these atoms.

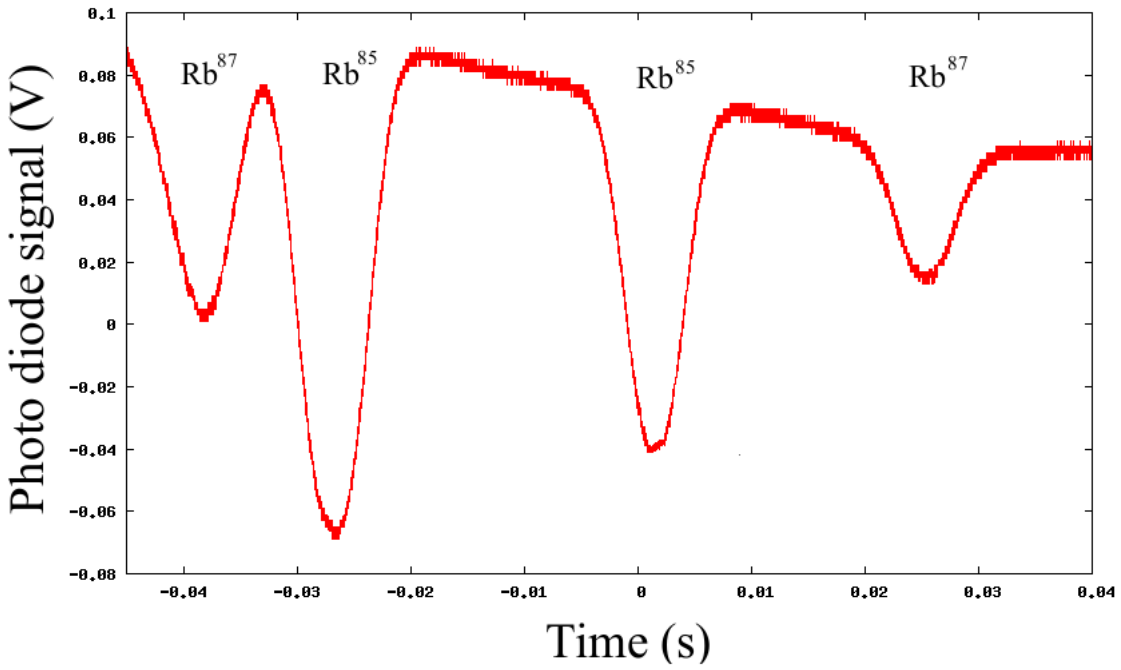

Fig. 3.5 Simple absorption spectroscopy plot for both species of rubidium, as the laser frequency is swept across the resonances. Each of the peaks is Doppler broadened, resulting in a width of the order GHz.

The exception to this is when the laser light is on resonance; in this case, both beams will only interact with those atoms moving perpendicularly to the beam and will both be on resonance with the same velocity class of atoms. Because both beams are now on resonance with the same atoms, the pump beam excites the atoms to saturation leaving a reduced number of atoms in the ground state for the probe beam to excite. The scattering probability for the probe beam will therefore be greatly reduced. This causes an increase in the probe beam output intensity at the central frequency ω_0, resulting in the narrow resonance peaks, known as Lamb dips, observed in figure 3.7.

These reduced width peaks are used to frequency lock the two laser frequencies needed to create a MOT. This is done by converting the peak voltage signals measured by the photodiode into an error signal. The laser diode controller, by dithering the current through the coil surrounding the rubidium cell, shifts the rubidium energy levels via the Zeeman effect. Applying a frequency dither on the laser diode with a phase shift creates an error

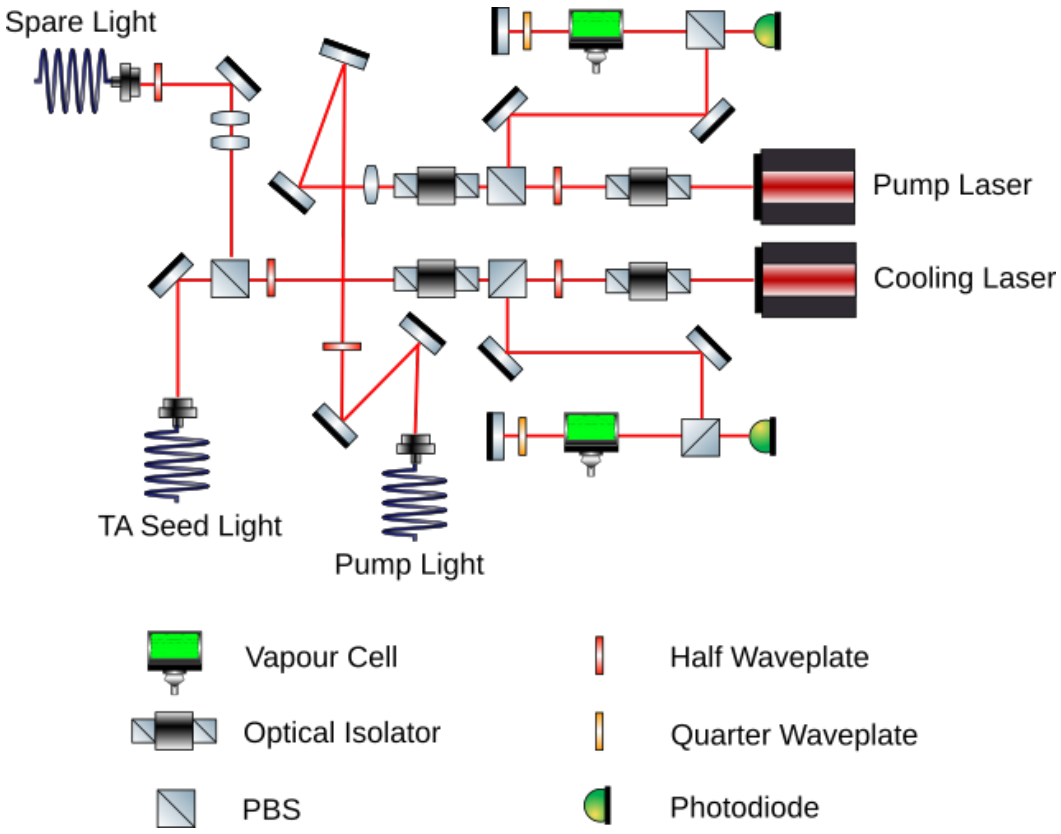

Fig. 3.6 All frequency generation is done via the repumper and cooling ECDLs shown above. The repumper light is coupled to the main table via an optical fibre, with an efficiency of around 50 %. The cooling light is used as seed light for a tapered amplifier. Only around 20 mW is required for this, so the rest of the light is used as spare light for other experiments.

signal which can be adjusted to lock the frequency to the side of the transition. For more information, see [74] [76].

For atoms of ^{85}Rb, one laser, the 'cooling' laser, is locked to the side of the $5^2S_{1/2},\ F = 3 \rightarrow 5^2P_{3/2},\ F' = 4$ transition, which gives a red-detuning of around 10 MHz as required to perform Doppler cooling. The other laser, known as the 'repumper', is locked to the $5^2S_{1/2},\ F = 2 \rightarrow 5^2P_{3/2},\ F' = 3$ transition, depopulating the F = 2 state and preventing the cooling cycle from ending.

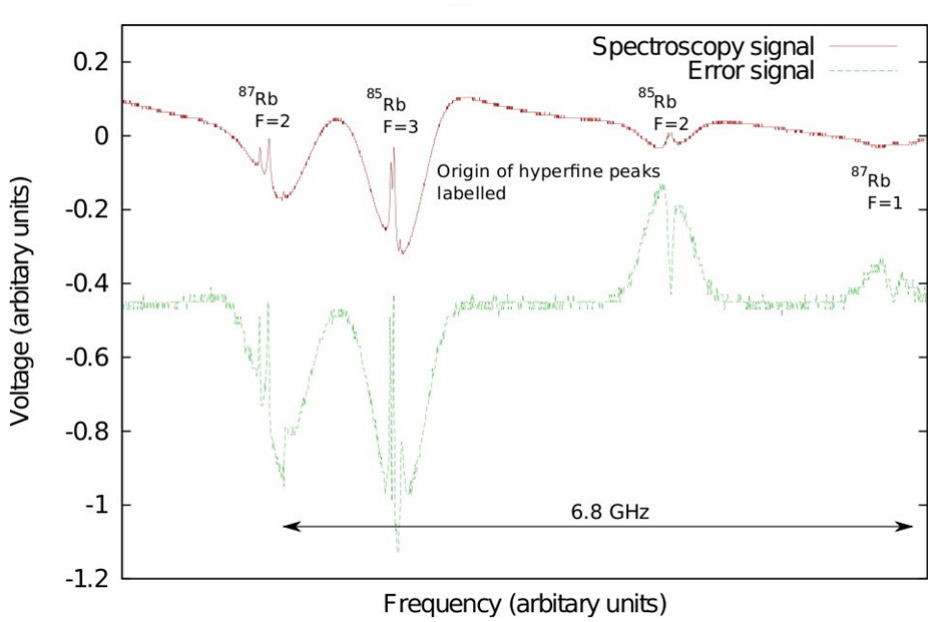

Fig. 3.7 Saturated spectroscopy signal for laser locking. The narrow spikes are the 'Lamb dips' caused by saturation spectroscopy. The green line shows the error signal which is generated from the photodiode signal and is used to provide a locking slope at the peak positions. The cooling laser is locked to one of the F = 3 transitions, the repumper to one of the F = 2 transitions.

3.2.2 Power Amplification

Both the cooling and repumper Moglabs ECDLs produce around 70 mW of laser power. For the cooling beam this is not sufficient power to create a large trapped atom cloud, due to the combined losses from approximately 20 optical components. To compensate for these losses, optical amplification of the cooling beam is required. For this, a Thorlabs tapered amplifier (TA) was used. Around 8 mW of locked cooling light is coupled into a fibre which is then used to 'seed' the TA, giving up to 2 W of output power at the same frequency as the input light.

Unfortunately, due to the structure of the TA, the output mode is both elliptical and divergent, with different divergences in the horizontal and vertical directions. Even with the built-in optics of the TA, this makes the output mode very difficult to efficiently couple into a fibre. Extra optics are therefore required to correct for this astigmatism (see figure 3.8). After

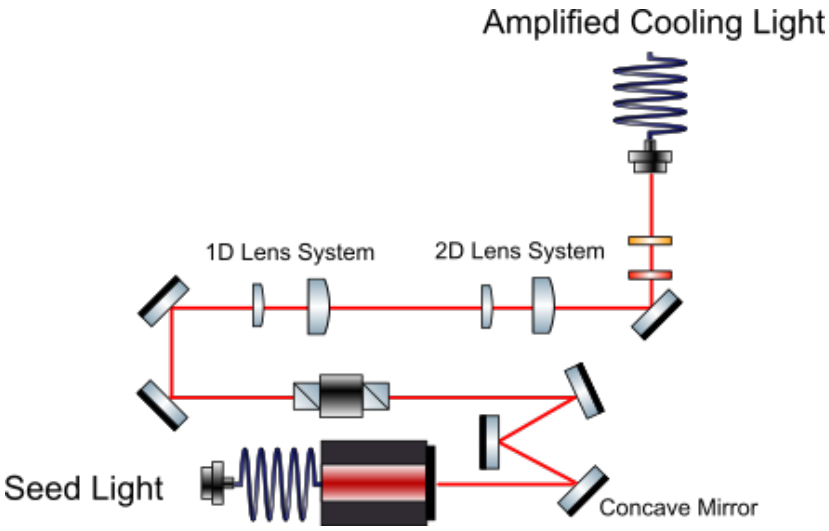

Fig. 3.8 Around 10 mW of locked light from the cooling laser is used to seed the tapered amplifier. The output light is then beam shaped via a concave mirror and a 1D beam expander to correct for ellipticity, followed by a 2D beam expander for collimation and coupling efficiency. Both a half waveplate and a quarter waveplate are used to create linearly polarised light which is aligned to the fast axis of the fibre.

leaving the output facet, the light is incident upon a concave mirror which is angled to stop back-reflections into the TA. The concave mirror collimates the beam in the horizontal direction and reduces the divergence of the beam in the vertical direction. After passing through an optical isolator which blocks back-reflections from the experiment, a pair of 1-D lenses are used to collimate the beam in the vertical direction at the point where the diameter of the beam in the y-direction has expanded to match the diameter in the horizontal direction. This near-circular and collimated beam is then expanded to match the aperture of the fibre collimator by two spherical lenses. The mode shapes before and after this procedure are shown in figure 3.9. This mode correction allowed a maximum coupling efficiency of around 40% to be achieved.

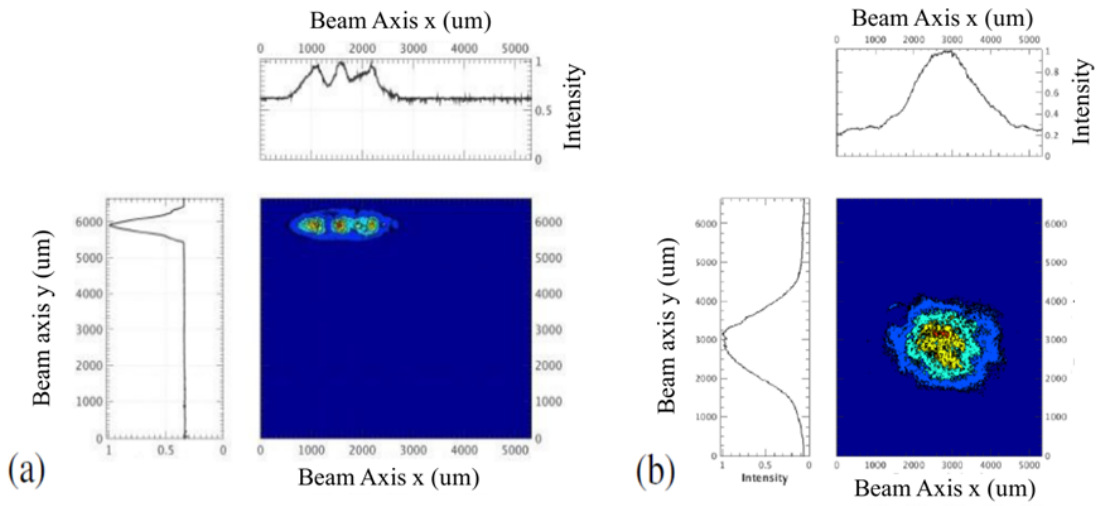

Fig. 3.9 As (a) shows, the output of the tapered amplifier is highly elliptical with several different modes, causing a critical reduction in fibre coupling. (b) was taken after various beam shaping measures were implemented, creating a much more Gaussian beam with a single mode. This allowed a coupling efficiency of around 40%.

3.3 Sequence Timing

This section deals with the intensity control of the cooling and repumper lasers, as well as frequency-shifting of the cooling laser, via acousto-optic modulators (AOMs). This capability is needed both for beam switching and for the polarisation gradient cooling stage.

3.3.1 Cooling Laser Control

The cooling laser is transported to the interferometry table via a polarisation-maintaining (PM) fibre and double passed through a pair of 80 MHz AOMs. AOMs are optical components which use RF frequencies to diffract light as it travels through a crystal. By varying the frequency and power of the RF signal, these AOMs are used to control the frequency and intensity of the cooling beam, as shown in the optical schematic figure 3.10 [77]. The beam first passes through a 500 mm focal length lens to create a beam waist at the centre of AOM0. Before reaching this AOM, it passes through a half waveplate PBS combination set to deflect

all of the power towards the AOM. The diffraction efficiency is then maximised via rotation of the AOM to the Bragg angle [78]. This downshifts the frequency of the beam by -80 MHz with a bandwidth of 20 MHz. A pick-off mirror is placed at the zeroth-order diffraction mode to send light to the Raman system (see section 3.9).

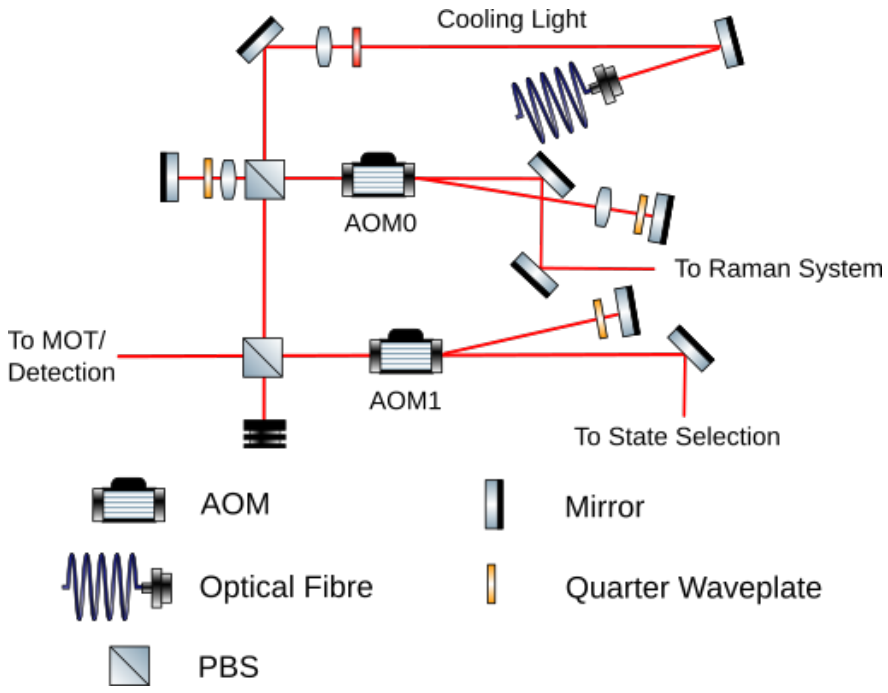

Fig. 3.10 Around 300 mW of cooling light is transported to the main table via fibre. The cooling laser is then double-passed through two AOMs to control both intensity and frequency.

The first-order mode passes through an f $= 300$ mm lens to collimate the light and is then double-passed through a quarter waveplate via a retro-reflection mirror to change the polarisation from vertical to horizontal. The retro-reflection mirror is aligned so that the beam returns along the same path, again forming a beam waist at the centre of the AOM, with the diffraction adding another -80 MHz frequency shift. The horizontally polarised light is then transmitted through PBS0 and recollimated via another 300 mm focal length lens. Another QWP/ PBS combination reorients the polarisation back to vertical, allowing the light to travel from PBS0 to PBS1.

A similar procedure happens at AOM1, with a pick-off mirror this time placed on the zeroth-order mode to send light to the state selection system (currently not in use). The light

that is double passed through AOM1 is this time upshifted by 80 MHz, putting the laser back on resonance before it enters the chamber, provided both AOMs are driven by the same frequency RF. By switching the RF frequencies and intensities sent to the AOMs, the frequency of the cooling beam may be shifted by $\pm$ 80 and the optical intensity can also be controlled. For more discussion of this system and its efficiency, see section 4.3.

3.3.2 Repumper Laser Control

Figure 3.11 shows the control system for the repumper laser. The intensity of the repumper laser needs to be controlled while the frequency is kept constant. In this case, the frequency shift generated by passing through the AOM must be cancelled. This was done by double passing the beam through the AOM so that the beam is first upshifted and then downshifted by the same amount.

A half waveplate (not shown) maximises the power passing through PBS3 and AOM2. A 300 mm lens focuses the beam down to the centre of the AOM, with the first-order diffraction modes being picked off and directed towards PBS4. Ideally, all of the light in the zeroth mode would travel through PBS4 and dissipate on a beam dump (for more on this see section 4.3.3). The first-order mode is transmitted through PBS4, collimated and retro-reflected with perpendicular polarisation, then travels back along the m = 0 path. This causes the AOM to both upshift and downshift the light by 80 MHz during the first and second passes resulting in an on-resonance repumper beam, the intensity of which can be manipulated by changing the driving power of AOM2.

3.3.3 Shutters

Electronic shutters were installed on all three different frequency laser paths. These shutters have a plastic blocking element and consequently were placed at positions of low beam power density (large beam profile) to prevent damage. The various shutter timings are also

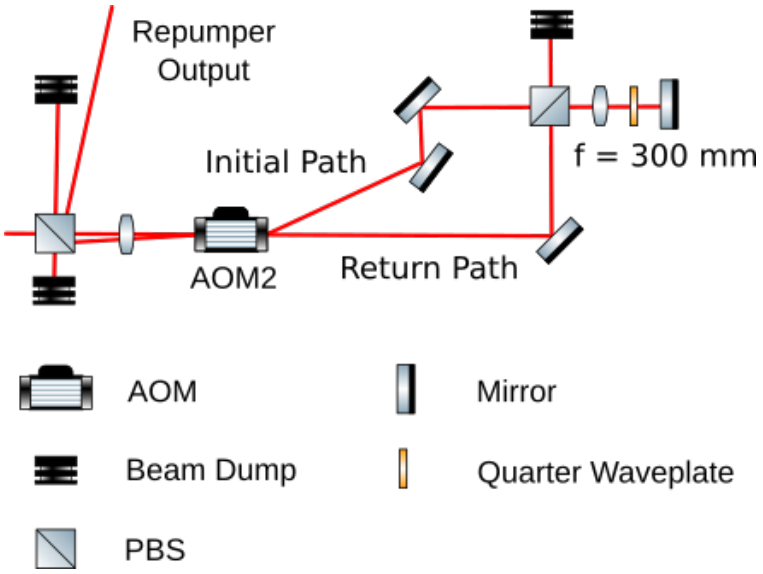

Fig. 3.11 The repumper laser is controlled via AOM2. The above design is chosen to keep the repumper on resonance, acting only as an intensity switch.

controlled by TTL pulses via FPGAs. There is an approximately 2.5 ms delay between the shutter receiving a TTL pulse and the opening/closing action being completed.

To account for this delay, a photodiode was placed at the spare port of the beam overlapping PBS (see figure 3.16) to act as a beam intensity monitoring system. Using this method for diagnostics, the shutter timings can be adjusted to ensure they are not closing too early and disrupting the state preparation stage, nor are they still closed during the state detection phase. The beam monitoring system is also useful for scan diagnostics as any significant drop in either cooling or repumper power, usually due to fibre coupling between the tables drifting, is clearly visible on the oscilloscope trace.

3.4 Magnetic Coils

3.4.1 Bias Magnetic Coils

Due to the Earth's magnetic field and those fields created by various electrical devices in the lab, the magnetic field inside the chamber is inevitably non-zero. These residual fields can have a large effect on the molasses temperature, as well as non-vertical field components changing the Raman transition amplitudes. Cancellation of the ambient magnetic field is achieved by a set of three, large, Helmholtz-configuration coils, placed orthogonally around the experiment. By varying the current in the coils, the magnetic field can be altered and magnetic spectroscopy performed.

3.4.2 MOT Coils

A pair of coils in an anti-Helmholtz configuration is wrapped around the spherical octagon chamber to provide the magnetic field (see figure 3.12). The coils are 8 cm in radius and are separated by 8 cm, providing a magnetic field gradient of 0.74 G/cm·A, with a magnetic field minimum in the geometric centre of the chamber to within 1 mm. They are connected in series to maintain consistency of current between coils, ensuring that the atom cloud position remains stable. The coils are operated in the range of $5 - 12$ A. The resistive heating is compensated by water cooling the coils. The magnetic field gradient was chosen to minimise atom cloud temperature, with an optimal current value of 6.9 A.

3.5 FPGA Control

The AOM driving signals, magnetic coil currents and shutters are controlled by a ZedBoard System on Chip (SoC) which runs a Linux-based operating system [79]. This allows 10 nanosecond timing precision of the sequence. The ZedBoard controls the power supply for

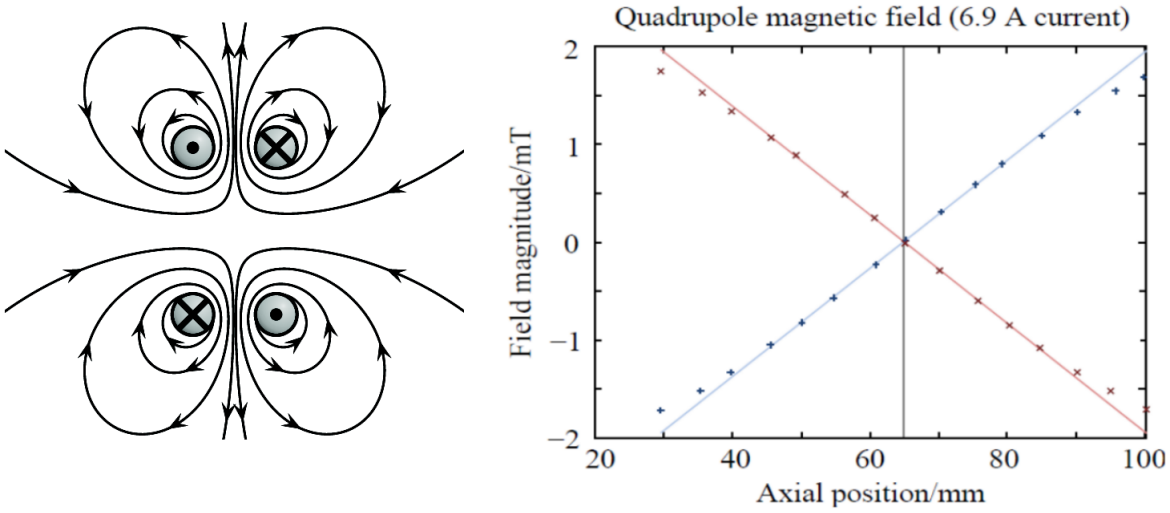

Fig. 3.12 The field lines created by anti-Helmholtz MOT coils are shown on the left, creating an in-going magnetic field along the axial direction between the coils and an out-going field in the plane orthogonal to the axial direction. The plot on the right shows that magnetic field was measured to be linear when moving along the axial direction, with deviations from linearity at distances of around 25 mm from the centre. The red and blue lines indicate measurements for equal but opposite coil currents [75].

the MOT magnetic coils, switching the magnetic field on and off during the interferometry sequence. The shutter sequence timings are also controlled directly from the ZedBoard.

A Novatech 409B digital signal generator is used to produce the oscillating RF signals required to power the AOMs [80]. This generator is controlled via a Xilinx Spartan FPGA which is in turn controlled by the ZedBoard.

3.6 MOT Beam Delivery

3.6.1 MOT Beams

The MOT beam setup evolved over several stages, from a retro-reflective configuration to six independent, free-space beams, and finally to fibre-launched beams. During the second upgrade stage, the beam diameters were increased from 3.4 mm to 12.0 mm, as displayed in figure 3.14. For a cooling power of 6.7 mW, this gives an individual beam intensity of

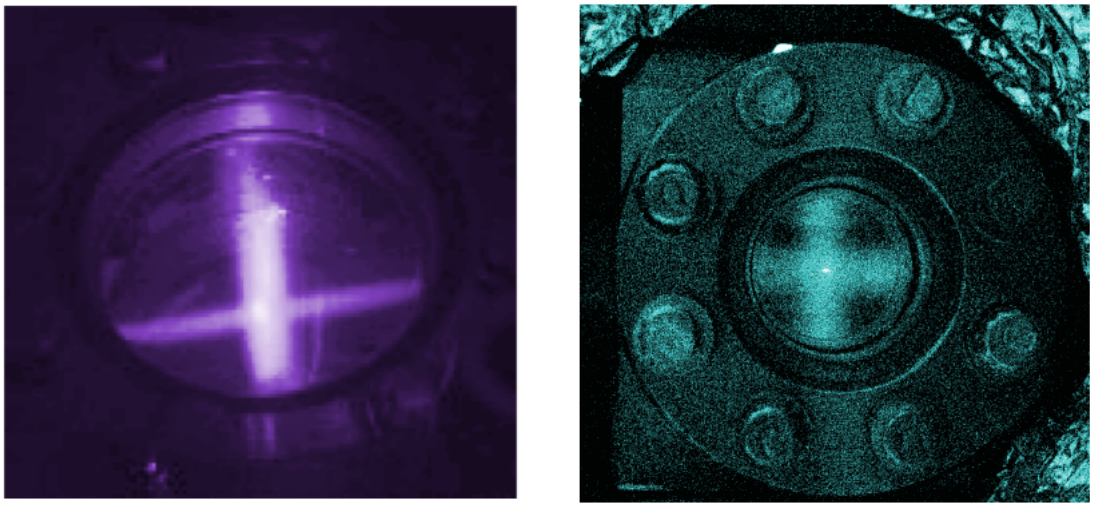

Fig. 3.13 Photographs of atom cloud and MOT beam fluorescence. Filling the upper chamber with rubidium vapour allows the beams to be observed and is useful for beam alignment.

11.85 mW/cm^2. There were several motivations for this important upgrade. Firstly, upgrading from free-space to fibre-launched beams made the process of beam alignment much simpler and power balancing possible due to identical Gaussian profiles of the counter propagating beams. Secondly, the increase in beam diameter allowed the capture of many more atoms in the atom cloud, from around 5×10^6 to 2×10^8. Finally, larger beams are much less sensitive to alignment error.

The six MOT beams are transported to the spherical octagon MOT ports via polarisation-maintaining fibres. The six independent beam outputs need to be flexible to aid alignment and beam overlap, and are designed as follows (see figure 3.15). The PM fibre is attached to a 3 mm output coupler, fixed to a kinematic mount. The beam passes first through a quarter waveplate, mounted in a rotation mount, which converts the linearly polarised light to circular light. The beam then passes through a pair of lenses to expand the beam from 3 mm to 12 mm diameter. This telescope is mounted in a screw-in optics tube for removal during power balancing. The kinematic mount gives an angular range of $\pm 4^\circ$, and the mount is fixed to a pair of orthogonal translation stages. This allows the beams to be both translated in two dimensions and tilted with respect to the chamber.

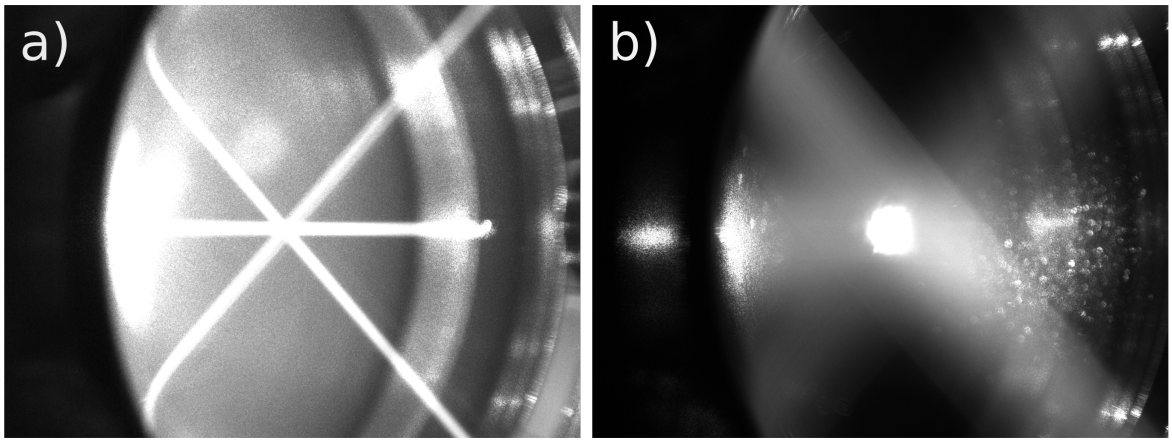

Fig. 3.14 Photograph a) shows the beams and atom cloud before the fibre launch upgrade and b) after the upgrade. The beams are clearly larger and a bigger atom cloud is now visible, especially relative to the larger and therefore more dispersed MOT beams.

To achieve the correct polarisations for the MOT beams, the six independent beam configuration is temporarily reverted to a retro-reflective setup. This is done by installing lens tubes with quarter waveplates and mirrors inside on one of the beams along each axis. This ensures that the input and reflected beams share the same ellipticity, so that once a visible MOT is produced, optimising the brightness of the MOT by rotating each QWP sets the polarisation of the beams to be circular, reducing the number of degrees of freedom from six to three. Once the brightest MOT is achieved, the retro-reflective components are removed and the same procedure is repeated for the other three beams. This way, using retro-reflected beams allows the polarisations of the pairs of beams to be set independently.

3.6.2 Power Balancing

To create a magneto-optical trap, both cooling and repumper frequency light are delivered to the vacuum chamber as orthogonal pairs of beams. The two beams must be overlapped, split into six and power balanced so that the radiation pressure on the atoms from opposing beams is equal, creating a stable atom cloud. To achieve this, a power balancing optical system is required (see figure 3.16). The beams are overlapped on a PBS, half waveplates ensuring maximum transmission. Overlapping in this way causes the cooling and repumper beams to

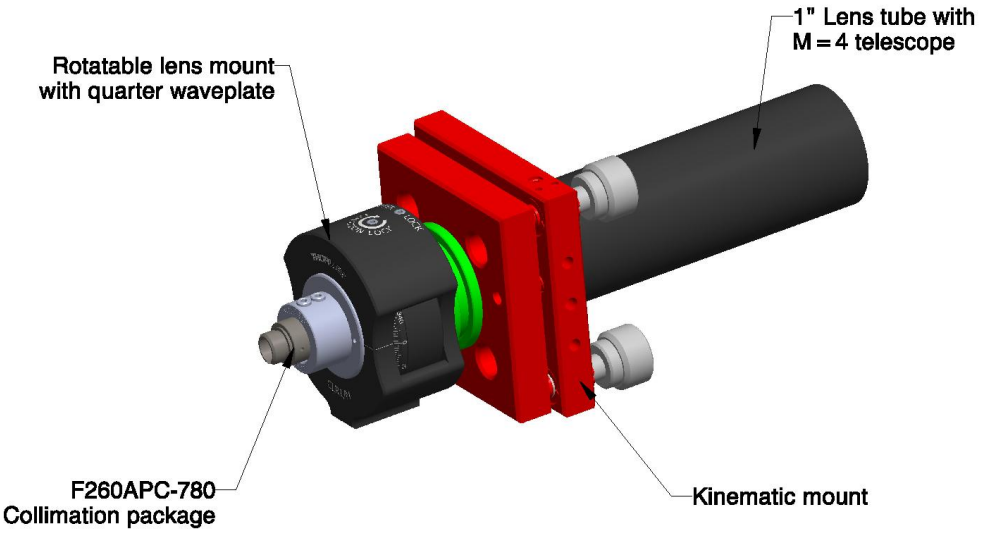

Fig. 3.15 Upgraded MOT beam delivery design. Translation stages to move the beams with respect to the chamber windows are not shown.

have orthogonal linear polarisations. Some power is always 'lost' due to the transmission and reflection inefficiencies of a PBS, so a photodiode for power monitoring is placed here to make use of this. The beams, which are perpendicularly polarised from the PBS onward, are split by a series of half waveplates and PBSs into six arms. These are then coupled into six fibre couplers, with a half waveplate before each to match the polarisations of both cooling and repumper beams to the fast (or slow) axis of the fibre.

By placing cage-mounted power meters in front of the fibre outputs, varying the half waveplate angles can be used to pairwise match the beam powers. For power balancing, only the cooling beam powers are matched. By balancing the powers for each pair and then balancing between pairs, all six cooling beam powers can be made equal. The current setup has a cooling beam power of around 6 mW per beam. Balancing this way, the repumper

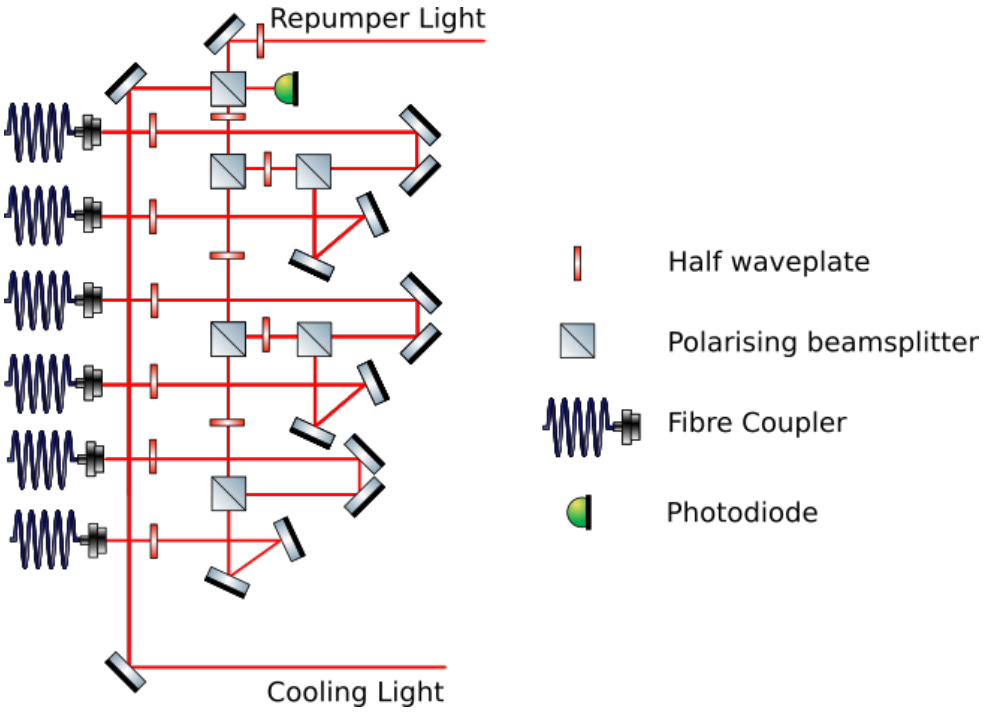

Fig. 3.16 The cooling and repumper beams are overlapped and the half waveplates adjusted to balance the cooling powers. The cooling light is required to travel a long way ($\sim$ 6 m) before entering the final fibre collimator, so is recollimated after it passes through AOM1.

powers of each beam will *not* all be equal, but they will be pairwise equal. This stems from the orthogonality of polarisation between cooling and repumper mentioned earlier. The power ratio between repumper beams is 6 : 2 : 1, with a maximum power of 180 μW per beam.

3.7 MOT and Molasses Diagnostics

By varying the MOT beam alignment, the atom cloud can be made both larger and colder. It is important therefore to be able to measure the beam alignment and variables such as atom number and cloud temperature. This section discusses the methods by which these observables are measured.

3.7.1 Cameras

To perform atom cloud diagnostics, both the MOT and beams may be imaged using cameras, focused at the intersection of the beams where the MOT forms. A pair of Thorlabs DCC1545M CMOS cameras, as well as a single Thorlabs DCU223M CCD camera, are mounted around the upper vacuum chamber to image the MOT beams. They are positioned to cover all three independent planes of the MOT beams, with one camera utilising one of the eight 3.38 cm ports, and the other two viewing via one of the large chamber windows.

3.7.2 Beam Alignment Procedure

To create a stable and spherical atom cloud, the optical and magnetic forces on the cloud need to be balanced. This requires both that the beam powers be balanced and that the beams themselves are correctly aligned, with all three pairs being correctly overlapped and the three propagation axes being orthogonal. By flooding the chamber with rubidium vapour, the beams themselves become visible via the cameras. This is due to the increase in rubidium density in the chamber, causing an increase in the fluorescence scattering.

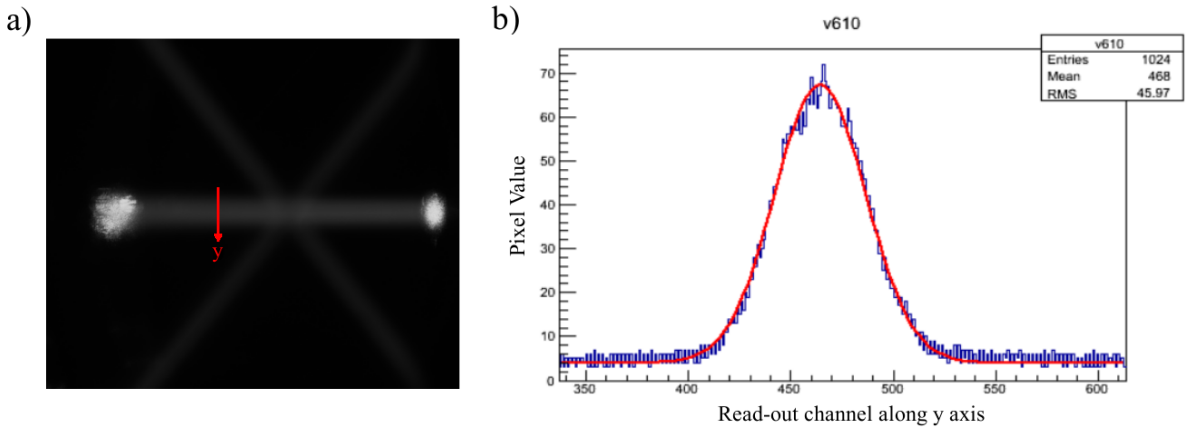

Fig. 3.17 Example photograph a) and Gaussian fit b) to determine the beam alignment.

Coarse alignment is performed by placing laser-cut plastic inserts onto the vacuum chamber ports. These consists of a broadly circular profile with a central hole of ~ 1 mm, much

smaller than the MOT beam diameters. These are designed to fix onto the chamber ports, with two different designs for the two different window sizes. By placing a pair of inserts onto opposing chamber ports, the translation stages and tip-tilt MOT beam mounts (see 3.6.1) can be adjusted to maximise the power passing through the chamber of one of the beams. The power is measured by mounting a power meter at the output insert. Given that the beams are approximately Gaussian, the maximum power should correspond to the beam passing through the geometrical centre of the chamber. Repeating this procedure for all six beams is then a first approximation to alignment.

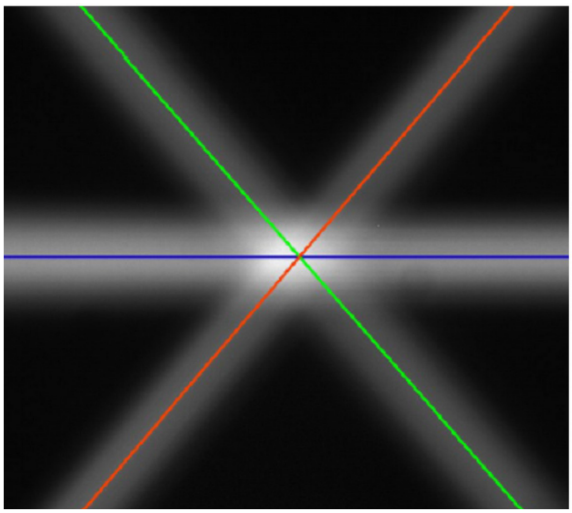

Fig. 3.18 The three lines show how the beam alignment procedure outlined matches with a photograph of the MOT beams. The beam parameters are then adjusted to ensure a common crossing point for all six beams.

To achieve a more accurate alignment method, the camera images can then be analysed and the paths of the beams determined. This is done by fitting the beam profiles with Gaussians and then fitting the Gaussian peaks with straight lines (see figure 3.18). The beam was found to vary in position by less than one pixel, resulting in a beam position precision of $< 10\ \mu$m.

3.7.3 Atom Number Measurement

Once the beam alignment is completed and the MOT beam polarisations are set correctly, further improvements can be made to the MOT via atom number measurements. By varying the magnetic field strengths and tweaking the beam alignment, the number of atoms in the cloud can be increased and thus the signal improved.

Atom number measurements are performed via a camera and lens system imaging the atom cloud. Once the atom cloud is imaged, an iris is used to cut out background light. The camera can then be replaced with a power meter, which measures the radiated power scattered from the atom cloud, allowing for a power calibration of the camera to be performed. The background can be further reduced by subtracting the power measured with the MOT coils off, giving a good indication of the amount of scattered light from the MOT. This power can be related to the number of atoms captured via the equation

$$N = \frac{P}{R_{scatt} E_\gamma} \frac{4\pi D^2}{A}, \tag{3.1}$$

where N is the number of atoms in the cloud, P is the power measured, R_{scatt} is the scattering rate from equation 2.1 and E_γ is the energy of a single scattered photon, equal to 1.589 eV. The ratio $A/4\pi D^2$ is the area of collected light, equal to the active area of the lens closest to the MOT, divided by the total spherical surface area of the light with radius D, equal to the distance from the focusing lens. Using this method the atom number was consistently measured to be $\sim$ 100 million atoms.

3.7.4 Temperature Measurement

The observation of coherent effects requires as little interaction between each atom and its surroundings as possible, which in turn leads to the necessity for very low atomic temperatures. During the MOT stage, the atom cloud is constrained and its shape is dictated

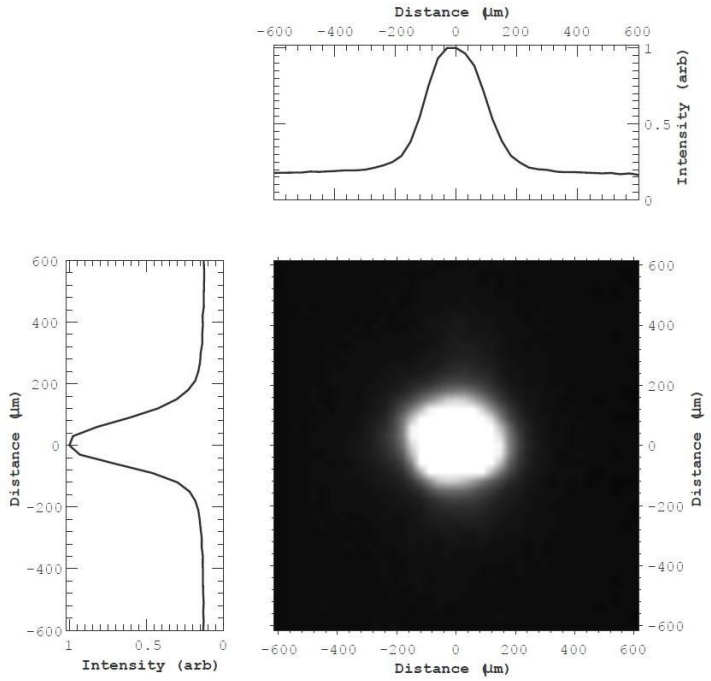

Fig. 3.19 Camera image of an atom cloud. The widths of the Gaussian atom distributions are found by summing over the pixel counts in each row/column and fitting the resultant histogram. From this fit, information about size as a function of time can be inferred.

by beam alignment, power balancing and other factors. When the magnetic field is switched off during the molasses stage, however, the cloud expands uniformly as described by the equation

$$\sigma^2(t) = {\sigma_0}^2 + \frac{k_B T}{m} t^2, \tag{3.2}$$

where σ_0 is the initial cloud radius, T the atom temperature in Kelvin, m the atomic mass of ^{85}Rb and t the time after release in seconds. This equation assumes that the cloud has an initial Gaussian distribution which remains Gaussian throughout. As this equation shows, the atomic cloud expansion rate and temperature are related, so by taking a succession of photographs for different expansion times, the temperature of the atoms after the PGC stage is complete can be inferred. The sum of the pixel counts in each row are plotted for both x- and y-dimensions, see figure 3.19. These are then fitted with Gaussian distributions and an x- and a y-axis width determined. The photographs were taken with a CCD camera which

was calibrated so that the size of the atom cloud could be reliably deduced from the image size.

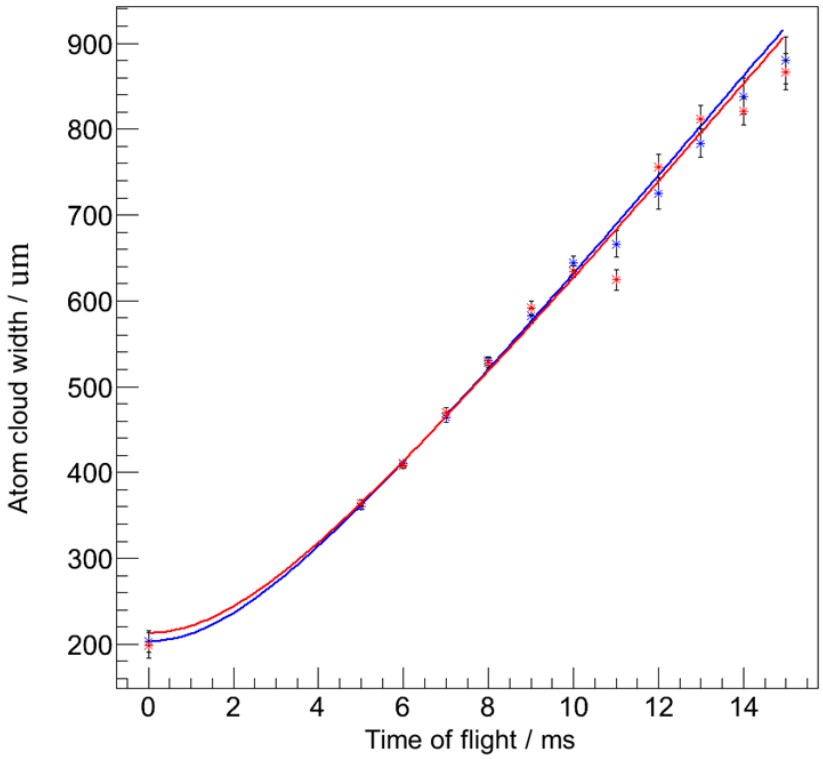

Fig. 3.20 Example of a temperature measurement, with the red and blue lines fitting the x- and y- atom cloud positions respectively.

The procedure to measure the temperature is as follows. The MOT cloud is initially prepared and the magnetic field is then switched off to allow the cloud to expand. After a delay of time t, the cloud is fluoresced by a flash of on-resonant light, imaging the cloud. To reliably and easily perform temperature measurements, a programme was written which would use the videos taken during the expansion process, identify the last MOT frame which is used to measure σ_0 and the 'flash' frame which is used to measure $\sigma(t)$. These two frames are then fitted and the process repeated over a range of delay times. This will of course lead to as many values of σ_0 as time increments, so these are averaged. The averaged initial width and the other widths as functions of time are then plotted in both x- and y-dimensions, and fit via equation 3.2. The output results for a particular measurements are shown in figure 3.20. The average temperature was found to depend on factors including magnetic field strength and

the stepping/ramping procedure during the PGC stage, see figure 3.21. After exploring these variables, the cloud temperature was minimised to 8 μK, and found reliably to be between 8 and 15 μK.

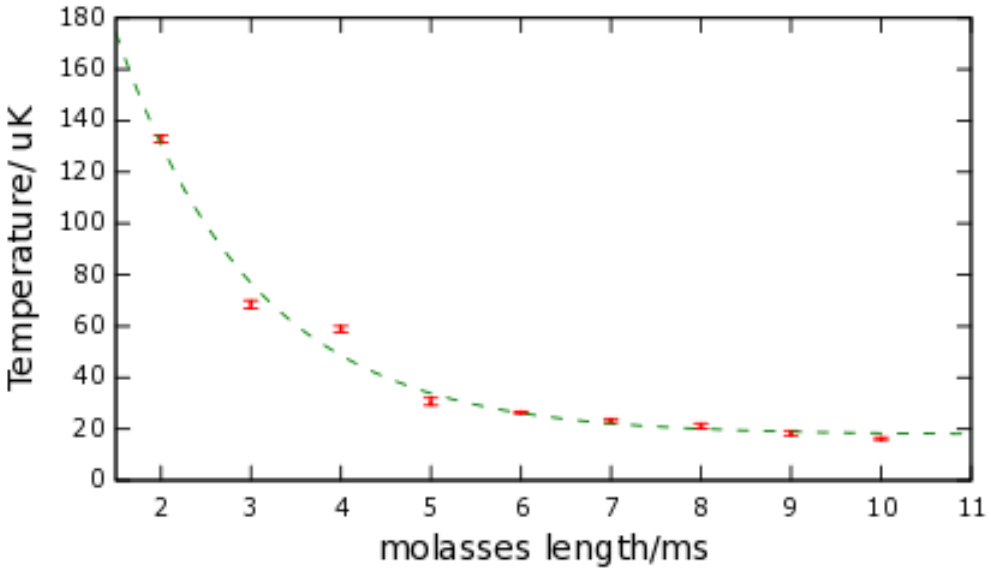

Fig. 3.21 Data showing the reduction of cloud temperature as the molasses duration is increased, where molasses duration here refers to the duration of the PGC cooling effect, where the anti-Helmholtz coils are switched off and the cooling beams are highly detuned.

3.8 Microwave Horn

The main focus of this thesis is the manipulation of atomic states via Raman transitions, but coherent single photon manipulation was also achieved via the application of $\omega \approx 2\pi\times$ 3.04 GHz radiation. The generation of $\omega \approx 2\pi\times$ 3.04 GHz radiation is provided by a microwave horn (Pasternack WR-284 PE9863/SF-10) [81] using the same RF source used for the Raman system [82]. This generator is incapable of producing an RF signal at this frequency, so a frequency doubler (Mini Circuits ZX90-2-19-S+) is used [83]. The signal generator is capable of a maximum output power of around 18 dBm and the frequency

Component	Power Change (dB)	Total Power (dBm)
Rohde & Schwarz SG	-	15
Attenuator	-5	10
Frequency Doubler	-15	-5
Attenuator	-3	-8
ZVE-3W-83+ amplifier	+30	22
Miscellaneous Losses	-7	15
HX2400 Amoplifier	+12	27

Table 3.1 Summary table of RF increases and losses from each component, as well as the total power. Miscellaneous losses most likely come from waveguide connector imperfections and from the presence of a > 2 m long cable to the microwave horn.

doubler is limited to a maximum input power of 23 dBm due to the damage threshold[1]. The generator is therefore first connected to the frequency doubler at a power of 15 dBm. At frequencies of approximately 1.5 GHz, the conversion loss on the doubler was profiled as shown in figure 3.22. Including the loss from the 5 dB attenuator to protect the Rohde & Schwarz generator from back-reflections, this resulted in an output power of -5 dBm. This was then amplified via a Mini Circuits ZVE-3W-83+ amplifier with a gain of 30 dB [84]. As shown in figure 3.23, this resulted in an output power of around 15 dBm. Including the contributions from the attenuator losses, this results in a power loss of around 7 dBm, from various return losses.

An RF power of 15 dBm is equivalent to 31.6 mW. Due to the divergence of the microwaves and distance from the atom cloud (combined with very little evidence of state manipulation) a second amplifier was introduced into the circuit. The Holzworth HX2400 RF amplifier [85] has a gain of approximately 12 dBm, boosting the horn input power from 15 dBm to 27 dBm. This is an order of magnitude increase in power, from 31 mW to 500 mW.

The horn is situated at one of the large spherical octagon windows. Due to the frequency requirements of the waveguide the horn itself is rather large, with a length of 25.4 cm and a wave guide opening size of 11×8.79 cm. This means that the distance between the RF source and the atom cloud can be no less than 28.9 cm. The horn is placed as close to one of the

[1]Decibel-milliwatts or dBm are logarithmic units often used when referring to radio-frequency signal powers. 10 dBm is defined as equal to 10 mW.

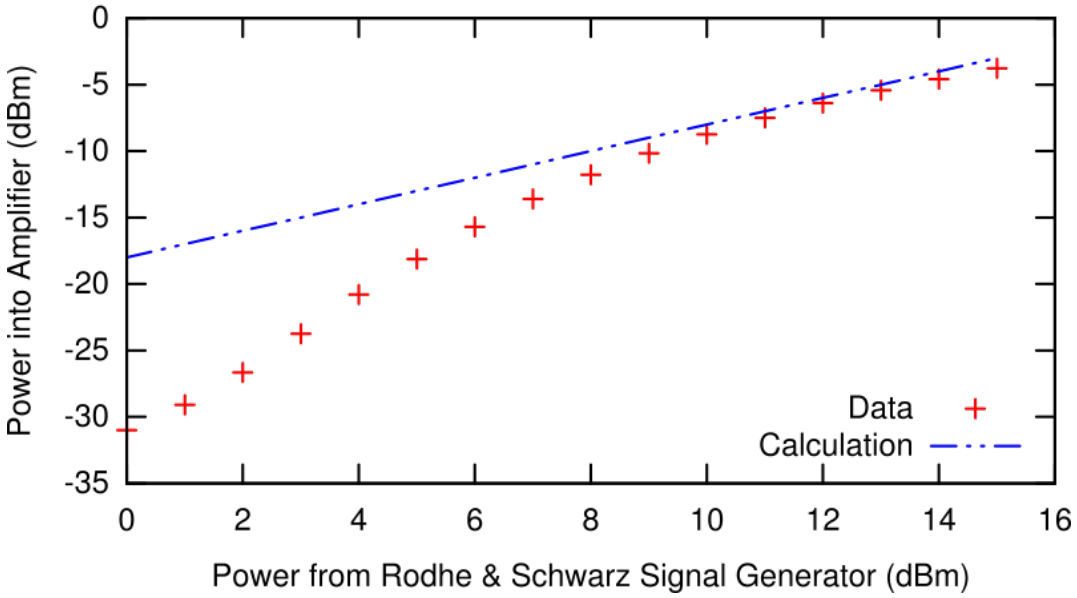

Fig. 3.22 Calibration plot for the microwave horn. The frequency doubler has a cut-off input power of around 10 dBm, below which the power into the amplifier is lower than expected, exhibiting non-linear behaviour. These measurements include a loss contribution from a 5 dB attenuator.

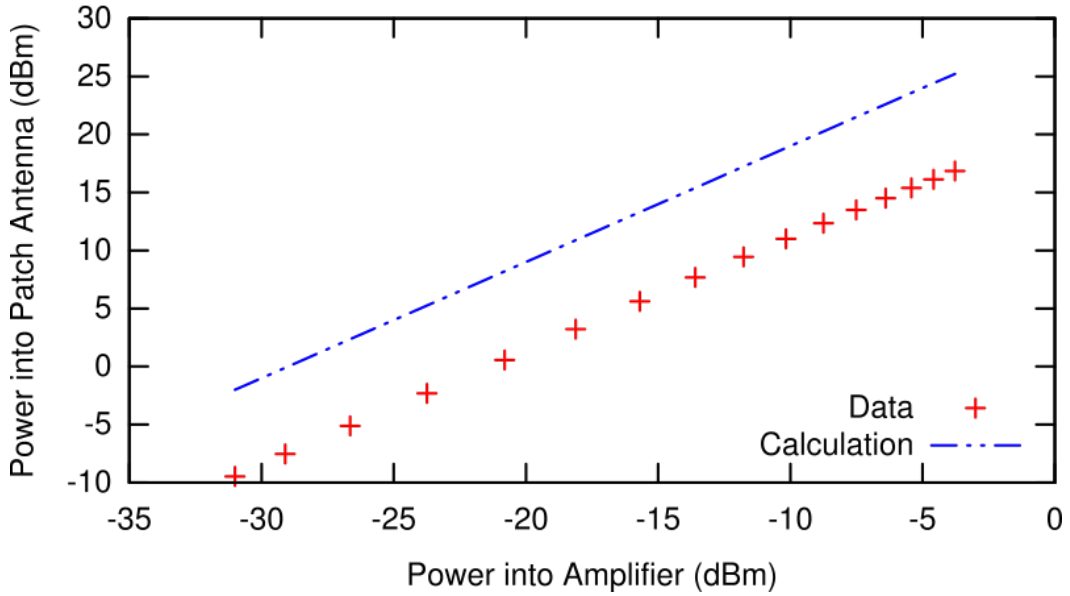

Fig. 3.23 The power going into the microwave horn increases linearly with the power into the amplifier, with an offset of around 7 dBm from what is expected.

large chamber windows as possible, each of which has a diameter of 11.43 cm, comparable to the horn opening size. Combining this with the fact that one of the MOT beams shares

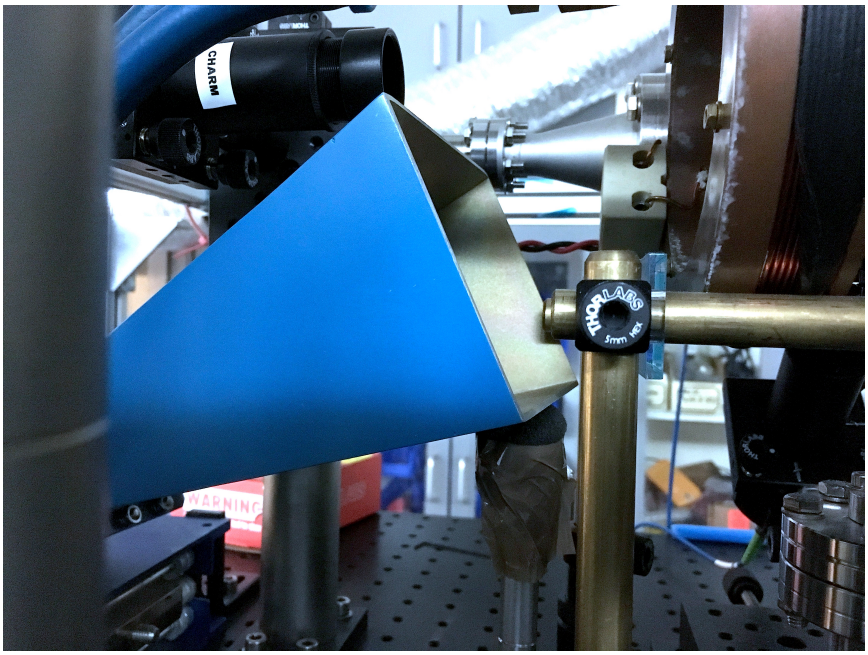

Fig. 3.24 Position of the microwave horn, situated beneath one of the horizontal MOT beams.

this vacuum port, the horn is necessarily situated away from the window and at an angle of around 32.6° (see figure 3.24), further increasing the distance. Any reflections from the window are also increased due to this angle, adding further to sources of lost power.

3.9 Raman System

The cooling beam is split into two frequency components to create the Raman frequencies required [86][87], as shown in figure 3.25. This is performed by a system composed of a 1.5 GHz Brimrose GPF-1500-200-780 AOM [88], with an input RF frequency controlled by a Rohde & Schwarz RF generator [82], see figure 3.27. This RF frequency is amplified from 18 dBm to the required 30 dBm via a Mini-Circuits ZHL-5W-2G+ amplifier [89].

When AOM0 is switched off, the cooling beam passes straight through and is sent to the Raman system. The beam is double passed through the Brimrose AOM and the downshifted and upshifted beams, labelled R1 and R2 respectively, are created by the first-order diffraction modes of the AOM. After AOM0, there is around 200 mW of power travelling towards the

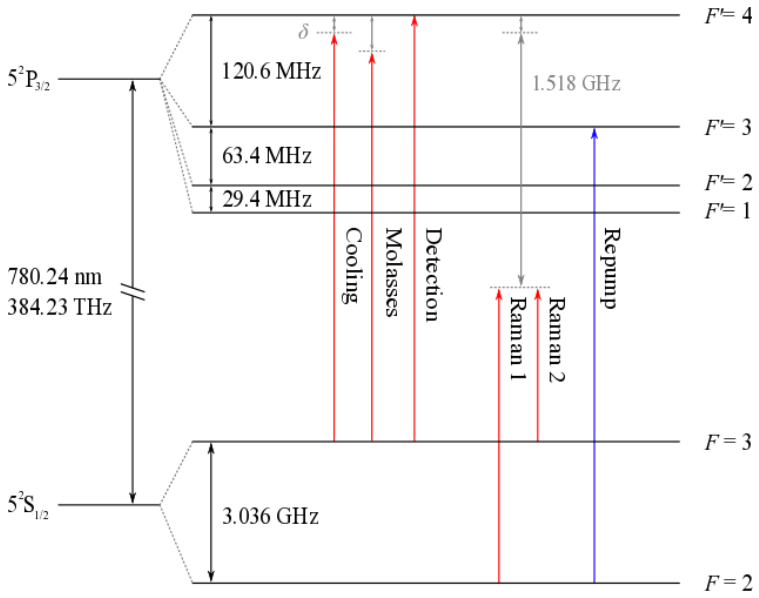

Fig. 3.25 Energy level diagram for rubidium-85. The cooling and repumper frequencies are shown, as well as the on-resonance detection beams, the further detuned molasses frequency and the two Raman frequencies detuned by ≈ 1.5 GHz.

Brimrose. The damage threshold power density of the Brimrose is 100 W/mm^2, with an active area of 0.004 mm^2. This gives a maximum input power in both passes of the AOM of 190 mW. The beam is therefore attenuated with ND filters before passing through an optical system which focuses the beam down to a waist at the centre of the Brimrose.

The optical system on the approach to the Brimrose is used to create a beam waist matching the Brimrose active area which can be translated to the centre of the AOM crystal. The polarisation of the incident light must be set horizontal to maximise diffraction efficiency as, in contrast to the Gooch & Housego AOMs used for the MOT beams, the diffraction efficiency is highly polarisation dependant. This is achieved via a half waveplate placed after the first collimation lens.

As the beam passes through AOM0, it is first collimated by an f = 40 mm lens. A pair of lenses L1 and L2 (with focal lengths denoted FL1 and FL2) are then employed to create a composite lens allowing the creation of an adjustable beam waist which depends on the distance between the lenses. The position of a third lens L3 (with focal length FL3) must be adjusted to collimate this beam, as the position of the beam waist as well as its

size vary with the relative positions of L1 and L2. The collimated beam then travels to a fourth lens (L4) placed at its focal length from the Brimrose AOM. The Brimrose position is fine-tuned via a Thorlabs MBT616D/M three-axis translation stage and a Newport M-UTR80 rotation stage. The beam waist size was iterated to maximise diffraction efficiency, with a maximum efficiency size of 68.5 μm, just below the active aperture size of 75 μm (see figure 3.26). The focal lengths used for this optical system were FL1 = 100 mm and FL2 = FL3 = FL4 = 50 mm.

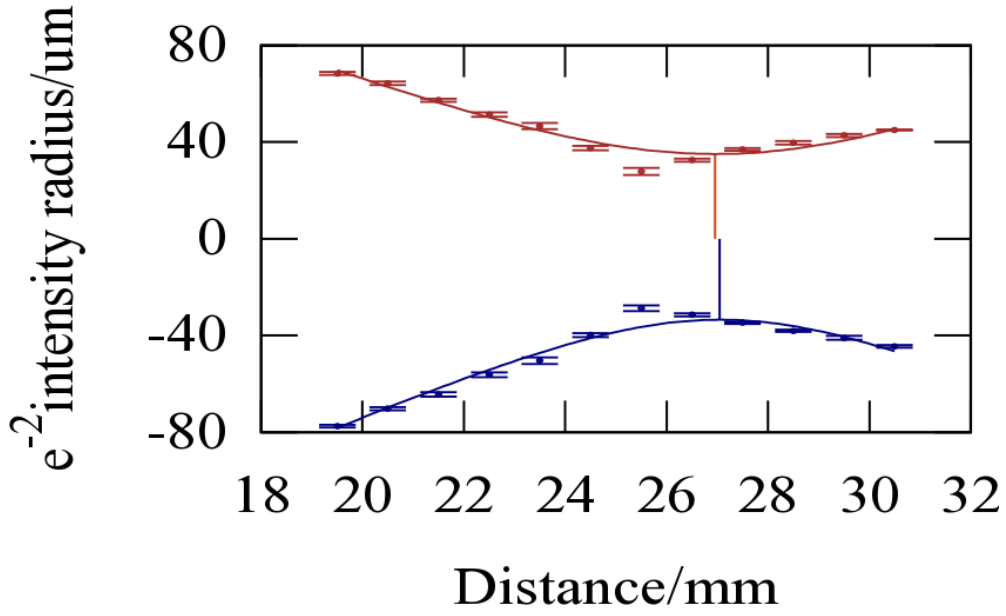

Fig. 3.26 Calibration of the cooling laser beam waist as it passes through the Brimrose. A camera was placed on a translation stage to take photos of the beam waist as it is moved along the direction of propagation. Doing this ensured that the beam waist is less than the active area of the AOM crystal.

The Brimrose AOM is aligned to maximise the diffraction efficiency in both first and second passes. The first pass alignment is performed by a pair of steering mirrors, which act to to set the height and the angle of the beam, as well as a three-axis translation stage for the Brimrose. Together these ensure that the beam passes horizontally through the active area of the crystal. The second pass alignment utilises a Thorlabs CM254-100-E03 concave mirror, mounted in a 5-axis motion control mount and fixed to a 2D translation stage. This mirror has a radius of curvature of 10 cm and is therefore placed at this distance from the crystal output facet

to create the second diffraction pass. Owing to its high operating frequency, the Brimrose has a low diffraction efficiency compared to the Gooch & Housego AOMs, with a first pass maximum diffraction efficiency of around 30%. Another 10% is lost due to reflection from the coating of the crystal.

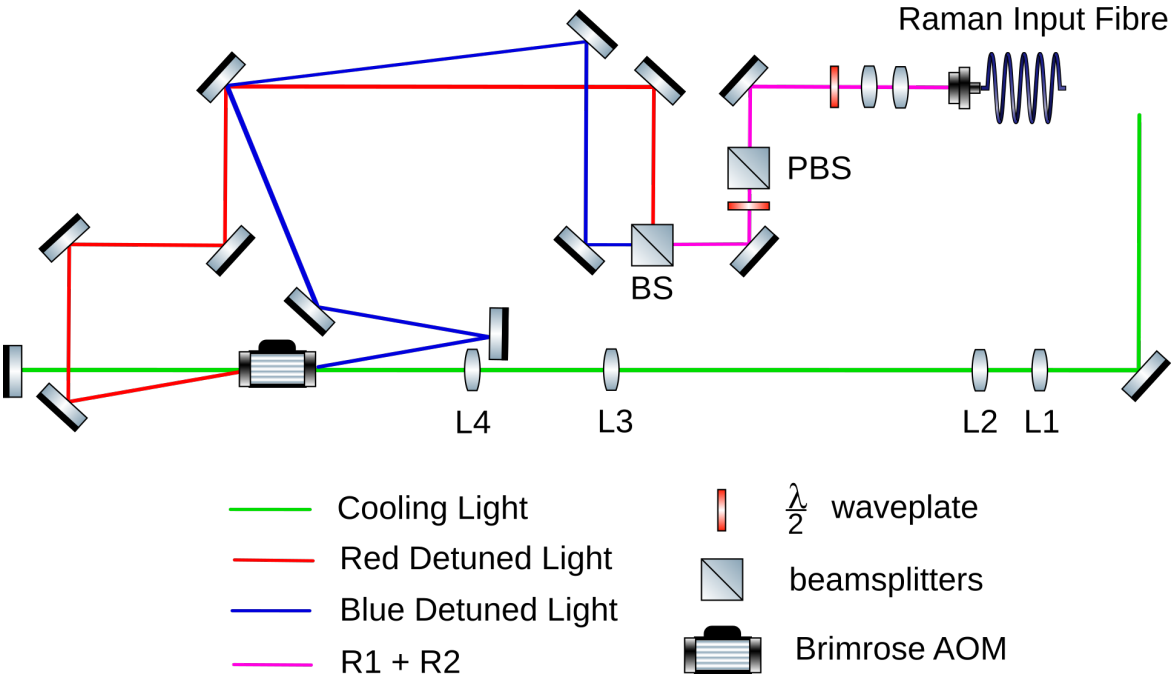

Fig. 3.27 Schematic of the cooling laser being split into the two Raman beam components (R1 and R2). The beams are overlapped via a beam splitter and coupled into a 10 m fibre. To match the Raman polarisations to the key of the fibre, the overlapping beam splitter is necessarily non-polarising. The PBS acts as a polarisation purifying element. The four composite lens elements are labelled from L1 to L4 moving downstream along the beam path.

These phase-locked beams, separated by the approximately 3.04 GHz hyperfine frequency difference, can therefore perform the Raman transitions required to coherently manipulate the atomic states. The beams are passed through a heated rubidium cell to remove on-resonant cooling light reflecting off the input facet of the AOM, overlapped on a 50 : 50 beam splitter and coupled into a 10 m polarisation-maintaining fibre. Coupling to a fibre is used for spatial mode filtering, with a 10 m long fibre chosen to diminish the amount of light which is carried into the chamber via the cladding modes. The Raman beams are injected into the top window of the vacuum chamber via a 13 mm Schäfter + Kirchhoff collimator [90]. This collimator is

fixed into a kinematic mount which is itself attached to a vertical breadboard. The beam then passes through a quarter waveplate to create the σ^+ - σ^+ or σ^- - σ^- polarisations required for velocity-insensitive, co-propagating Raman transitions.

Using a Brimrose AOM to create the Raman beams allows the Raman system to be made using a single input laser. The need for any active phase-locking between beams is also removed by this method. The current Raman system has a two-photon detuning $\Delta = 1.5$ GHz, given by equation 2.35. The ratio of the linewidth (see Appendix A) to the detuning is 4.04×10^{-3}, thus satisfying equation 2.36.

3.9.1 Raman Power Upgrade

The Raman beam coupling was upgraded to increase the power in the Raman beams with the intention of increasing the Rabi oscillation frequency. This would therefore permit state oscillations to be observed before sources of non-Raman contaminant light destroyed coherence. The previous setup achieved a maximum total output Raman power of around 2.5 mW out of a possible 13 mW. To improve on this, both beam profiles were measured using a Thorlabs beam profiler as they entered the collimation package, see figure 3.28 [91]. The downshifted beam R1 was measured to have a Gaussian horizontal diameter of 1.962 mm and a vertical diameter of 1.423 mm. This gives a reasonably large mode ellipticity of 0.68. The upshifted beam R2 was measured to have a horizontal diameter of 2.992 mm and vertical diameter of 2.263 mm, with a similar ellipticity of 0.65 in the horizontal plane.

The collimation package was therefore changed from an F280APC-780 to an F240APC-780 with a $1/e^2$ beam diameter of 1.5 mm at one focal length. The total Raman beam powers were consequently increased from around 2.5 mW to 6.7 mW of total Raman power, with maximum R1 and R2 powers of 5 and 1.7 mW respectively.

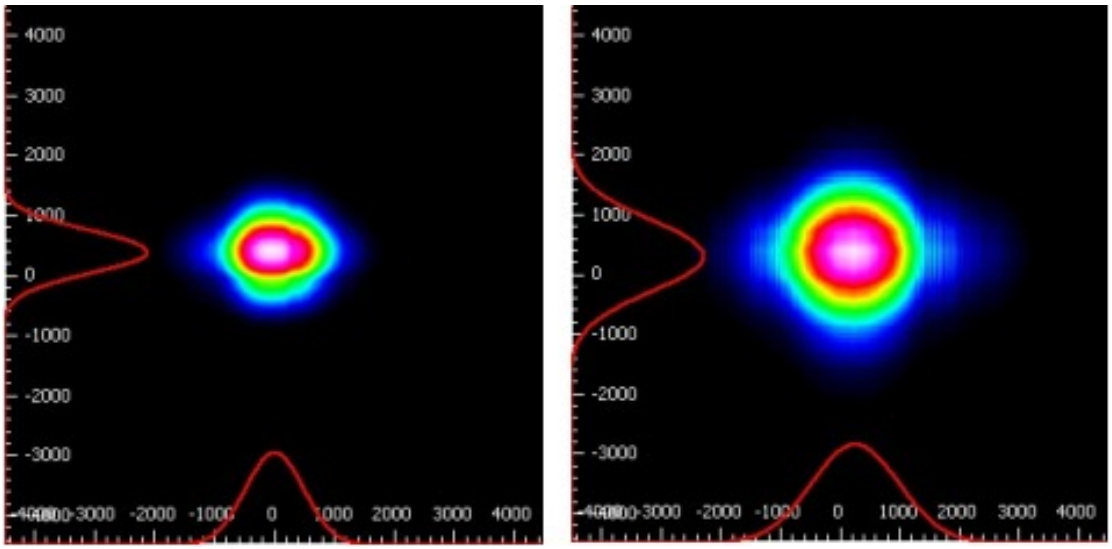

Fig. 3.28 Profiles of Raman beams R1 (left) and R2 (right) entering the Raman fibre collimation package. Profile was measured via the Thorlabs BP208-IR/M scanning slit optical beam profiler.

3.9.2 Raman Beam Alignment

The Schäfter + Kirchhoff collimator is aligned using two orthogonal translation stages in combination with a tip-tilt mount. The beam is aligned to pass straight through the upper and lower MOT ports, passing through the centre of the chamber where the magnetic field is minimised. Alignment is initially performed via a camera placed at the bottom of the lower vacuum chamber, with more precise alignment utilising a pair of custom made port covers with 1 mm diameter apertures at their centre. Due to the fact that the beam is Gaussian, the tip-tilt and translation mounts can be varied to maximise the power through the apertures and hence ensure good alignment. For further details see [50].

3.9.3 Raman Beam Coherence

For the Raman beams to coherently manipulate the internal atomic states, the two Raman beam arms R1 and R2 must be in-phase. The current Raman system generates the shifted frequencies by the splitting of an incoming laser beam via the Brimrose AOM, with no

phase-locking required. This means that both arms should be initially in-phase and any phase difference when the beams reach the chamber is caused by phase noise accumulated between the separate paths. This phase noise is caused by thermal and mechanical vibrations of the optics.

To test coherence, a beat note measurement was performed. The Raman beams were coupled into the same, single-mode fibre to ensure they both had the same beam profile and polarisation, and could be conveniently manipulated. The outgoing beam was then focused down to a waist, at which point a 12.5 GHz bandwidth, Newport 818-BB-45 fast photodiode sensor was placed [92]. The beam was focused to a 52 μm waist, just smaller than the 60 μm photodiode sensor. The photodiode was set up on a pair of orthogonal translation stages to allow the beam waist and sensor to be accurately overlapped. The beam was aligned to be incident on the sensor via a kinematic collimation package mount and a pair of steering lenses. The two different frequencies in the beam cause the measured intensity to sinusoidally vary or 'beat', as shown in figure 3.29. This beat note is measured by a Picoscope 9201 fast spectral analyser [93], with a timing reference provided by the Rohde & Schwarz RF generator [82], showing that the Raman beams are indeed phase-locked.

3.10 State Detection

3.10.1 Fluorescence Measurement Apparatus

During the commissioning stage, state detection is performed in the same chamber as the formation and cooling of the atom cloud. The atoms are fluoresced by the MOT beams to determine the state population. This fluorescence is measured by the state detection system, shown in figure 3.30. It consists of a photodiode (APD430A), fixed to a kinematic mount via an iris. This allows the reduction of scattered light from the chamber windows and other sources of stray light. A 780 nm filter is attached to a Thorlabs SM1L10 lens tube, which screws in to the mount, reducing any sources of background light hitting the photodiode.

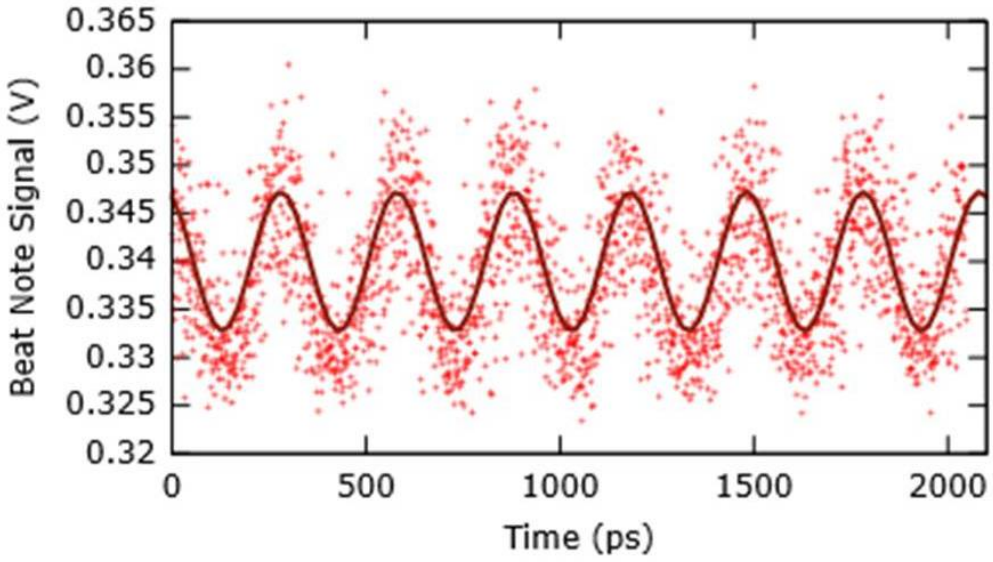

Fig. 3.29 The sinusoidal fit shows how the photodiode signal varies with time as the two Raman beams exhibit a 'beat note' effect. This behaviour is only possible if the two beams have a constant phase difference, showing that they are in phase with one another. The absolute vertical offset is a function of the difference in powers between R1 and R2.

A lens system is then attached via 30 cm cage plates to enable imaging of the atom cloud. The setup is designed so that the photodiode can be replaced with a camera, for diagnostic purposes, with no disruption or need for realignment.

The state detection system was redesigned to make it more stable, flexible and to improve imaging efficiency. The photodiode and lens system was previously suspended adjacent to the chamber viewing window via 12.7 mm posts and right-angle clamps. This was unstable and meant the whole system needed regular realignment. This setup was upgraded to one with the photodiode fixed to an adjustable height mounting post bracket with an associated 3.8 cm diameter mounting post. For this new design, the photodiode once secured needed essentially no realignment.

The new system also vastly improves the image quality, as seen in figure 3.31. The previous system created blurred images with glare caused by laser light reflecting from the chamber windows. The atom cloud is now much clearer and free of glare.

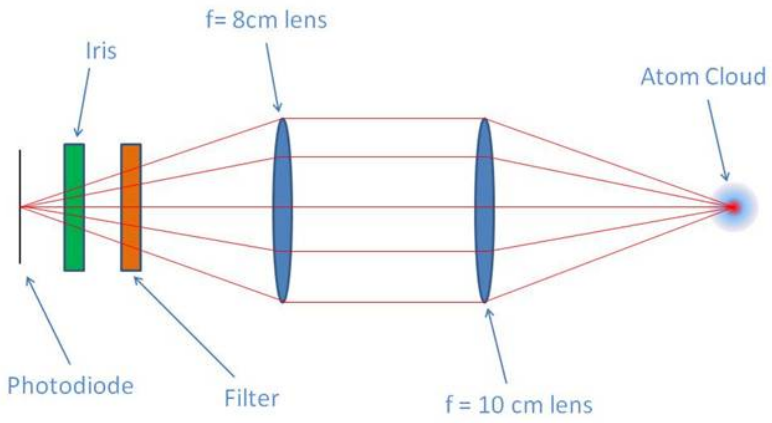

Fig. 3.30 State detection setup. The photodiode and filter act to stop unwanted light reaching the photodiode and causing an offset on the signal. The lens positions were then calibrated to image the atom cloud onto the photodiode. The distance between the photodiode and the atom cloud is $\approx$ 10 cm.

3.11 Interferometry Sequence

The magnetic field and laser beam timings for a single-pulse Raman sequence is shown in figure 3.32. The procedure begins by loading up the atom cloud, requiring the cooling and repumper beams to be on, as well as the magnetic field. The cooling beam is approximately 10 MHz detuned from resonance. After a loading time of around 10 s, the magnetic coils are switched off. A gap of 5 ms is then inserted to allow any eddy currents to die down. The frequency of the cooling laser is then stepped from 10 MHz to 30 MHz. After 2 ms, the cooling intensity is ramped down for a further 2 ms. During this ramp down, the repumper is switched off, causing the F = 3 population to be totally depleted and therefore preparing all of the atoms to be initially in the F = 2 state. To manipulate the state populations, the Raman beams are then switched on for around 75 μs.

After a period of time for interferometry to be performed, the atoms are fluoresced for 2 ms by an on-resonant cooling pulse, the brightness of which is proportional to the F = 3 population which decays exponentially due to atoms being pumped to the F = 2 dark state. There is then a gap of 3 ms to allow the shutter on the repumper to open. A repumper pulse of 2 ms completely repopulates the F = 3 state, and then a second 2 ms cooling pulse fluoresces the

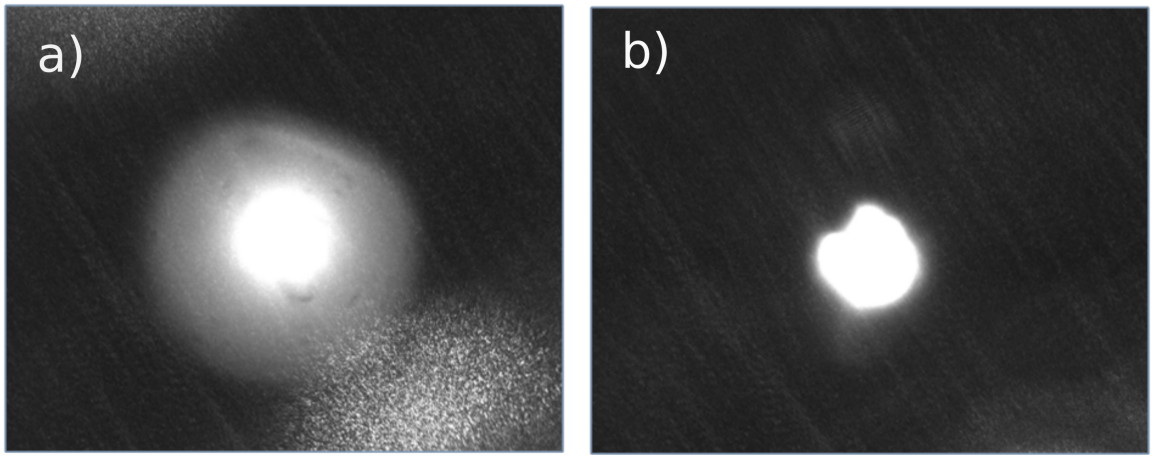

Fig. 3.31 Photograph a) shows the atom cloud before the state detection system was updated, showing evidence of glare and also a blurry image of the cloud. The iris and filter were uses to remove the glare and the imaging was improved by changing the lens setup, as demonstrated in b).

atoms, the intensity of which is proportional to the total number of atoms, see figure 3.33. By integrating the area beneath each exponentially decaying signal, removing the common background light contribution and taking the ratio of the two signals, a normalised F = 3 state population is found. This is the metric which is used to indicate the influence of the Raman beams on the atomic states.

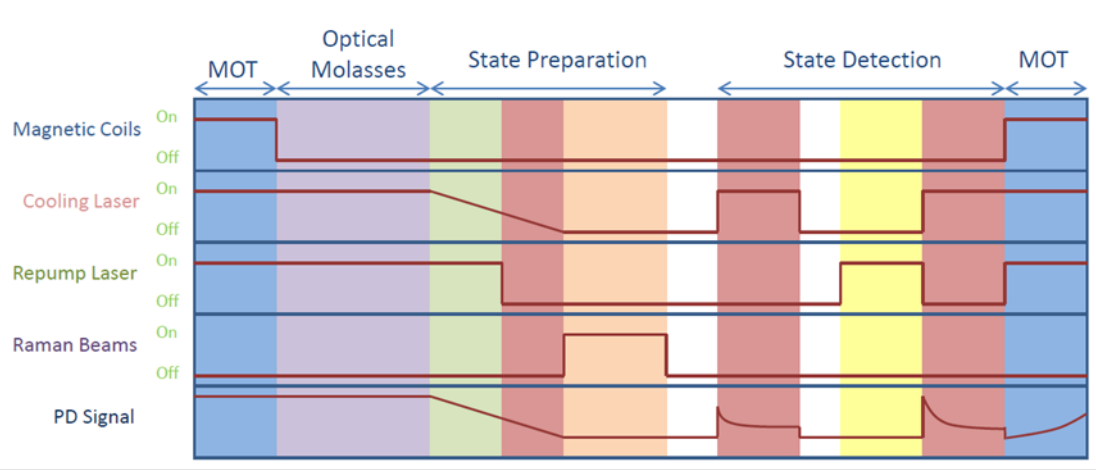

Fig. 3.32 Schematic of interferometry sequence, with the interferometry sequence timing on the x-axis. The photodiode signal shows the exponential decay of the F = 3 state during the cooling pulses.

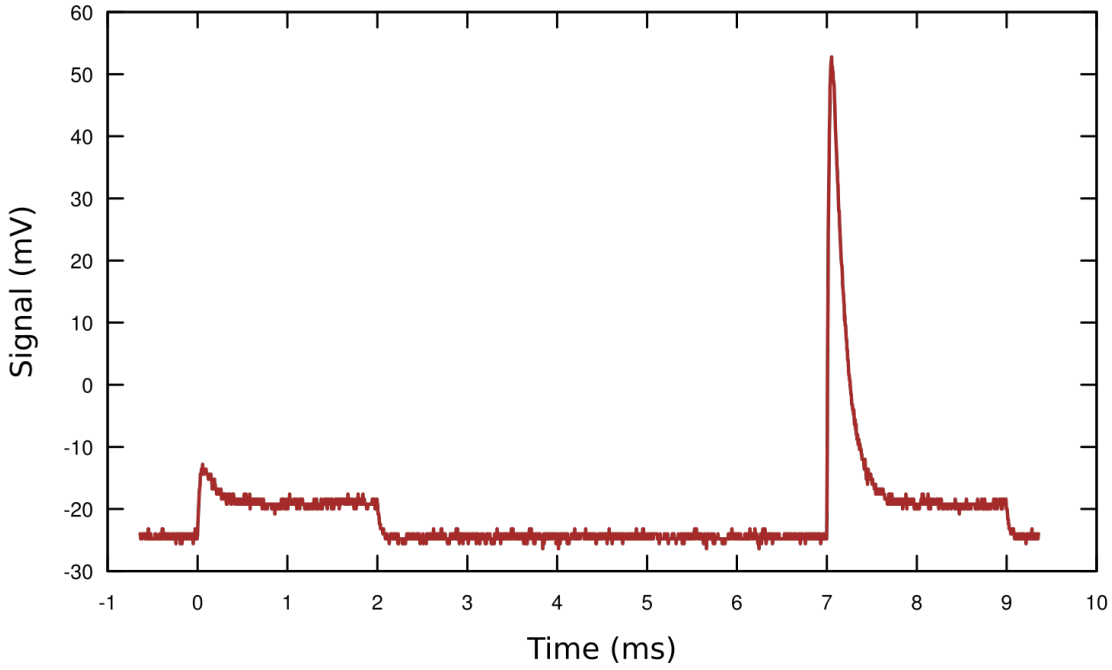

Fig. 3.33 Example of photodiode signal, showing the cooling pulse fluorescences. The ratio of the signal amplitudes is used to infer the excited hyperfine state population after the state manipulation stage.

Chapter 4

Search for Coherent State Manipulation

4.1 First Observation of Raman Resonance

In December 2015, the first evidence of Raman beams state manipulation was found (figure 4.1). The atoms were initially prepared in the F = 2 state and transferred into the F = 3 state via Raman beams. Figure 4.1 shows the population of the F = 2 state as a function of the RF frequency, or equivalently as half the Raman beam frequency difference. The Raman powers in beams R1 and R2 for this measurement were 3.5 mW and 1.5 mW respectively, with a detuning Δ of 1.5 GHz. This would give a predicted π pulse duration of 25 μs. The Raman pulse length was of order 5 ms which would suggest that the final state population passed through many Rabi cycles, causing decoherence effects in the process and reducing the state population to half the maximum value. The contrast of this peak is around 0.15 (see [76] for more details).

This work appeared to be in agreement with what was expected. Achieving data this clear, however, took days to scan and the averaging of many data sets. It was therefore near impossible to use this system to perform Rabi oscillations and measure the magnetic field via

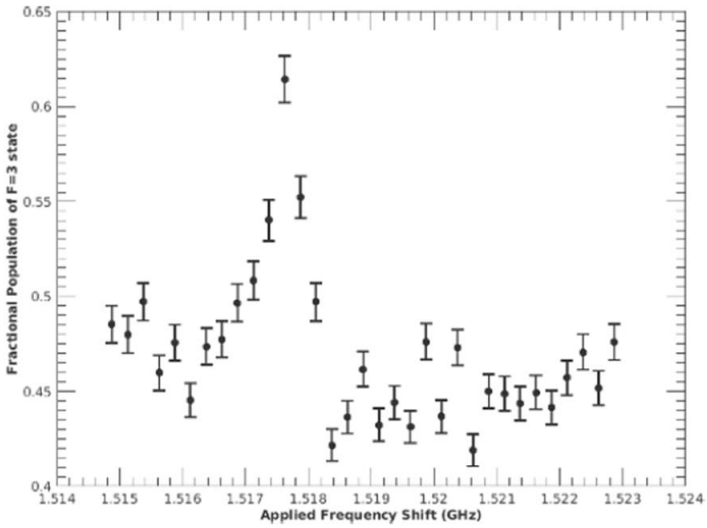

Fig. 4.1 First evidence of state manipulation via Raman beams. This data was taken with a 5 ms Raman pulse.

the Zeeman splitting. Rabi oscillation with this resonance was attempted but no indication of coherent manipulation was observed (see figure 4.2), with the population of the F = 3 state seen to asymptotically approach its peak value in $\sim$ 5 ms.

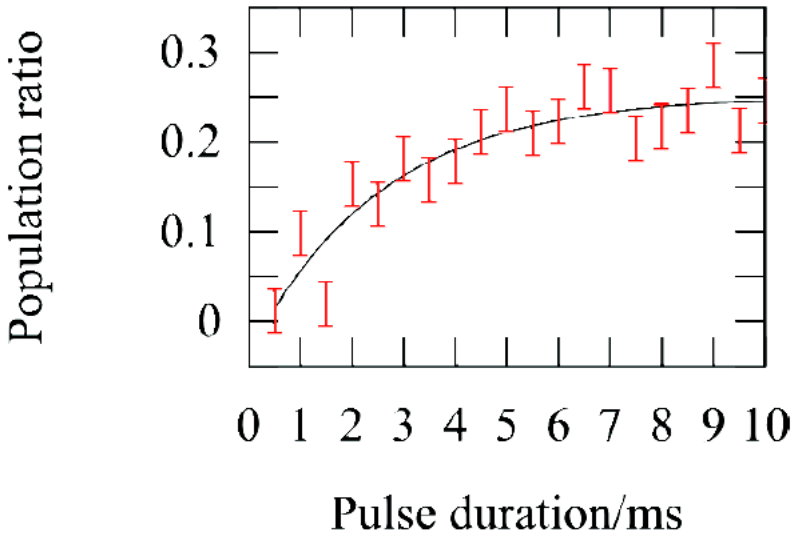

Fig. 4.2 Attempted Rabi oscillation scan shows the behaviour expected of critically damped oscillations.

Additionally, after the MOT beams were upgraded (section 3.6.1) the resonance was still visible but much less pronounced, as shown in figure 4.3. This led to the conclusion that the MOT beams were affecting the internal states of the atoms during the state manipulation phase. It was therefore decided to improve the system, primarily by enhancing the signal-to-noise ratio to reduce the need for repeated scanning of the same data ranges, making the procedure faster and more reliable.

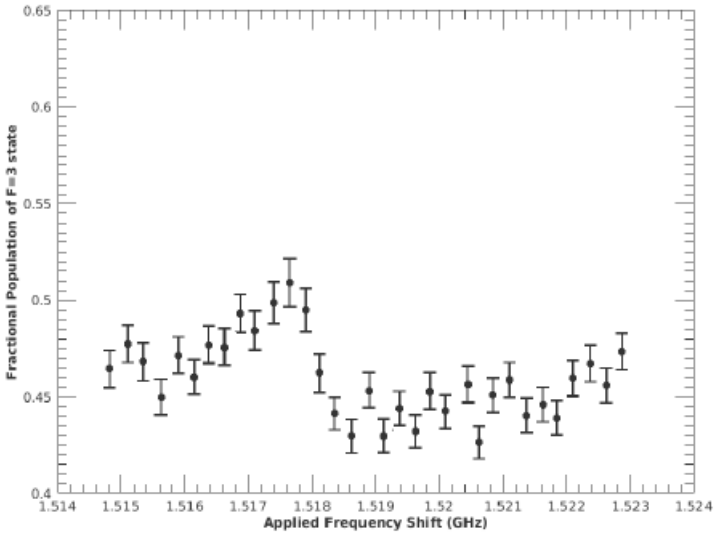

Fig. 4.3 The peak contrast measured after the beam delivery system was upgraded. With reference to figure 4.1, the contrast has reduced from around 0.15 to 0.06.

4.2 Signal to Noise Improvement

Figure 4.4 shows the signal from the state detection system used to infer the population ratio

$$Ratio \equiv R = \frac{P_{F=3}}{P_{F=2} + P_{F=3}}, \tag{4.1}$$

where $P_{F=2}$ and $P_{F=3}$ are the F = 2 and F = 3 populations respectively. As discussed in section 3.10, the area beneath the exponentially decaying segment of the signal is proportional to the state population.

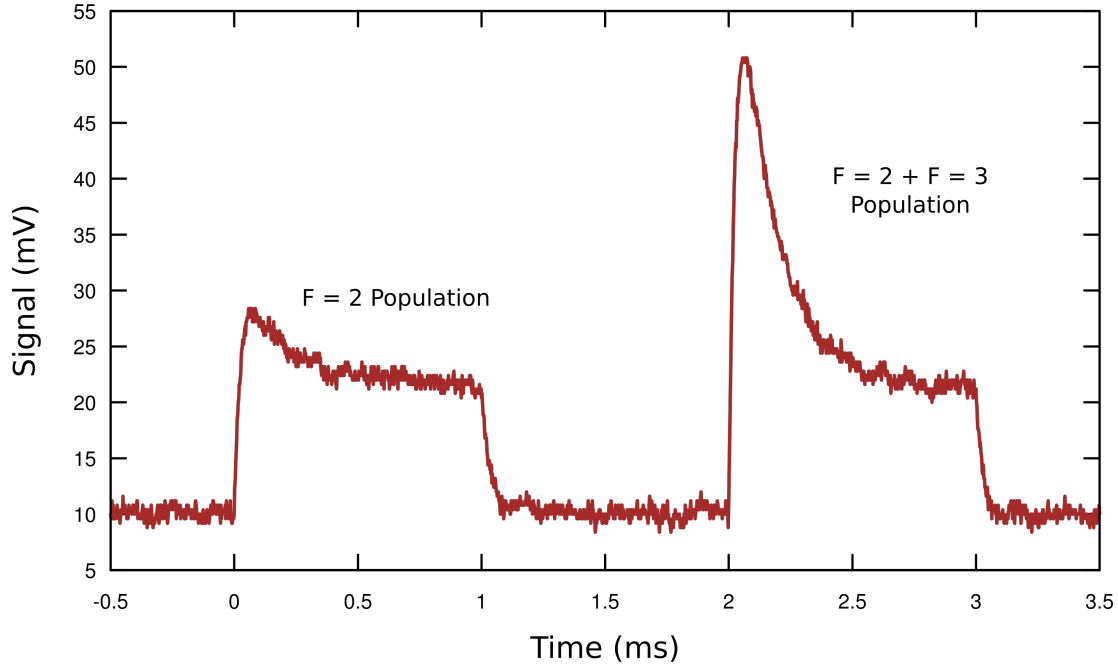

Fig. 4.4 Example state population measurement with the Raman beam path blocked.

It can be observed from figure 4.4 that exponential signal decays may be seen in both peaks, indicating a significant F = 3 population. It was found that this large population transfer to F = 3 was independent of the frequency of the Raman beams and significant F = 3 state populations were observed even when the Raman beam sequence was absent. This showed that either the state preparation stage was not completely depopulating the F = 3 state or another interaction was causing the atoms to be excited.

To ensure that the state preparation stage was working as expected, figure 4.5 was produced. The sum of the first two stages of the 'state preparation' stage was held constant (see figure 3.32) and the length of the last stage pumping atoms into F = 2 was linearly varied. The x-axis therefore indicates the variation of the time during which there was only the cooling component present in the MOT beams. The y-axis is the ratio of the heights of the first and second peaks. Figure 4.5 demonstrates that, after 1.6 ms, the state preparation reaches an

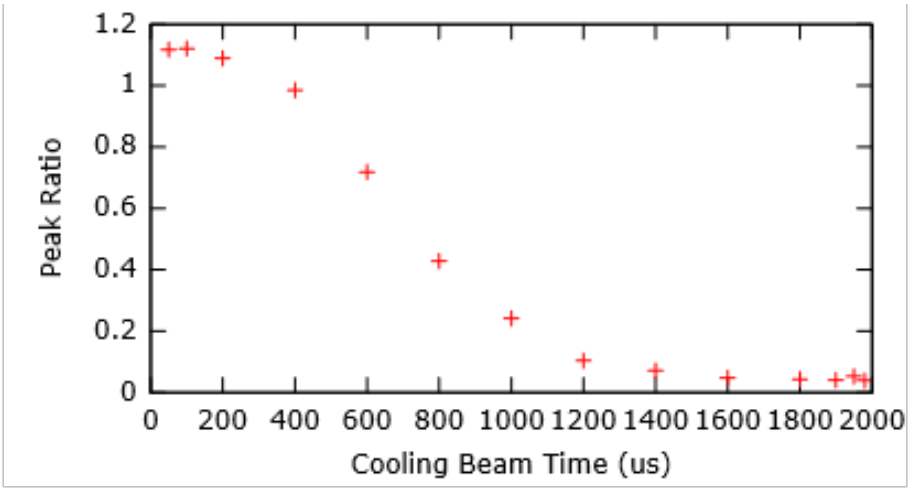

Fig. 4.5 Example of state preparation stage calibration, showing the F = 2 state becoming fully depopulated after 1.2 ms.

asymptote. A greater than unity peak ratio value for small cooling beam times is caused by the signal height reducing as the atom cloud falls out of the MOT beams. This plot shows that the initial state population approaches an asymptotic value around 5%. The value of this asymptote would vary greatly, however, indicating the presence of non-Raman interactions after the state preparation stage.

Given the change in the resonance measured after the MOT beam upgrade, 'contaminant light' was suspected in the MOT beams. Due to the atom cloud preparation, state manipulation and state detection all occurring in the crossover area of the MOT beams, any 'leaked' laser light incident upon the atoms when the MOT beams are switched off could cause the non-zero F = 3 population and explain the change in the Raman resonance.

4.3 Reduction of Contaminant Light

To locate and minimise the various sources of contaminant light in the chamber, the power downstream of the repumper and trap beam combination PBS in figure 3.16 was measured, for various AOM settings. Measurement here allows the unwanted light getting into the chamber via the MOT beams to be quantified without disrupting the MOT beam alignment.

The attempt to reduce this background light is described for each AOM below, as well as reduction of the resonant light entering the chamber via the Raman system collimator.

4.3.1 AOM0

The configuration of AOM0 is shown in figure 4.6a. It was assumed in this setup that a half waveplate can direct all of the power towards AOM0, with negligible power transmitted towards PBS1. By varying the half waveplate and measuring the power that is reflected from PBS1 it was found (see figure 4.7) that the minimum power that is transmitted by PBS0 and then reflected off PBS1 is 92 μW, for a total input power of 310 mW. This resulted in μWs of cooling light power reaching the power balancing system.

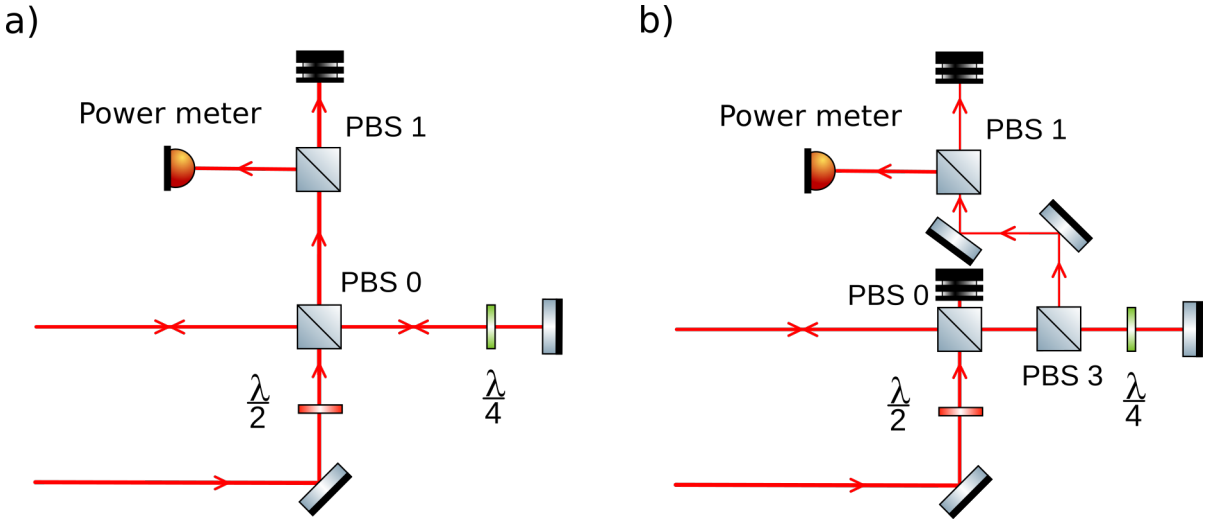

Fig. 4.6 Figure a) shows the previous PBS configuration, and figure b) the improved configuration. An extra PBS, labelled PBS3, is inserted to reduce the contaminant light. 156 mW of power is observed at the power meter when AOM0 is on.

To correct this, the cooling laser PBS setup was altered, as shown in figure 4.6. By inserting another PBS into the circuit, the direct route between PBS0 and PBS1 can be blocked, greatly reducing the power along this path when AOM0 is switched off. The double-passed light is then rerouted via PBS3 and a pair of steering mirrors, requiring everything downstream to be realigned. This modification results in a power loss of a few mW, both via the light

now hitting the beam dump and also the extra component inefficiencies. The unwanted light along this path is, however, reduced from 92 μW to 1.6 μW.

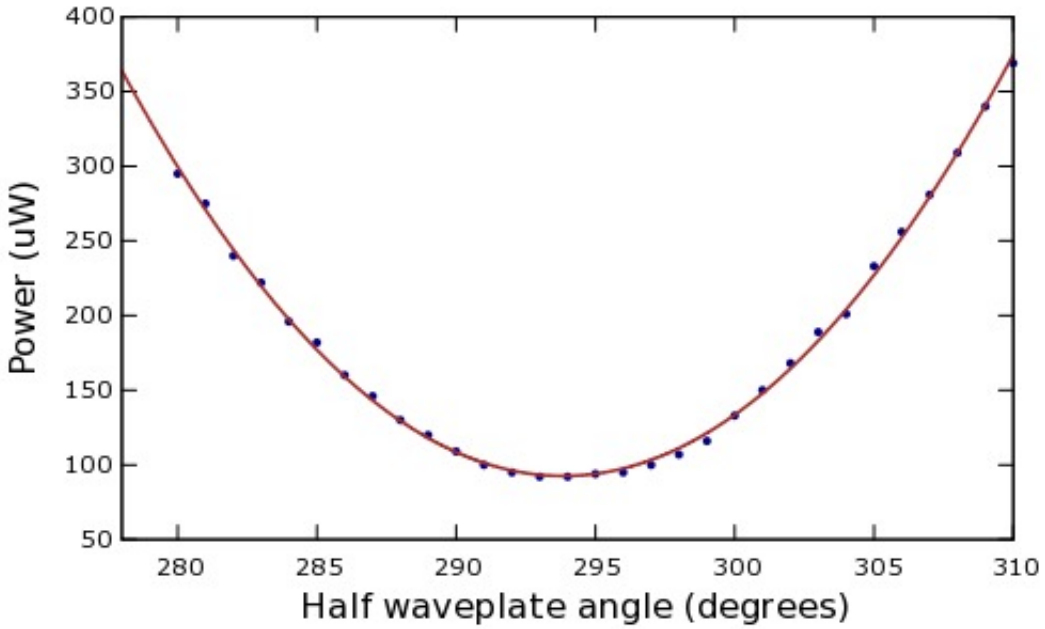

Fig. 4.7 Variation of waveplate angle shows that contaminant light passing through AOM0 could not be reduced below 92 μW.

4.3.2 AOM1

With both AOM0 and AOM1 switched on, a cooling power of 63 mW was measured at the combination PBS. When AOM1 was switched off, this reduced to 120 nW, giving a leaked light ratio of 1.9×10^{-6}. Two causes were found for this 'leaked' light through AOM1. The first was a retro-reflection along the state selection arm, causing light to be returned via the PBS when AOM1 was switched off, passing back through AOM1 and then into the chamber. The other cause was a reflection from the mirror on the upshifted arm of AOM1 (see figure 3.10).

The state selection system on AOM1 is currently not in use, so a beam dump was placed as near as possible along this pass, spatial constraints permitting. This resulted in a leaked light measurement of 113 nW, reducing the unwanted power by 7 nW. The state selection

path was therefore found to contribute only minimally to the leaked light, with no redesign required for future use.

The power reflected from the retro-reflecting mirror back through the AOM was measured to be 49 μW. When the retro-reflecting mirror was blocked, the leaked light measured at the PBS fell dramatically from 113 nW to 67 nW, showing that this is the major contribution to contaminant light via AOM2. Obviously blocking this mirror is not a viable long-term solution to this problem. Repositioning of this AOM may lead to a reduction in diffractive inefficiencies, and shutters will also reduce the power travelling to the vacuum chamber via this route. This was deemed unnecessary, however, due to the configuration of AOM0 being switched on and AOM1 switched off never occurring in the frequency scan program.

4.3.3 AOM2

AOM2 is used to switch the repumper beam on and off. The repumper power measured at the combination PBS, with AOM2 switched on, is 3 mW. When AOM2 is switched off, this reduces to 40 nW, with a 10 nW contribution from background light, giving a leaked light ratio of 1×10^{-5} and showing that a far larger fraction (4:1) of the repumper beam than the cooling beam is constantly in the chamber when the beams are nominally switched off.

As seen in figure 3.11, the PBS is deliberately configured so that any incorrectly polarised light, as it enters the PBS, is reflected onto a beam dump. This prevents light from bypassing the AOM and travelling straight to the chamber. The PBS used (CM1-PBS252) is designed for use in a transmission configuration, meaning that any light that passes through this PBS should be horizontally polarised, with an extinction ratio[2] of 1000:1. When AOM2 is switched off, any light that travels undeflected through the AOM and reaches the second PBS should also be horizontally polarised and very little should reflect off the diagonal interface of the PBS. When this light was measured, however, it was found to have a power of 572 μW,

[2]The extinction ratio is defined as the minimum to maximum transmission power of a linearly polarised input beam.

compared to the 14 mW which are transmitted. This indicates that the light which travels through the AOM accumulates a change in polarisation angle of around 3°.

With such a large contribution of leaked light via this channel, it is perhaps surprising that more repumper light is not measured going into the chamber. The reason for this is that the repumper and contaminant light take opposite routes around the AOM2 circuit, meaning that beams reflect off PBS3 at slightly different angles. An iris is therefore used to block most of the light from this unwanted path.

4.3.4 Raman System

Figure 3.27 shows that in the Raman system, light passes first through the Brimrose AOM and is then retro-reflected via a concave mirror to perform a second pass. As the Raman system is extremely well aligned, it is possible for the light which is not diffracted into the R2 beam path to travel back along its original path and eventually reach the chamber via the MOT beams. This is another source of contaminant cooling light reaching the chamber, with the largest effect during the Raman sequence when most light is being sent to the Raman system.

To prevent this, a 35 dB optical isolator (IO-5-780-VLP) was installed in the optical circuit before the Brimrose. When AOM0 is switched off, 220 mW of power is sent towards the Brimrose AOM, which is reduced to around 120 mW via neutral density filters. Before the isolator was installed, the cooling power reaching the combination PBS was measured when AOM0 was off and AOM1 was on. In this configuration, 1.75 mW of unwanted cooling power was observed. After the isolator was installed, this was reduced to 60 nW.

Leakage is also possible via the Raman collimator, with light reaching the chamber via the Raman system even when the Brimrose is switched off. This was measured, however, and found to have a sub nW effect.

4.3.5 Shutters

Besides the specific solutions discussed above, a more general solutions is simply the installation of optical shutters on each of the beam paths (see 3.3.3). These shutters do, however, have an opening and closing time of around 2.5 ms, allowing contaminant light into the chamber during this time.

4.3.6 Summary

After all possible sources of MOT beam contamination were identified and minimised, the oscilloscope signal with no state manipulation was as shown in figure 4.8. The amount of total contamination measured at the combination PBS was reduced from 100s of μWs to around 10 nWs, where this value represents an upper limit to the amount of light actually entering the chamber; the coupling efficiency of around 50%, reflections from windows etc implies a value closer to a few nW. This reduction causes the F = 3 state to remain depopulated in the absence of any deliberate state manipulation. This change can be seen in the difference between figures 4.4 and 4.8, with a background reduction of around 10 mV but an *increase* in overall signal size by around 35 mV. With the reduction of contaminant light, it was hoped that the scattering rate from contaminant light was reduced enough to allow atomic coherence to exist for sufficient time to be observed. The microwave horn scans were therefore repeated to search for Rabi oscillations.

4.4 Microwave Horn Scans

The inability to observe any coherent manipulation of the atomic states resulted in the belief that the lack of coherence might be due to the Raman system. To perform an independent check, the Raman system was blocked and a microwave horn was used for state manipulation (see section 3.8 for horn installation and calibration).

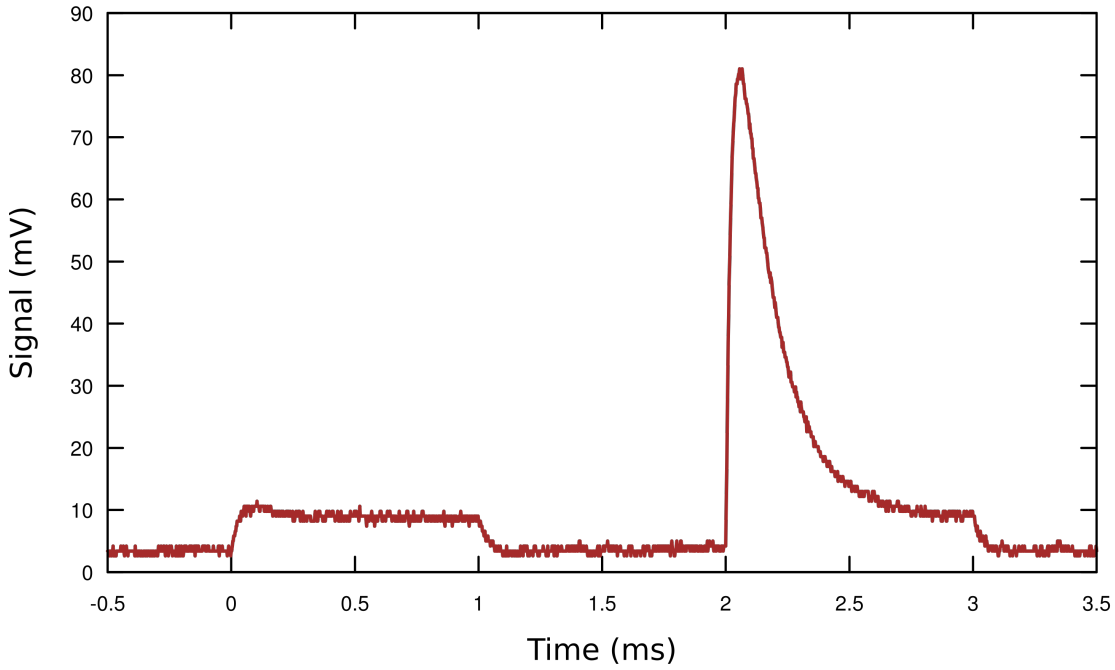

Fig. 4.8 Photodiode signal example plot. The shutter gap which was eventually inserted between the first cooling pulse and the repumper pulse has been removed for easy comparison with figure 4.4.

4.4.1 Frequency Scans

Figure 4.9 is a frequency scan using the microwave horn. The scan is performed in 10 kHz steps and each data point is averaged four times. The x-axis shows the frequency offset from the current leading empirical measurement of the $m_F = 0 \rightarrow m_F = 0$ transition between the $F = 2$ and $F = 3$ states, $f_0 = 1.517866220$ GHz. A bias field in the z-direction was deliberately applied during this scan, removing the degeneracy of the Zeeman substates. A narrow central peak is visible at this frequency, accompanied by a pair of much broader peaks either side.

A narrower scan across the central peak was performed with step size of 0.1 kHz, as shown in figure 4.10. Fitting the peak with a Lorentzian results in a Rabi frequency of $f = 0.439 \pm 0.03$ kHz and an offset from f_0 of $\Delta f_0 = 0.0966 \pm 0.027$ kHz.

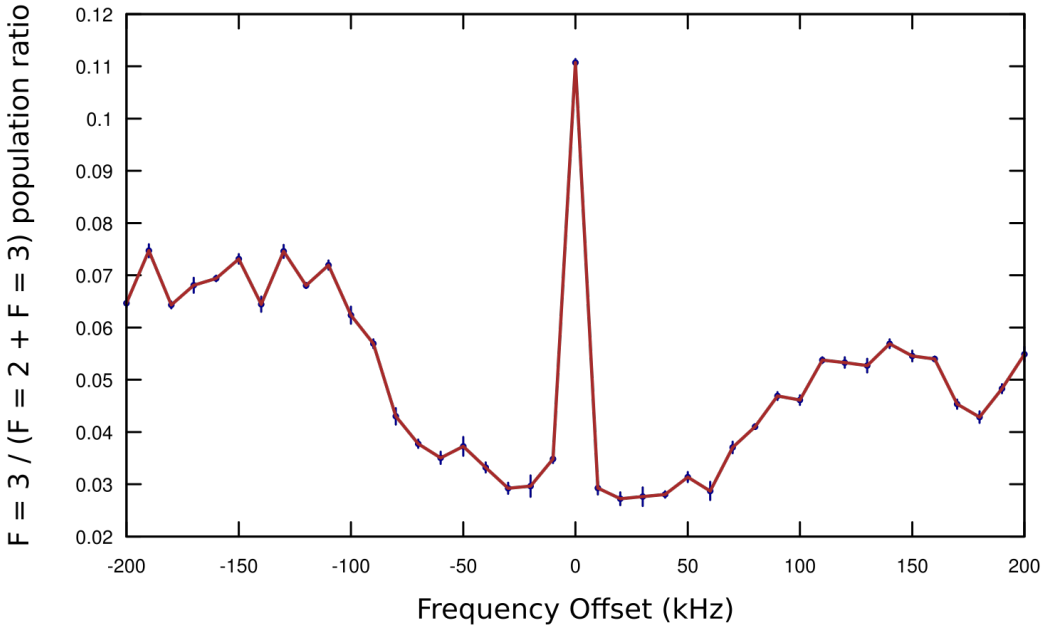

Fig. 4.9 Frequency scan with microwave horn showing central peak and broadened, magnetically sensitive side resonances.

This data shows a noticeable lack of secondary 'lobes' associated with the sinc-squared function expected via equation 2.50, despite repeated efforts to observe them. For this reason the simpler Lorentzian function is used to infer the resonance height, width and offset.

4.4.2 Data Readout and Errors

The state detection system utilises a Thorlabs PDA36A-EC photodiode which reads out to an oscilloscope. This photodiode has a single data point measurement error of 1.1 mV. Every state detection measurement consists of 500 voltage measurement data points. Each oscilloscope trace is repeated eight times, leading to an individual data point error of $1.1/\sqrt{8} \simeq 0.4$ mV.

For an oscilloscope setting of 20 mV/division, the total oscilloscope voltage range is $20 \times 8 =$ 160 mV. The screen is split into 200 vertical slices, giving a quantisation standard deviation of

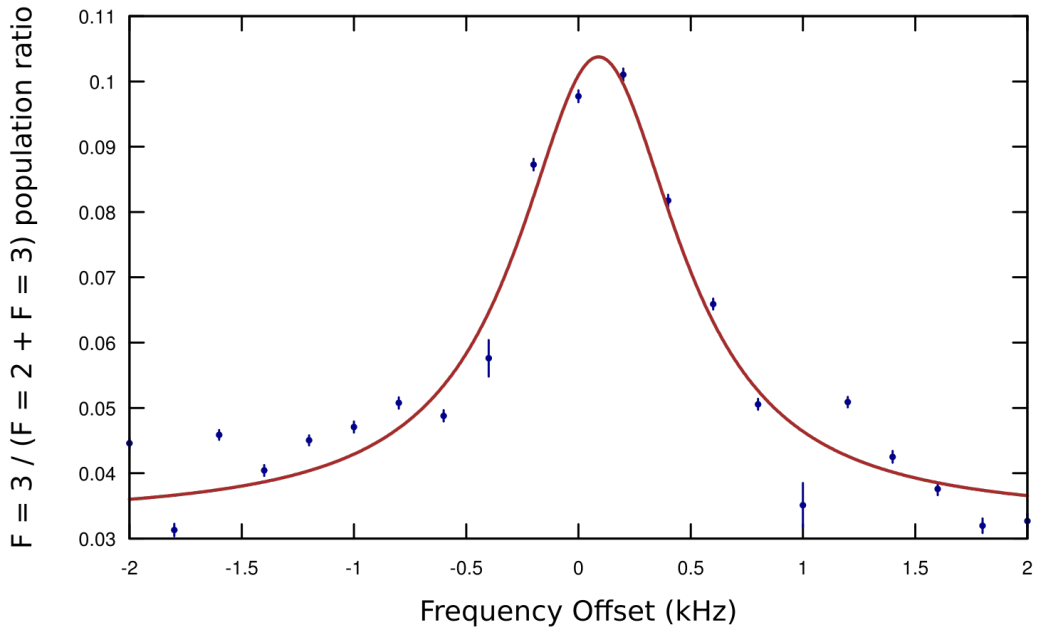

Fig. 4.10 Frequency scan of the horn central peak, with a microwave pulse time of 5 ms.

$$\sigma_Q = \frac{160/200}{\sqrt{12}} = 0.23 \text{ mV}. \tag{4.2}$$

Combining the two separate sources of error for the peak height value in quadrature gives $\Delta V = \sqrt{\Delta V^2_{Photodiode} + \Delta V^2_{Oscilloscope}} = \sqrt{0.4^2 + 0.23^2} = 0.46$ mV.

The averaged data is then analysed by using a script to identify both of the peak heights, the average flat background for each pulse and the total background. The population ratio R is then given by

$$R = \frac{h1 - b1}{h2 - b2}, \tag{4.3}$$

where h1 is the height of peak 1, b1 the fit to the flat background of peak 1, and the same for peak 2. This is permitted, rather than integrating under each peak, because the ratio of the heights of two exponential decays and the ratio of their areas is the same, provided that both

curves share the same exponential decay factor. The total error on the peak height ratio ΔR is therefore

$$\Delta R = \sqrt{\left(\frac{\Delta V}{h1-b1}\right)^2 + \left(\frac{\Delta V}{h2-b2}\right)^2} \times R, \tag{4.4}$$

giving a typical measurement error around 5%.

4.4.3 Rabi Oscillation Scan

A scan in microwave pulse length from 0 to 10 ms was performed to search for Rabi oscillations. Figure 4.11 shows a heavily damped Rabi oscillation seen at the central pulse peak frequency. The oscillation is fit with a simple decaying sine function. Using the peak width and equation 2.26 allows a comparison of the π pulse time with what is expected. A π pulse t_π must satisfy the equation

$$\Omega_R t_\pi = \pi. \tag{4.5}$$

Fitting the data with a decaying exponential resulted in a π pulse length of 3.055 ± 0.017 ms and therefore a Rabi frequency of Ω_R of $2\pi \times 163.7$ Hz.

4.5 Magnetic Spectroscopy

The magnetic field can be determined, and eliminated, by measuring the Zeeman splitting of the magnetic substates, as the current in the bias coils is varied. The individual Zeeman resonances, as shown for example in figure 4.12, were fit with Gaussian functions to determine their positions, and these positions plotted as a function of coil current, as shown in figure 4.14 where the North-South coils are varied, with the other two coils kept constant. The

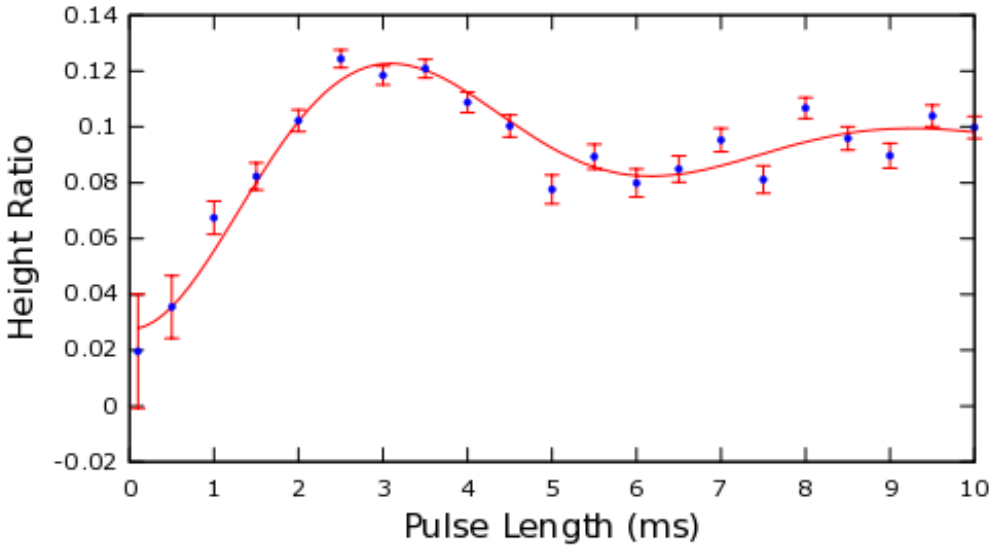

Fig. 4.11 Rabi oscillation with microwave horn. Coherent oscillations are clear if heavily damped.

constant currents were chosen so that the separate peaks do not overlap, but nor are they so distant that scanning across every peak in a sensible time frame becomes unfeasible.

The microwaves that are emitted from the horn are linearly polarised, which would drive π transitions if the horn were positioned either parallel or perpendicular to the quantisation axis. Due to the spatial constraints caused by the MOT beams, however, the horn is in neither of these positions. It is therefore expected that the horn will drive both $\Delta m_F = 0$ and $\Delta m_F = \pm 1$ transitions. The five clearly visible peaks in figure 4.12 are therefore expected to be, from left to right, $m_F = -1 \rightarrow m_F = -2$, $m_F = -1 \rightarrow m_F = -1$, $m_F = 0 \rightarrow m_F = -1$, $m_F = 0 \rightarrow m_F = 0$ and $m_F = 0 \rightarrow m_F = 1$. This is due to the $m_F = 0 \rightarrow m_F = 0$ peak being magnetically insensitive to first order and the other transitions being the closest energetically to this peak (see figure 4.13).

The Zeeman splitting for each hyperfine substate is given by

$$\Delta E_{Zeeman} = \mu_B g_F m_F |B|, \tag{4.6}$$

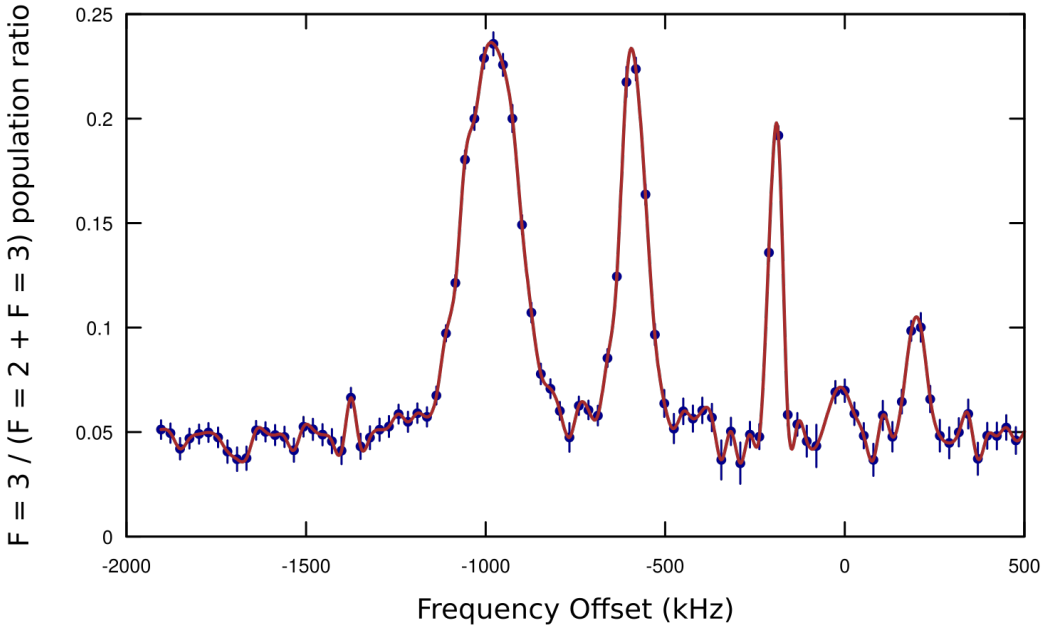

Fig. 4.12 Wide frequency scan showing several resonance peaks, the separation of which gives an indication of the magnetic field strength.

where the Landé g-factors are $1/3$ and $-1/3$ for the F = 3 and F = 2 states respectively. The two levels therefore split in opposite directions, as shown in figure 4.13.

The total splitting between the states is therefore given by

$$\Delta E_{hyperfine} = \hbar\Delta\omega = \hbar\omega_0 + \mu_B|B|(g_{F=3}m_{F=3} - g_{F=2}m_{F=2}). \tag{4.7}$$

Inserting the Landé g-factors gives

$$E_{hyperfine} = \hbar\omega = \hbar\omega_0 + \frac{1}{3}\mu_B|B_0 + B_I|(m_{F=3} + m_{F=2}), \tag{4.8}$$

where B_0 is the sum of the magnetic field without the coils, the Earth's magnetic field etc., and B_i is the magnetic field induced by the bias coils. Rearranging equation 4.8 to give the energy offset and assuming that magnetic field B is a linear function of current I gives

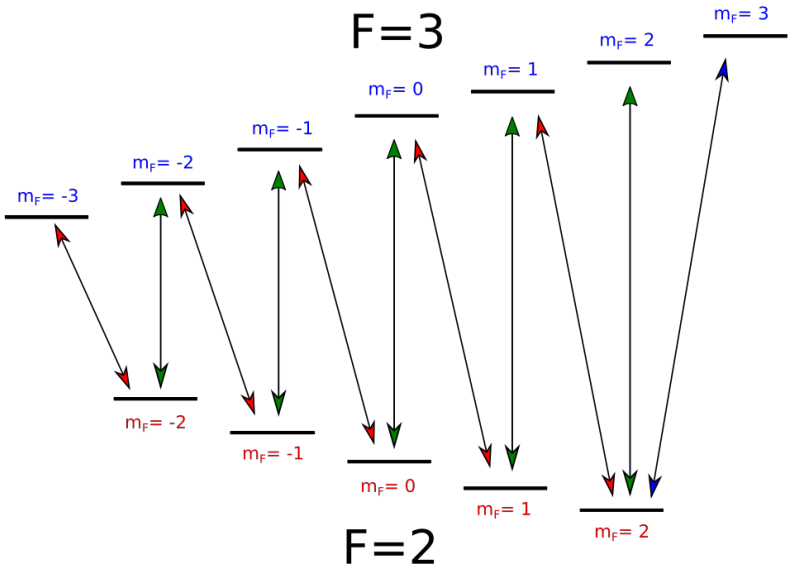

Fig. 4.13 Diagram showing the single-photon transitions between the hyperfine ground state of rubidium-85 which are permitted by the selection rules. The distance between the levels is indicative of the hyperfine energy splitting. The arrows shown are the 11 non-degenerate single-photon transitions.

$$\Delta E_{hyperfine} = \hbar(\omega - \omega_0) = \frac{1}{3}\mu_B(kI + B_0)(m_{F=3} + m_{F=2}), \tag{4.9}$$

where k is some constant of proportionality with dimension T/A. This shows that the energy levels are evenly spaced with energy difference from the $m_F = 0 \rightarrow m_F = 0$ transition being a constant multiplied by sum of the magnetic substate quantum numbers, as shown in figure 4.13. Fitting the non-$m_F = 0 \rightarrow m_F = 0$ peaks with straight lines and inferring the gradient and crossing point allows the inference of the magnetic field via

$$B_I = \frac{3Ih}{\mu_B m_l (m_{F=3} + m_{F=2})} \tag{4.10}$$

where m_l is the line gradient and a factor of 2π has been dropped to convert between ω and f. The 'background' magnetic field strength is given via the y-intercept

$$c = -\frac{B_0}{k}. \tag{4.11}$$

Extracting the fitting parameters from the data in figure 4.14, a conversion value of 8.406×10^{-6} T/A was found. Utilising equation 4.11 gives an approximate value of B_0 of 180 mG, which is the same order of magnitude as the Earth's magnetic field.

The error on the position of each Gaussian peak, as given by the uncertainty on the peak fit, is ~ 0.01 kHz. For this reason the error bars on these measurements are not visible in figure 4.14. The peaks all appear to shift approximately linearly with current, with a central peak independent of magnetic field strength. Figure 4.14 indicates that the current should be set to around -2.5 A to minimise the magnetic field in the North-South direction. This process was repeated for the other magnetic coils, to minimise North-South and East-West, while setting the vertical field to maintain a quantisation axis parallel to the Raman beams.

4.6 Summary

Reducing the unwanted light from approximately 100 μWs to around a nW reduces the scattering rate from 4.43×10^3 to 5.77×10^{-2} per atom per ms. For an experiment with an interrogation time of order milliseconds, it is important that is this scattering rate is less than 1. By greatly reducing these unwanted sources of interaction, clear evidence of reliable, frequency dependent state transitions was observed with a microwave horn. Evidence of heavily damped Rabi oscillations was then observed with single-photon microwave transitions. These transition frequencies were then measured as a function of magnetic field strength via the Zeeman effect. This led to the magnetic field being measured and hence minimised via adjustment of the bias coil current.

These results show that it is possible to observe coherent manipulation within the current experimental setup. Using the microwave horn allowed a very useful separate check on the experiment, showing that the atoms are sufficiently cold and the collision rate low enough

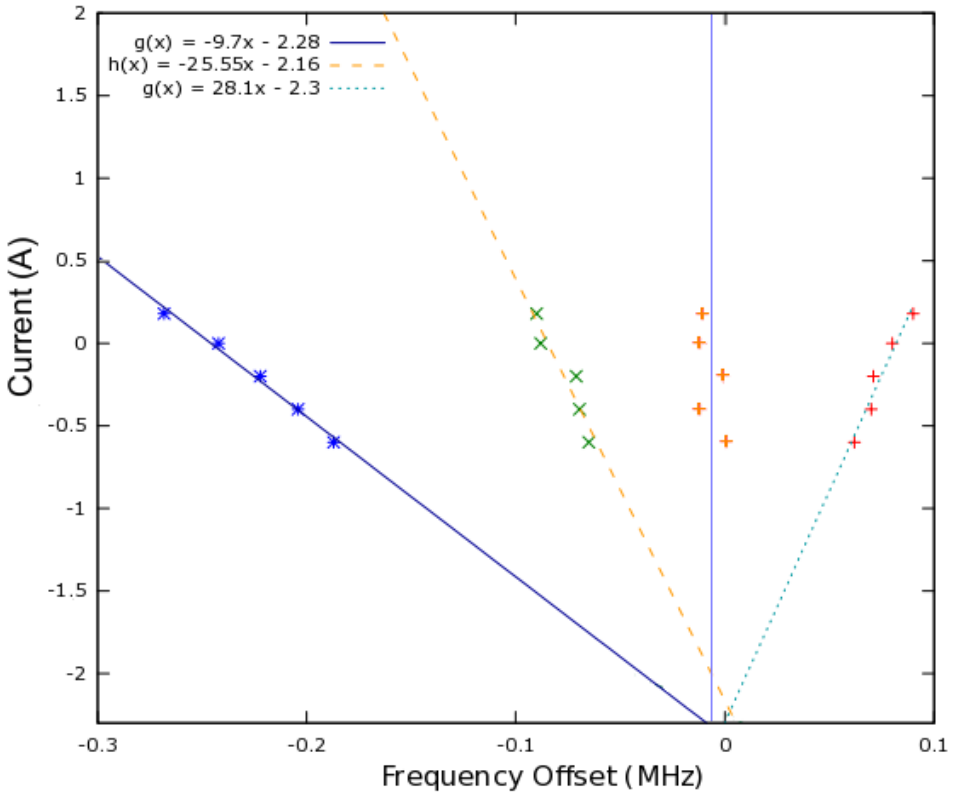

Fig. 4.14 Position of resonance peaks as the magnetic coil current is linearly varied. The $m_F = 0 \rightarrow m_F = 0$ transition (orange data points) is fit with a line which is constrained to be vertical.

to permit coherent effects. Any inability to observe Raman transitions is therefore down to deficiencies in the Raman beams.

Chapter 5

State Manipulation: Raman Beams

After coherent transitions were observed with the microwave horn and any critical decoherence effects via the MOT beams were ruled out, state manipulation via Raman transitions was then reinvestigated. Returning to the Raman beams, several upgrades were made to the Raman system before Rabi oscillations and eventually Ramsey fringes were observed.

5.1 Raman System Upgrade

5.1.1 Circular Polariser

The Raman system is coupled to the chamber via a 10 m optical fibre. The light entering the fibre is linearly polarised and set to align with the fast-axis of the fibre via a half waveplate. The fibre output light then passes through a quarter waveplate, converting linear light to circular light appropriate for the $\sigma^+ - \sigma^+$ transitions of co-propagating Raman beams.

Regular measurement of the Raman polarisation after the quarter waveplate showed that, though the preceding steps had been followed, the light could not be perfectly circularly polarised. Variations over time of the alignment of the incident light into the fast axis of

the fibre may have caused this, as well as the effects of changing laboratory conditions on the fibre itself. Changes in laboratory temperature, as well as mechanical stress on the fibre, can cause the polarisation to vary between input and output. A temperature differential along the fibre can cause the polarisation to vary because the thermal expansion changes at different points along the fibre cladding. This leads to a variation in strain and a change in birefringence. Due to the Raman delivery fibre being 10 m in length, these effects may well be amplified and thus cause the change in polarisation observed [94][95].

To remedy this effect, a circular polariser was used to replace the quarter waveplate. As shown in figure 5.1, a linear polariser is used to convert all incoming light to linear light. The light then passes through a quarter waveplate which is fixed at a 45° angle to the linear polariser. The effect of this is to guarantee that the Raman beam light is circularly polarised, and converts any variations in polarisation from the fibre to a variation in power.

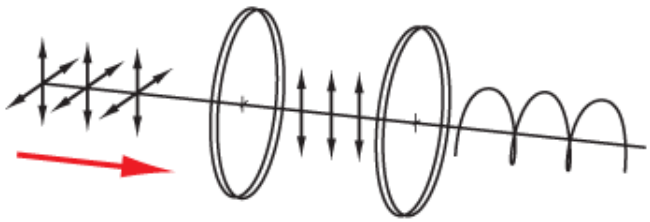

Fig. 5.1 Schematic of circular polariser. The Raman system delivers linearly polarised light to this optical element, ensuring the polarisation is correct to drive velocity insensitive transitions [96].

5.2 Raman Resonances

The scan searching for a Raman resonance as shown in section 4.1 was repeated with confidence that atom coherence would not be lost instantly due to contaminant in the MOT beams. Resonant structure was observed and the $m_F = 0 \rightarrow m_F = 0$ transition with Raman beams is shown in figure 5.2. Fitting this peak with a Lorentzian as with the peak from the

microwave horn, it was found that the peak has a width of 5.06 ± 0.24 kHz. This is much wider than the horn peak, due to the increased power broadening via the Raman beams. It is therefore expected that the Rabi frequency will be larger for Rabi oscillations via Raman transitions.

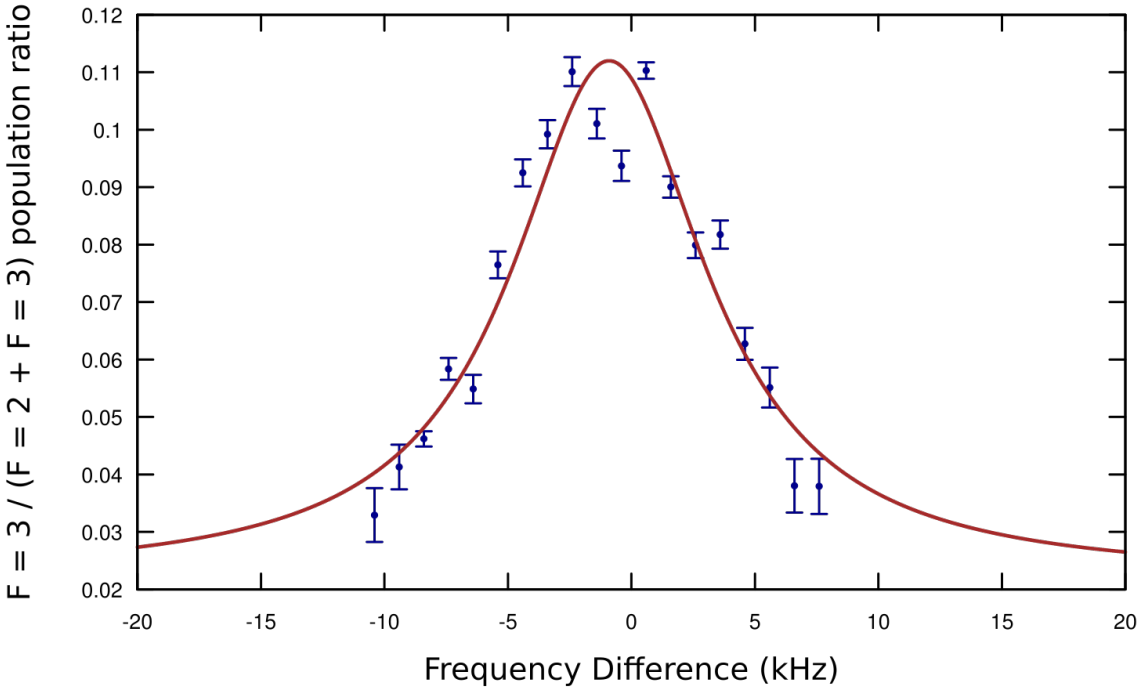

Fig. 5.2 Scan of the frequency difference between the Raman beams, offset from the empirical transition (see appendix A). This data was taken with a pulse duration of around 5 ms.

Figure 5.3 shows how the peak contrast is improved when the vertical bias coils are on and aligned 'backwards' to add to the magnetic field of the Earth in the vertical direction. The upper plot is the central resonance peak with a 'background' magnetic field, while the lower plot shows the peak when the z-coil is on, but the east-west and north-south coils are off. An increase in peak amplitude of around 20% was observed. This shows that some non-vertical component of the Earth's magnetic field remains uncancelled so that the quantisation axis is not well aligned with the direction of the Raman beams. This misalignment then causes the amplitudes for the $\sigma^+ - \sigma^+$ transitions to be reduced. Adding a strong vertical field thus increases these amplitudes and hence increases the resonance amplitude.

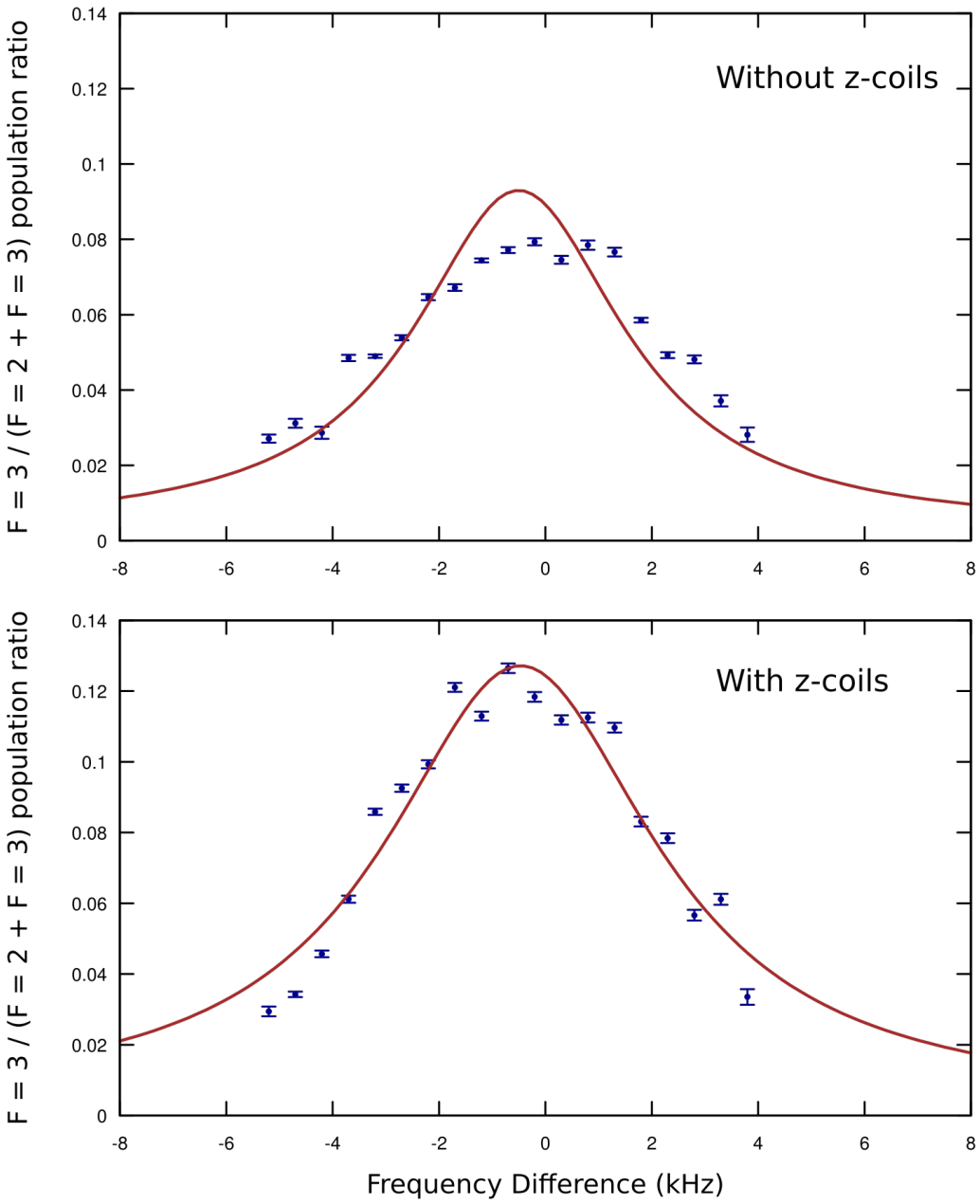

Fig. 5.3 Raman resonances fit with Lorentzian functions, for different bias field configurations. The above plots show that the amplitude with the z-coils on is larger, providing a larger signal-to-noise ratio, demonstrated by the data more closely resembling a Lorentzian distribution.

This was significant because, in the current experimental setup, the shim coils remain in their initial configuration for the duration of the scan. This means that optimising the coil currents to minimise the magnetic field, as was done in section 4.5, will both decrease the temperature of the atoms and decrease the signal of both Raman resonances and Rabi oscillations. It was

decided that having the north-south and east-west coils on to cancel any stray magnetic fields in this plane, whilst using the vertical coils to add a quantization axis, was the most effective compromise.

5.3 Rabi Oscillations

By fitting the resonance in figure 5.2 to determine the central frequency and varying the Raman pulse length, the Rabi oscillation in figure 5.4 was observed. This scan was taken with R1 and R2 powers of 3 mW and 0.9 mW respectively. It clearly shows F = 3 population oscillating as a function of pulse length, but also evidence of a strong decoherence effect, with the $F = 3$ state failing to return to $P_{F=3} \approx 0$. By fitting the decaying oscillation via a damped sinusoidal curve with a multiplicative contrast factor, a Rabi frequency of $\Omega_R = 2\pi \times 6.859$ kHz was found.

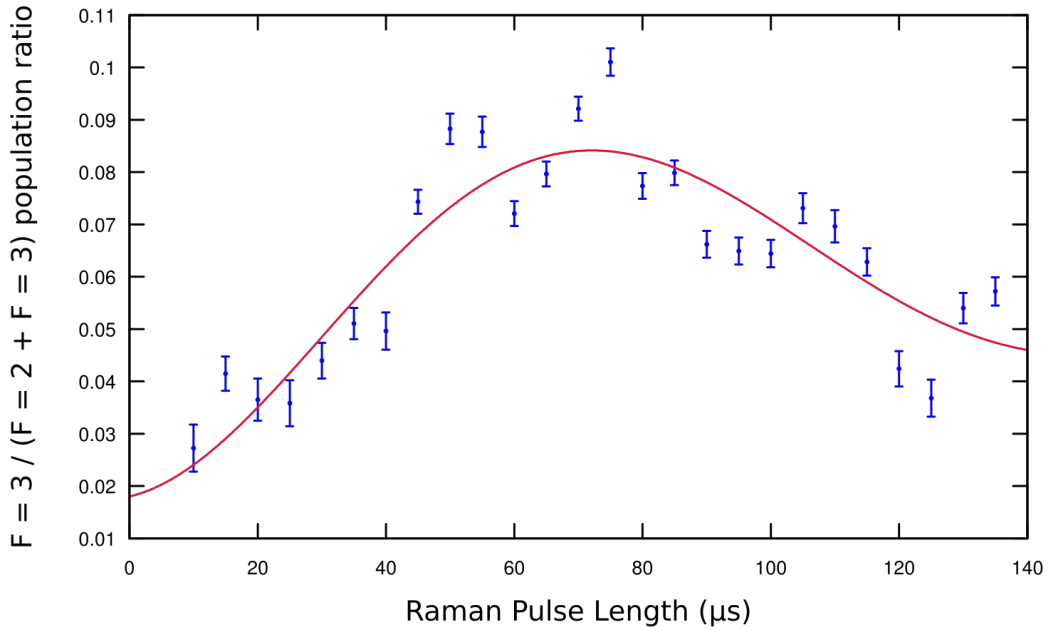

Fig. 5.4 Initial Rabi oscillation data after removal of contaminant effects and Raman system upgrade.

Figure 5.5 (left) shows the variation of the Rabi oscillations as the Raman frequency is detuned from resonance. As discussed in section 2.2.2, this causes Rabi oscillations to decrease in

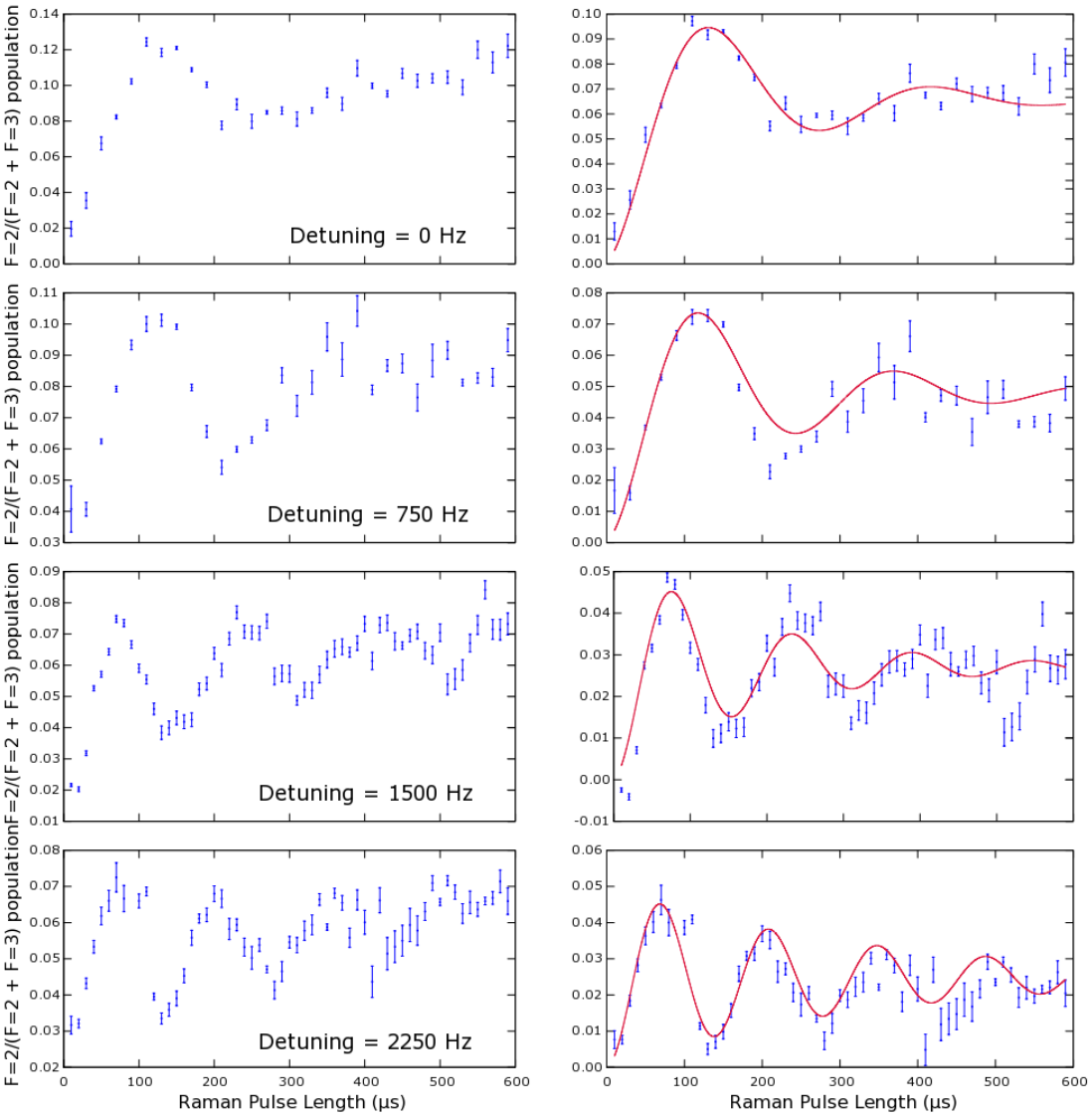

Fig. 5.5 Rabi oscillations for various detunings from resonance. The plots on the left show the linear increase in F = 3 populating mentioned earlier, due to these scans being taken without heated cells. The plots on the right have had this linear background subtracted.

amplitude and increase in frequency. By increasing the detuning, more oscillations are visible before coherence was lost. By increasing detuning, the $\pi/2$ pulse time was reduced from 80 μs to 31 μs.

These Rabi oscillation scans showed not just decoherence effects but a linear increase in the F = 3 population. It was observed that performing a Rabi oscillation scan with only the R2 beam caused a linear F = 3 population increase without the initial oscillations, as shown

by the blue line in figure 5.6. The heated cells on the Raman beam path had been removed initially to increase the Raman beam power, increasing the Rabi frequency and reducing the risk that any evidence of coherent control was being masked by decoherence effects. Inserting the heated cells back into the Raman beam path caused this effect to disappear, at the cost of a large reduction in power, from around 8 mW total power to around 5 mW. The Rabi oscillations with this linear effect subtracted are shown in figure 5.5 (right).

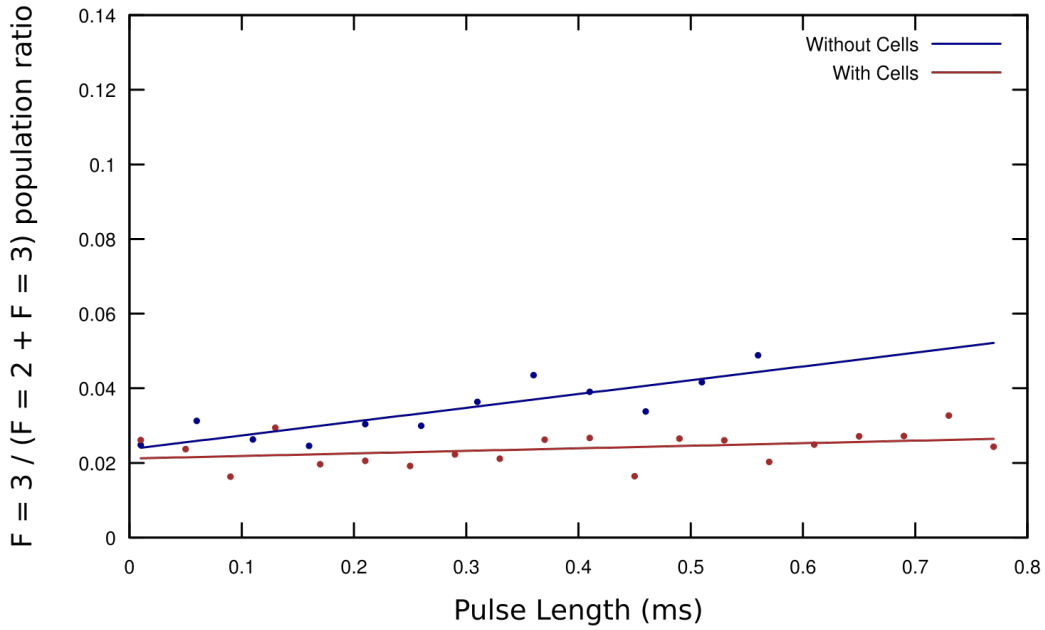

Fig. 5.6 Excited hyperfine state population as the R2 beam pulse length is increased. Both data sets are fit with linear functions.

These oscillations are a clear indication that the Raman beams are capable of coherent manipulation of the atomic states, and shows that the Rabi oscillation behaviour is in agreement with what is expected.

5.4 Ramsey Fringes

By fitting the on-resonance Rabi oscillation, a $\pi/2$ pulse time of 80 μs was inferred. By performing a scan with two 80 μs pulses separated by an interval time of 800 μs, the Ramsey

fringes in figure 5.7 were observed. This fringe pattern is a clear indication of interference effects between the states.

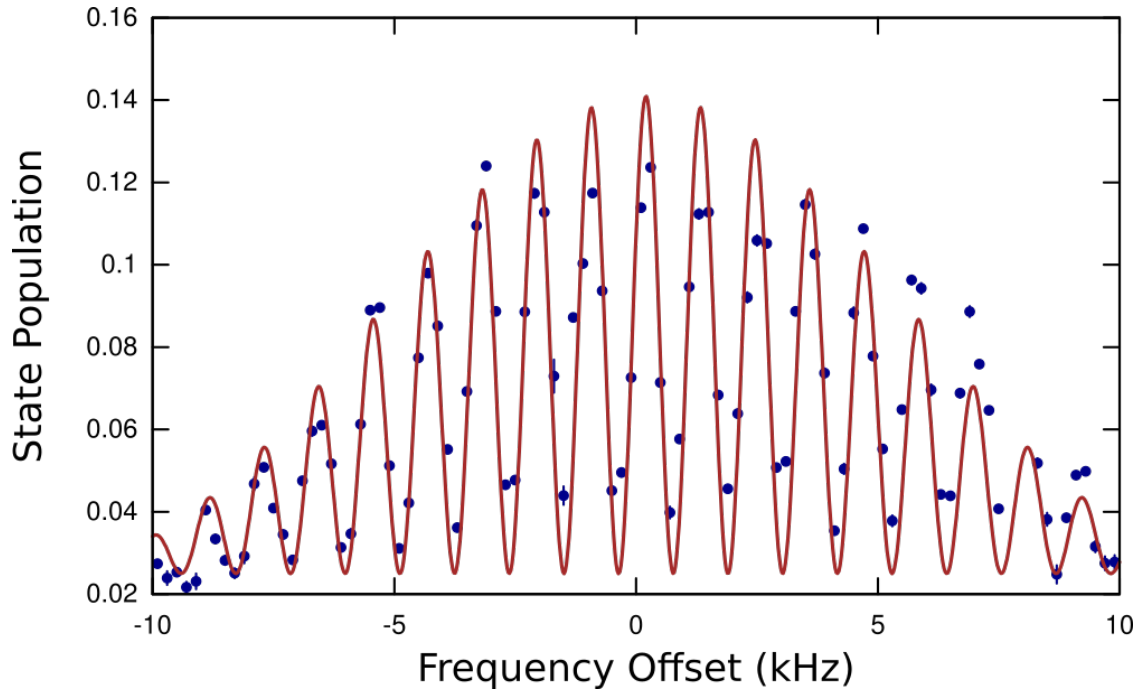

Fig. 5.7 Ramsey fringes with an interval length of $T = 0.8$ ms. A slight offset from the theoretical central frequency is clear, caused by the AC Stark shift.

By increasing the interval time between the two pulses, it is expected that the Ramsey envelope will remain the same width but there will be a greater number of fringes. This is shown in figure 5.8, where the interval time is increased in steps of 0.3 ms. In order to keep the shutters synchronised with the delayed state detection pulses as the Ramsey pulse interval becomes longer and longer, it was decided to set the total time between the first Raman pulse and the state detection pulse to be equal to a constant 5 ms. The sequence therefore included two Raman pulses, an interval time between the pulses with no Raman beams present and a time between the last Raman pulse and the state detection pulses called the 'buffer'. This way, increasing the interval time and concomitantly decreasing the buffer time allowed the shutters to remain synchronised. The benefit of this method over changing the shutter timings is that pushing the state detection pulses later and later causes the fluorescence signal shape to change, potentially affecting the data analysis. Keeping the state detection pulse timings the same for every scan prevents this problem. The error on the position of the central fringe,

as given by the fit uncertainty, is around 25 Hz for an interval time of 0.8 ms. This means that the central resonance frequency, and hence the hyperfine energy splitting, can be measured to around 1 part in 10^8, giving a value of 3035732838 ± 25 Hz [97] [98]. Deviations from the expected value of 3035732440 may be ascribed to uncancelled AC Stark shift.

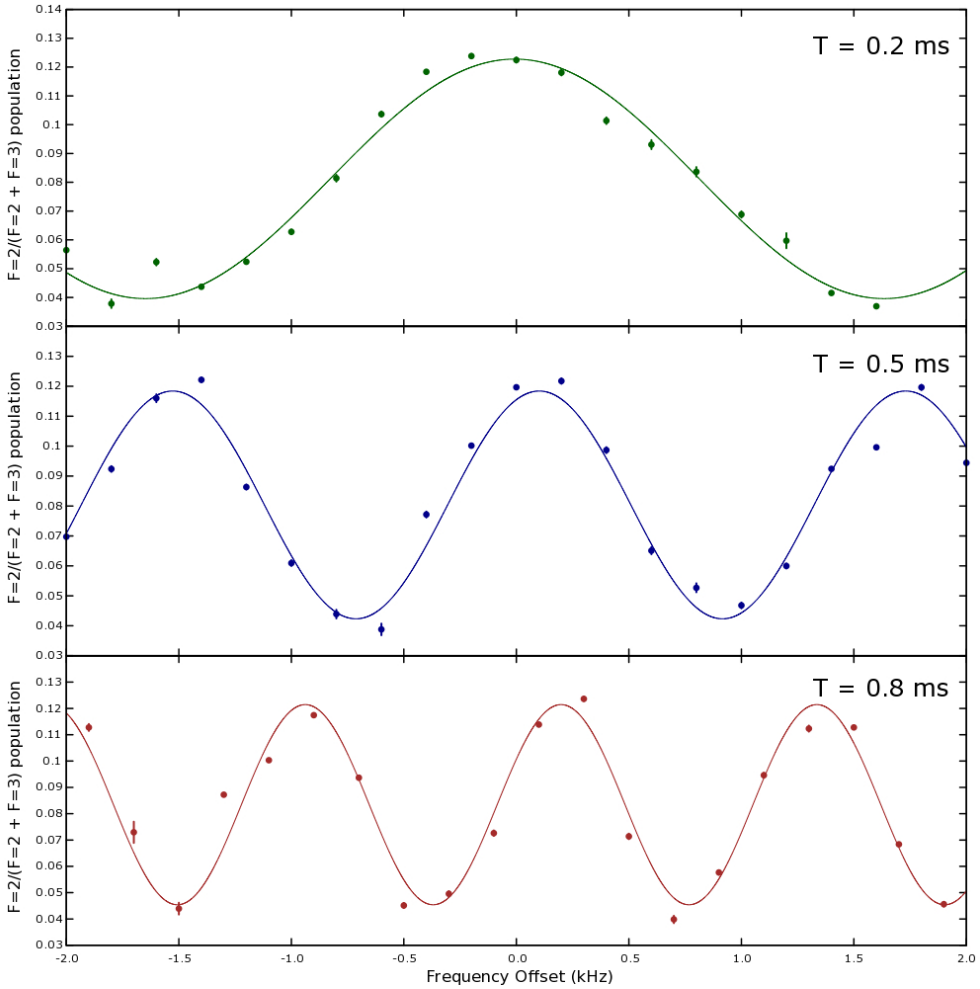

Fig. 5.8 Ramsey fringes as a function of interval length. For $T = 0.8$ ms, the central frequency offset was found to be 0.19 ± 0.01 kHz.

For a consistency check, the Ramsey fringes for various interval times were fit with sinusoidal functions giving the fringe periodicity from which the inferred interval times were calculated. The comparison of the interval time between the pulses in the interferometry sequence and the inferred interval time is shown in figure 5.9. This shows that the fringes measured are

in good agreement with what would be expected for the programmed pulse timings and intervals, giving confidence in the observed Ramsey fringes.

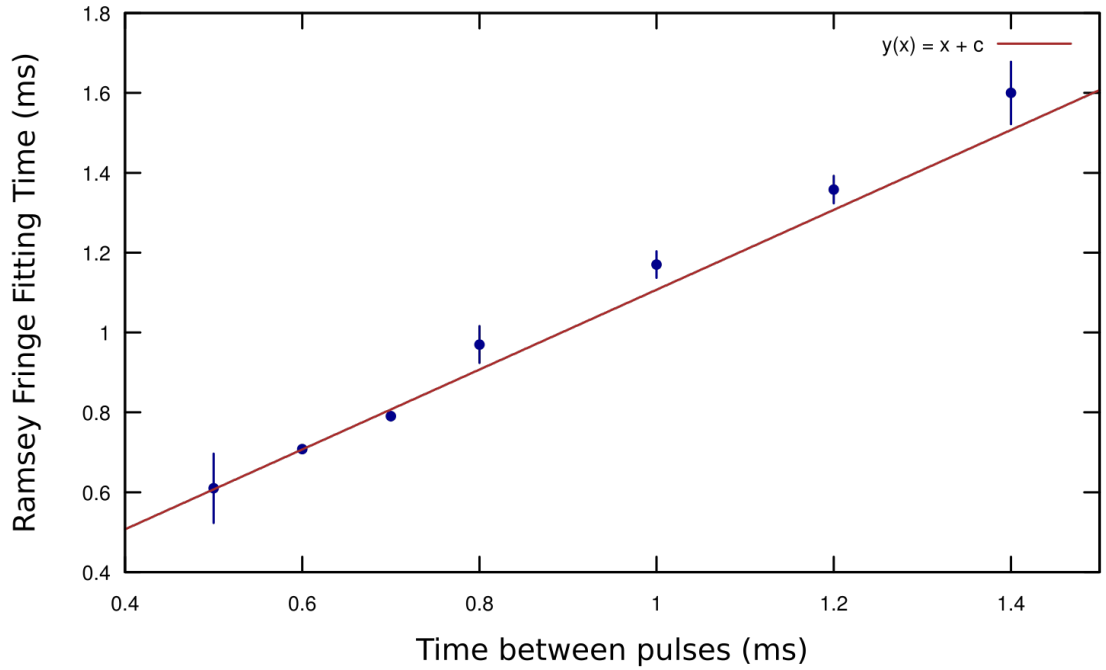

Fig. 5.9 Consistency check between the fitting parameters and the Ramsey sequence pulse settings. The proximity to the red line shows how close the expected and measured pulse intervals are, for some given offset c. By fitting with a straight line with a gradient equal to unity, this offset was found to be 0.107 ± 0.008 ms. This discrepancy may be caused by assumptions involved in deriving the Ramsey fringe equation, the pulses not being perfectly square etc.

5.5 Loss of Coherence

By increasing the Raman pulse interval for the Ramsey fringe sequence, the number of fringes increases, as shown in figure 5.8. This allows the central frequency to be more accurately determined, so it is natural to make this interval as large as possible. It was found, however, that after around 0.8 ms, the contrast of the fringes starts to decrease, as shown in figure 5.10.

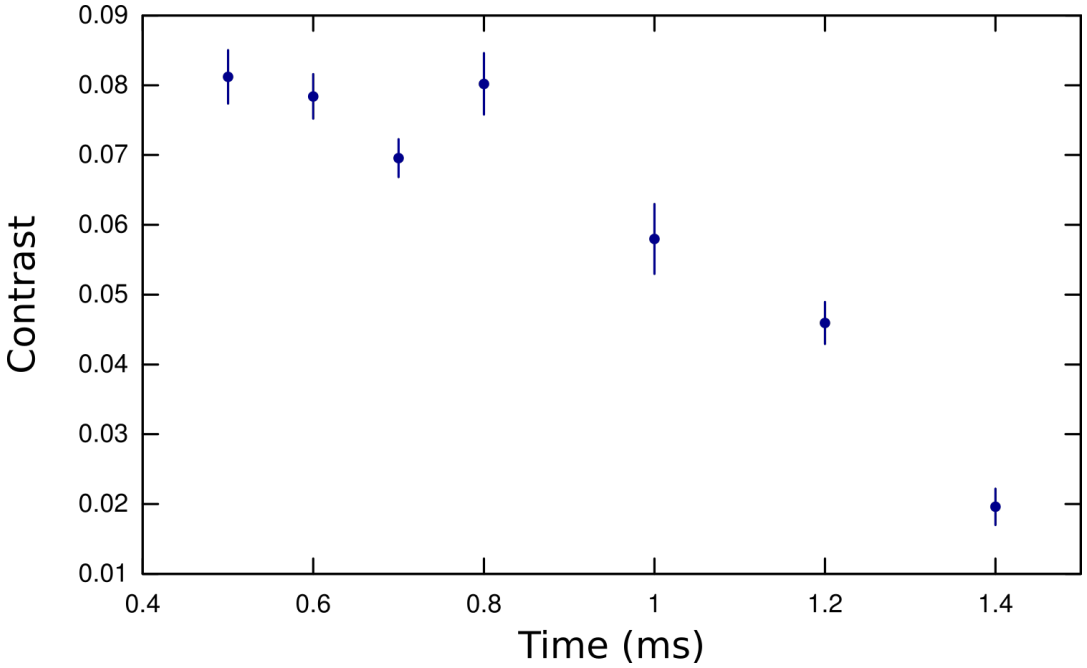

Fig. 5.10 Decrease in the fitted central fringe amplitude as the pulse interval time is increased.

This loss of contrast can also be displayed by performing a Ramsey scan over interval time rather than frequency. The Raman frequency is deliberately set off-resonance, then the interval time is scanned, resulting in the decaying oscillation curve shown in 5.11. Both of these plots show that beyond around a millisecond, either dephasing or decoherence begins to severely damp the interference fringes, with all evidence of fringes extinguished after around 1.5 ms [99].

5.6 Sources of Decoherence

To increase the precision of the Ramsey sequence frequency measurement, causes of decoherence must be identified and eliminated. Some of the possible causes of decoherence are discussed below (see eg. [46] for more information).

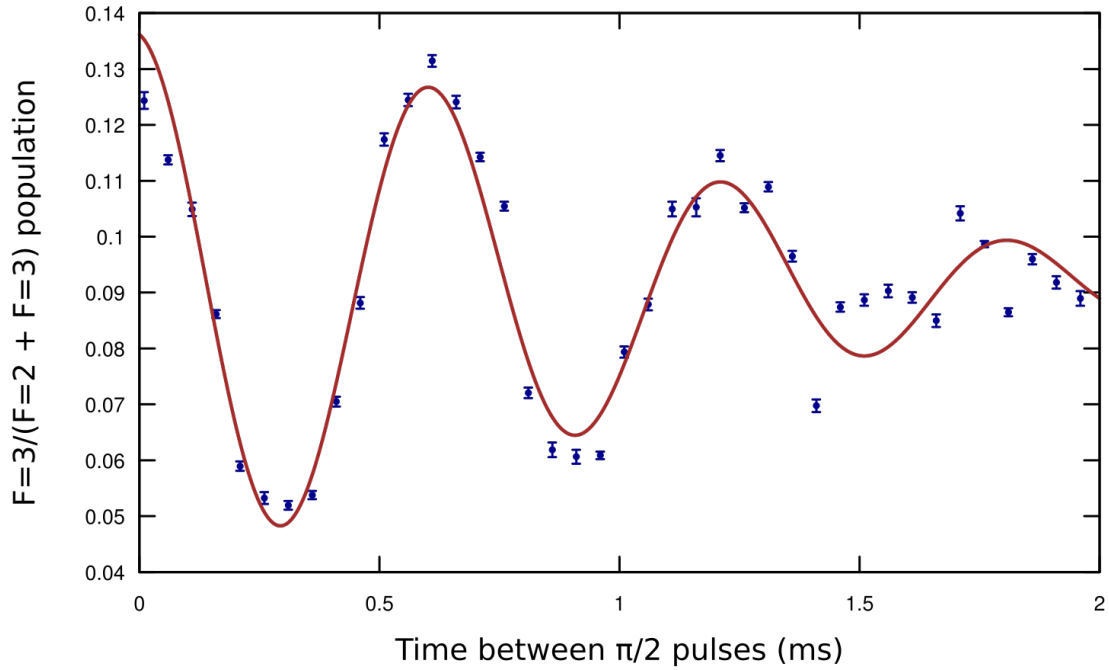

Fig. 5.11 Decrease of the Ramsey fringe contrast as the time between Ramsey pulses is increased. The Raman beam detuning is set to be 3 kHz away from resonance. Data was fit with a decaying sine curve.

5.6.1 Atomic Collisions

Collisions between the cooled ^{85}Rb atoms or between the atoms in the MOT and the background vapour atoms, particularly ^{87}Rb atoms, will cause decoherence. For our setup, however, this is unlikely. The vacuum pressure in the chamber is consistently of order 10^{-9} mBar, and damped microwave horn oscillations were observed over an order of magnitude longer time than the Raman oscillations, suggesting that collisions might be the cause of the horn oscillation damping, but not the Raman damping.

Inter-cloud collisions may explain the difference in coherence times between the horn and Raman beam setups. For the horn measurements, the field was approximately cancelled, whereas for the Raman scans the ambient field was amplified to increase the signal size. This increase in magnetic field could cause an increase in cloud temperature and hence decrease the coherence times observed.

5.6.2 On-Resonant Light

As discussed in chapter 4, reduction of on-resonant light, particularly light which entered the vacuum chamber during the state manipulation phase via the MOT beams, was a critical factor in observing coherent behaviour. After these sources were minimised, the cooling power constantly entering the chamber was of order a few nWs. This gives a scattering rate of around a single scattering event per atom every 20 ms. Considering this and the various sources of contaminant light identified, it seems likely that the system is currently limited by these effects.

Chapter 6

Summary

This thesis presents the advances in an atom interferometer at the University of Liverpool following a series of design enhancements and their implementation over several years, tailored towards observing interference in the chamber. The following is a summary of the improvements to the experiment that were undertaken as part of this work.

The rubidium-85 magneto-optical trap was redesigned to be both fibre coupled and have increased beam diameters, allowing for a two orders of magnitude increase in the amount of trapped atoms. This was a vast improvement over the previous, mirror-based method, allowing much more convenient beam alignment. With the implementation and optimisation of laser cooling techniques an optical molasses at around 10 μK was demonstrated. The state detection system was upgraded to improve both sensitivity and stability. This reduced unwanted light reaching the photodiode, allowing the MOT to be imaged with an enhanced signal-to-noise ratio, and resulted in a state detection system which needs minimal realignment and is flexible enough to be used for diagnostics, atom number measurements, temperature measurements and ultimately for the state ratio detection of the interferometer.

Various sources of contaminant light were found to be present during the state manipulation phase, leading to incomplete depopulation of the excited hyperfine state. These sources were identified and removed or minimised. These improvements allowed for the coherent

manipulation of an atomic system via the observation of Rabi oscillations. The Raman beams were further used to calibrate $\pi/2$ and π pulses, leading to a clock sequence being implemented, demonstrating Ramsey fringes. Observation of fringes was clear evidence of interference between the two hyperfine states.

The experiment is currently undergoing a series of upgrades, based on the outcomes of this work and the consequent understanding of the system's limitations. These upgrades consist of redesigning the vacuum chamber to allow more scope for optical improvements and increasing the measurement cycle rate. This will be achieved in part by a cold-atom source for the MOT (as opposed to loading the atom cloud from warm vapour) which is currently under construction and will reduce the $\sim$10 s loading time by an order of magnitude [100][101][102]. The new design will increase the interference times and will, combined with large momentum transfer techniques [103], vastly improve measurement sensitivity.

In summary, the coherent control of atomic states via Bloch oscillations, as well as the ability to demonstrate interference, both of which are necessary for an atom interferometry sequence, were established. The near-term future of the experiment consists of demonstrating velocity sensitive interference, with an upgraded experiment to be realised in the longer term.

Appendix A

Rubidium 85 D2 Transition Data [51]

Frequency	ω_0	$2\pi \cdot 384.230406373(14)$ THz
Transition energy	$\hbar\omega_0$	1.589 049 139(38) eV
Wavelength (vacuum)	λ	780.241 368 271(27) nm
Isotope shift	$\omega_0(^{87}\mathrm{Rb}) - \omega_0(^{85}\mathrm{Rb})$	$2\pi \cdot 78.095(12)$ MHz
Lifetime	τ	26.2348(77) ns
Natural Linewidth	Γ	$2\pi \cdot 6.0666(18)$ MHz
Recoil Velocity	v_r	6.0230 mm/s
Recoil Energy	ω_r	$2\pi \cdot 3.8597$ kHz
Recoil Temperature	T_r	370.47 nK
Doppler Temperature	T_D	145.57μK

References

[1] Alexander D. Cronin, Joerg Schmiedmayer, and David E. Pritchard. Atom interferometers. 2007.

[2] William D. Phillips. Nobel lecture: Laser cooling and trapping of neutral atoms. *Nobel Media*, 1997.

[3] Wolfgang Ketterle. When atoms behave as waves: Bose-einstein condensation and the atom laser. *Nobel Media*, 2001.

[4] Peter Asenbaum, Chris Overstreet, Tim Kovachy, Daniel D. Brown, Jason M. Hogan, and Mark A. Kasevich. Phase Shift in an Atom Interferometer due to Spacetime Curvature across its Wave Function. *Physical Review Letters*, 118(18):183602, May 2017.

[5] G. Rosi, G. DâAmico, L. Cacciapuoti, F. Sorrentino, M. Prevedelli, M. Zych, Ä Brukner, and G. M. Tino. Quantum test of the equivalence principle for atoms in coherent superposition of internal energy states. *Nature Communications*, 8:ncomms15529, June 2017.

[6] Savas Dimopoulos, Peter W. Graham, Jason M. Hogan, and Mark A. Kasevich. General Relativistic Effects in Atom Interferometry. *Physical Review D*, 78(4), August 2008. arXiv: 0802.4098.

[7] Malo Cadoret, Estefania de Mirandes, Pierre Cladé, Saïda Guellati-Khélifa, Catherine Schwob, Fran çois Nez, Lucile Julien, and Fran çois Biraben. Combination of bloch oscillations with a ramsey-bordé interferometer: New determination of the fine structure constant. *Phys. Rev. Lett.*, 101:230801, Dec 2008.

[8] Richard H. Parker, Chenghui Yu, Weicheng Zhong, Brian Estey, and Holger Müller. Measurement of the fine-structure constant as a test of the standard model. *Science*, 360(6385):191–195, 2018.

[9] T. Kovachy, P. Asenbaum, C. Overstreet, C. A. Donnelly, S. M. Dickerson, A. Sugarbaker, J. M. Hogan, and M. A. Kasevich. Quantum superposition at the half-metre scale. *Nature*, 528(7583):530–533, December 2015.

[10] A. Arvanitaki, P. Graham, J. Hogan, S. Rajendran, and K. Van Tilburg. Phys. Rev. D **97**, 075020 (2018).

[11] P. Graham, D. Kaplan, J. Mardon, S. Rajendran, and W. A. Terrano. Phys. Rev. D **93**, 075029 (2016).

[12] P. Graham, D. Kaplan, J. Mardon, S. Rajendran, W. A. Terrano, L. Trahms, and T. Wilkason. Phys. Rev. D **97**, 055006 (2018).

[13] Benjamin M Roberts, Geoffrey Blewitt, Conner Dailey, Mac Murphy, Maxim Pospelov, Alex Rollings, Jeff Sherman, Wyatt Williams, and Andrei Derevianko. Search for domain wall dark matter with atomic clocks on board global positioning system satellites. *Nature Communications*, 8(1):1195, 2017.

[14] Tigran Kalaydzhyan and Nan Yu. Extracting dark matter signatures from atomic clock stability measurements. *Phys. Rev. D*, 96:075007, Oct 2017.

[15] Mark Kasevich and Steven Chu. Atomic interferometry using stimulated raman transitions. *Phys. Rev. Lett.*, 67:181–184, Jul 1991.

[16] Achim Peters, Keng Yeow Chung, and Steven Chu. Measurement of gravitational acceleration by dropping atoms. *Nature*, 400:849–852, Aug 1999.

[17] Susannah M. Dickerson, Jason M. Hogan, Alex Sugarbaker, David M. S. Johnson, and Mark A. Kasevich. Multiaxis inertial sensing with long-time point source atom interferometry. *Phys. Rev. Lett.*, 111:083001, Aug 2013.

[18] G. Rosi, L. Sorrentino, F. Cacciapuoti, M. Prevedelli, and G. M. Tino. Precision measurement of the newtonian gravitational constant using cold atoms. *Nature*, 510(7506), 2014.

[19] TL Gustavson, A Landragin, and MA Kasevich. Rotation sensing with a dual atom-interferometer sagnac gyroscope. *Classical and Quantum Gravity*, 17(12):2385, 2000.

[20] Savas Dimopoulos, Peter W. Graham, Jason M. Hogan, Mark A. Kasevich, and Surjeet Rajendran. An Atomic Gravitational Wave Interferometric Sensor (AGIS). *Physical Review D*, 78(12), December 2008. arXiv: 0806.2125.

[21] Remi Geiger. Future gravitational wave detectors based on atom interferometry. 2016.

[22] Norman F. Ramsey. A molecular beam resonance method with separated oscillating fields. *Phys. Rev.*, 78:695–699, Jun 1950.

[23] T. L. Nicholson, S. L. Campbell, R. B. Hutson, G. E. Marti, B. J. Bloom, R. L. McNally, W. Zhang, M. D. Barrett, M. S. Safronova, G. F. Strouse, W. L. Tew, and J. Ye. Systematic evaluation of an atomic clock at 2×10^{18} total uncertainty. *Nature Communications*, 6:6896 EP –, 04 2015.

[24] M. Inguscio and M. Fallani. *Atomic physics: Precise Measurements and Ultracold Matter*. OUP Oxford, 2015.

[25] F.G. Mayor. *The Quantum Beat: Principles and Applications of Atomic Clocks*. Springer, 2007.

[26] C. Audoin and B. Guinot. *The Measurement of Time: Time, Frequency and Atomic Clocks*. Cambridge University Press, 2001.

[27] Mark Kasevich and Steven Chu. Atomic interferometry using stimulated raman transitions. *Phys. Rev. Lett.*, 67:181–184, Jul 1991.

[28] R. Colella, A. W. Overhauser, and S. A. Werner. Observation of gravitationally induced quantum interference. *Phys. Rev. Lett.*, 34:1472–1474, Jun 1975.

[29] M. Kasevich and S. Chu. Measurement of the gravitational acceleration of an atom with a light-pulse atom interferometer. *Applied Physics B*, 54(5):321–332, May 1992.

[30] Pippa Storey and Claude Cohen-Tannoudji. The feynman path integral approach to atomic interferometry. a tutorial. *Journal de Physique II*, 4(11):1999–2027, 1994.

[31] Susannah M. Dickerson, Jason M. Hogan, Alex Sugarbaker, David M. S. Johnson, and Mark A. Kasevich. Multiaxis inertial sensing with long-time point source atom interferometry. *Phys. Rev. Lett.*, 111:083001, Aug 2013.

[32] Achim Peters, Keng Yeow Chung, and Steven Chu. High-precision gravity measurements using atom interferometry. *Metrologia*, 38(1):25, 2001.

[33] Torsten Gerrit Petelski. *Atom interferometers for precision gravity measurements*. PhD thesis, Paris 6, 2005.

[34] Daniel A. Steck. *Quantum and Atom Optics*. http://steck.us/teaching, 2017.

[35] Malte Schmidt. *A mobile high-precision gravimeter based on atom interferometry*. PhD thesis, Humboldt-Universität zu Berlin, Mathematisch-Naturwissenschaftliche Fakultät I, 2011.

[36] S. Perlmutter, G. Aldering, G. Goldhaber, R. A. Knop, P. Nugent, P. G. Castro, S. Deustua, S. Fabbro, A. Goobar, D. E. Groom, I. M. Hook, A. G. Kim, M. Y. Kim, J. C. Lee, N. J. Nunes, R. Pain, C. R. Pennypacker, R. Quimby, C. Lidman, R. S. Ellis, M. Irwin, R. G. McMahon, P. Ruiz-Lapuente, N. Walton, B. Schaefer, B. J. Boyle, A. V. Filippenko, T. Matheson, A. S. Fruchter, N. Panagia, H. J. M. Newberg, and W. J. Couch. Measurements of Omega and Lambda from 42 High-Redshift Supernovae. *The Astrophysical Journal*, 517(2):565–586, June 1999. arXiv: astro-ph/9812133.

[37] Planck Collaboration. Planck 2015 results - xiii. cosmological parameters. *AA*, 594:A13, 2016.

[38] Will J. Percival, Beth A. Reid, Daniel J. Eisenstein, Neta A. Bahcall, Tamas Budavari, Joshua A. Frieman, Masataka Fukugita, James E. Gunn, Željko Ivezić, Gillian R. Knapp, Richard G. Kron, Jon Loveday, Robert H. Lupton, Timothy A. McKay, Avery Meiksin, Robert C. Nichol, Adrian C. Pope, David J. Schlegel, Donald P. Schneider, David N. Spergel, Chris Stoughton, Michael A. Strauss, Alexander S. Szalay, Max Tegmark, Michael S. Vogeley, David H. Weinberg, Donald G. York, and Idit Zehavi. Baryon acoustic oscillations in the sloan digital sky survey data release 7 galaxy sample. *Monthly Notices of the Royal Astronomical Society*, 401(4):2148–2168, 2010.

[39] Saul Perlmutter. Nobel lecture: Measuring the acceleration of the cosmic expansion using supernovae. *Rev. Mod. Phys.*, 84:1127–1149, Aug 2012.

[40] Paul Hamilton, Matt Jaffe, Philipp Haslinger, Quinn Simmons, Holger Müller, and Justin Khoury. Atom-interferometry constraints on dark energy. *Science*, 349(6250):849–851, 2015.

[41] Clare Burrage, Edmund J. Copeland, and E.A. Hinds. Probing dark energy with atom interferometry. *Journal of Cosmology and Astroparticle Physics*, 2015(03):042, 2015.

[42] R. R. Caldwell, Rahul Dave, and Paul J. Steinhardt. Cosmological imprint of an energy component with general equation of state. *Phys. Rev. Lett.*, 80:1582–1585, Feb 1998.

[43] R. J. Adler, H. Mueller, and M. L. Perl. A Terrestrial Search for Dark Contents of the Vacuum, such as Dark Energy, Using Atom Interferometry. *International Journal of Modern Physics A*, 26:4959–4979, 2011.

[44] Ronald J. Adler, Brendan Casey, and Ovid C. Jacob. Vacuum catastrophe: An elementary exposition of the cosmological constant problem. *American Journal of Physics*, 63(7):620–626, 1995.

[45] Sean M. Carroll. *Spacetime and Geometry*. Addison Wesley, 2004.

[46] Matthew Himsworth. *Coherent manipulation of ultracold rubidium*. PhD thesis, University of Southmpton, 2009.

[47] Christopher J Foot. *Atomic physics*. OUP Oxford, 2004.

[48] Carl Wieman, Gwenn Flowers, and Sarah Gilbert. Inexpensive laser cooling and trapping experiment for undergraduate laboratories. *American Journal of Physics*, 63(4):317–329, 1995.

[49] Jérôme Estève. Trapped by nanostructures. *Nature Nanotechnology*, 8:317 EP –, 05 2013.

[50] David Morris. *Development Of A Prototype Atomic Interferometer For Fundamental Physics Searches*. PhD thesis, University of Liverpool, 2018.

[51] Daniel Adam Steck. Rubidium-85 d line data, 2008.

[52] Jean Dalibard and Claude Cohen-Tannoudji. Laser cooling below the doppler limit by polarization gradients: simple theoretical models. *JOSA B*, 6(11):2023–2045, 1989.

[53] A M Steane, G Hillenbrand, and C J Foot. Polarization gradient cooling in a one-dimensional sigma + - sigma - configuration for any atomic transition. *Journal of Physics B: Atomic, Molecular and Optical Physics*, 25(22):4721, 1992.

[54] Chang Huang, Pei-Chen Kuan, and Shau-Yu Lan. Laser cooling of ^{85}Rb atoms to the recoil-temperature limit. *Phys. Rev. A*, 97:023403, Feb 2018.

[55] Malte Schmidt, Alexander Senger, M Hauth, C Freier, V Schkolnik, and Achim Peters. A mobile high-precision absolute gravimeter based on atom interferometry. *Gyroscopy and Navigation*, 2(3):170–177, 2011.

[56] Yukun Luo, Shuhua Yan, Qingqing Hu, Aiai Jia, Chunhua Wei, and Jun Yang. Contrast enhancement via shaped raman pulses for thermal coldatom cloud interferometry. *The European Physical Journal D*, 70(12):262, Dec 2016.

[57] Alexander Dunning, Rachel Gregory, James Bateman, Nathan Cooper, Matthew Himsworth, Jonathan A. Jones, and Tim Freegarde. Composite pulses for interferometry in a thermal cold atom cloud. *Phys. Rev. A*, 90:033608, Sep 2014.

[58] Boyan T. Torosov and Nikolay V. Vitanov. Smooth composite pulses for high-fidelity quantum information processing. *Phys. Rev. A*, 83:053420, May 2011.

[59] Kazuyuki Fujii. Introduction to the rotating wave approximation (rwa): Two coherent oscillations. *arXiv preprint arXiv:1301.3585*, 2013.

[60] Richard P. Feyman. *The Feynman Lectures on Physics Volume III*, volume 3. Pearson Addison Wesley, 2006.

[61] Rui Han, Hui Khoon Ng, and Berthold-Georg Englert. Raman transitions without adiabatic elimination: A simple and accurate treatment. *Journal of Modern Optics*, 60(4):255–265, 2013.

[62] Etienne Brion, Line Hjortshøj Pedersen, and Klaus Mølmer. Adiabatic elimination in a lambda system. *Journal of Physics A: Mathematical and Theoretical*, 40(5):1033, 2007.

[63] Harold J. Metcalf and Peter van der Straten. *Laser Cooling and Trapping*. Springer-Verlag, New York, 1999.

[64] Paul R Berman. *Atom interferometry*. Academic press, 1997.

[65] Alexander Dunning. *Coherent atomic manipulation and cooling using composite optical pulse sequences*. PhD thesis, University of Southampton, 2014.

[66] Jason Hogan. *Towards Precision Tests of General Relativity using an Atom Interferometer*. PhD thesis, Stanford University, 2010.

[67] *Laser Cooling and Trapping*. McLeod Research Group, University of Colorado Boulder.

[68] *4.5" Spherical Octagon (tapped holes)- Vacuum Chamber*. Kimball Physics.

[69] *SAES alkali metal dispensing data sheets*. Saes, Jul 2014.

[70] Alexander Franzen. Component library. http://www.gwoptics.org/ComponentLibrary/.

[71] Robert Scholten and Alex Slavec. Moglabs external cavity diode laser model ecd004, revision 4.20.

[72] Sebastian Saliba and Robert E Scholten. Linewidths below 100 khz with external cavity diode lasers. 48:6961, 12 2009.

[73] W Hong. Design and characterization of a littrow configuration external cavity diode laser.

[74] Robert Scholten and Alex Slavec. Moglabs external cavity diode laser controller, models dlc-202, dlc-252, dlc-502, revision 7.01.

[75] Oliver S. Burrow. *The Development of a Light Pulse Atom Interferometer Towards a Parameter Search of the Dark Contents of the Vacuum*. PhD thesis, University of Liverpool, 2015.

[76] Joe S.T. Heffer. *Towards precision gravimetry using light-pulse atom interferometry*. PhD thesis, University of Liverpool, 2017.

[77] *3080-122 AOM specifications sheet*. Crystal Technology Inc.

[78] *Maximizing AO Diffraction Efficiency*. Isomet Corp.

[79] Zedboard product briefs. http://www.zedboard.org/sites/default/files/product_briefs/5066-PB-AES-Z7EV-7Z020-G-V3c%20%281%29_0.pdf.

[80] Novatech 409b. http://www.novatechsales.com/PDF_files/409b_ds.pdf.

[81] *WR-284 Waveguide Standard Gain Horn Antenna Operating From 2.6 GHz to 3.95 GHz With a Nominal 10 dB Gain SMA Female Input*. Pasternack.

[82] *Signal Generator SMA100A Operating Manual*. Rohde and Schwarz.

[83] *ZX90-2-19-S+ x2 Frequency Multiplier*. Mini-Circuits.

[84] *ZVE-3W-83+ high power amplifier datasheet*. Mini-Circuits.

[85] *HX2400 Ultra-low phase noise RF amplifier datasheet*. Holzworth Instrumentation.

[86] P. Bouyer, T. L. Gustavson, K. G. Haritos, and M. A. Kasevich. Microwave signal generation with optical injection locking. *Opt. Lett.*, 21(18):1502–1504, Sep 1996.

[87] Kai Wang, Zhanwei Yao, Runbing Li, Sibin Lu, Xi Chen, Jin Wang, and Mingsheng Zhan. Hybrid wide-band, low-phase-noise scheme for raman lasers in atom interferometry by integrating an acousto-optic modulator and a feedback loop. *Appl. Opt.*, 55(5):989–992, Feb 2016.

[88] *AO Frequency Shifter PF-1500-200-780*. Brimrose Corporation of America.

[89] *ZHL-5W-2G+ Coaxial High Power Amplifier datasheet*. Mini-Circuits.

[90] *Fibre Collimators 60FC*. Schafter and Kirchhoff.

[91] *BP209-VIS/M - Dual Scanning Slit Beam Profiler, 200 - 1100 nm, Ø2.5 µm - Ø9 mm, Metric*. Thorlabs.

[92] *818-BB-45 Fast Biased Silicon Photodetector*. Newport.

[93] *Pico Technology. Picoscope 9201 data sheet*. Pico Technology.

[94] Filip Dvorak, Jan Maschke, and Cestmir Vlcek. The response of polarization maintaining fibers upon temperature field disturbance. *Advances in Electrical and Electronic Engineering*, 12(2), 2014.

[95] Zhihong Li, X. Steve Yao, Xiaojun Chen, Hongxin Chen, Zhuo Meng, and Tiegen Liu. Complete characterization of polarization-maintaining fibers using distributed polarization analysis. *Journal of Lightwave Technology*, 33(2), 2015.

[96] *Left-Handed Polymer Circular Polarizers*. Thorlabs, Inc.

[97] O. Burrow, A. Carroll, S. Chattopadhyay, J. Coleman, G. Elertas, J. Heffer, C. Metelko, R. Moore, D. Morris, M. Perl, J. Ralph, and J. Tinsley. Atom Interferometry for Dark Contents of the Vacuum Searches. *arXiv:1705.09376 [physics]*, May 2017. arXiv: 1705.09376.

[98] Yuri Ovchinnikov and Giuseppe Marra. Accurate rubidium atomic fountain frequency standard. *Metrologia*, 48(3):87, 2011.

[99] S. Kuhr, W. Alt, D. Schrader, I. Dotsenko, Y. Miroshnychenko, A. Rauschenbeutel, and D. Meschede. Analysis of dephasing mechanisms in a standing wave dipole trap. 2004.

[100] Yuri B. Ovchinnikov. Compact magneto-optical sources of slow atoms. *Optics Communications*, 249(4–6):473 – 481, 2005.

[101] K. Dieckmann, R. J. C. Spreeuw, M. Weidemüller, and J. T. M. Walraven. Two-dimensional magneto-optical trap as a source of slow atoms. *Phys. Rev. A*, 58:3891–3895, Nov 1998.

[102] K. H. Kim, K. I. Lee, H. R. Noh, W. Jhe, N. Kwon, and M. Ohtsu. Cold atomic beam produced by a conical mirror funnel. *Phys. Rev. A*, 64:013402, May 2001.

[103] Holger Müller, Sheng-wey Chiow, Quan Long, Sven Herrmann, and Steven Chu. Atom interferometry with up to 24-photon-momentum-transfer beam splitters. *Phys. Rev. Lett.*, 100:180405, May 2008.